Fakultät für Elektrotechnik und Informationstechnik
der Technischen Universität München
Lehrstuhl für Technische Elektrophysik

Real-Time Magnetic Field Monitoring in Magnetic Resonance Imaging

Pekka Tapani Sipilä

Vollständiger Abdruck der von der Fakultät für Elektrotechnik und Informationstechnik der Technischen Universität München zur Erlangung des akademischen Grades eines

Doktors-Ingenieur (Dr.-Ing.)

genehmigten Dissertation.

Vorsitzender:	Univ.-Prof. Dr.-Ing. T. Eibert
Prüfer der Dissertation:	1. Univ.-Prof. Dr. rer. nat. G. Wachutka
	2. Univ.-Prof. Dr.-Ing. habil. Dr. h.c. A. Koch

Die Dissertation wurde am 19.11.2010 bei der Technischen Universität München eingereicht und durch die Fakultät für Elektrotechnik und Informationstechnik am 08.08.2011 angenommen.

Tekikö tämä minusta viisamman?
Siunasiko se järjellä?

Omistettu Dorothealle, ja kaikille teille,
jotka olette minulle tärkeitä ja rakkaita

Summary

Imperfections in the magnetic gradient fields for image encoding can severely deteriorate the quality of magnetic resonance imaging (MRI), especially in the case of advanced imaging applications such as fast-acquisition, phase-contrast-based flow quantification, and diffusion-tensor imaging. Gradient field imperfections are caused by eddy currents induced in the conductive structures of the MRI scanner, gradient amplifier nonlinearities, and anisotropic gradient delays, as well as system instabilities and parameter drifts caused by heating. It is expected that by addressing these gradient-encoding disturbances, the diagnostic capabilities of MRI could be significantly improved for both research and routine clinical applications. In this thesis, different approaches to improving the quality of MRI are investigated using a dedicated magnetic field monitoring system, especially in the context of the advanced imaging applications mentioned above

The performance requirements of dedicated magnetic field monitoring systems are derived from general MRI encoding considerations, and the respective capabilities of existing magnetometer techniques are explored. Implementations of the most promising techniques, such as pick-up coils and nuclear magnetic resonance (NMR) probes, are further studied in both theory and practice. The analysis shows that, of these two approaches, only the nuclear magnetic resonance probes provide a basis for delivering the desired performance necessary for improving image quality.

Various NMR probe designs are further developed for magnetic field monitoring assisted MRI experiments. For operating the NMR probes, a dedicated multinuclear transmit-receiver for NMR applications is developed including an advanced excitation scheme for maintaining phase coherency between the NMR-probe spin ensembles and the radio frequency pulses. Such an independent add-on monitoring system is found to be particularly attractive as it is easily interfaced with existing MRI scanners, it does not require MRI pulse sequence

modifications, and it does not introduce undesired image artifacts or lead to a reduction of the signal-to-noise ratio.

The developed phase-coherent transmission technique establishes a basis for a generalized NMR-based field monitoring system for clinical applications. In comparison to the standard operation scheme, which is based on noncoherent, long-interval excitations, the novel technique provides a robust performance that is insensitive to applied imaging parameters, such as resolution and repetition rate. Furthermore, the complexity of probe manufacturing is largely reduced with this scheme, enabling a more cost-effective system integration into radio frequency coils, patient tables, and magnet bores.

The developed prototypes of ^{1}H and ^{2}H NMR probes, as well as the dedicated multinuclear transmit-receiver system, are characterized in a 3-T magnetic field MRI system. The performance of the developed NMR probes is proven to meet the requirements that are needed for magnetic field monitoring assisted MRI. ^{2}H NMR probes are found to be superior with respect to more traditional ^{1}H NMR probes since ^{2}H NMR probes are frequency decoupled from standard ^{1}H-based MRI. Because of this, imaging experiments accompanied by ^{2}H magnetic field monitoring hardware are clean of interference artifacts.

It is shown that the image quality of advanced MRI methods, such as single-shot imaging and phase-contrast-based flow quantification, is significantly improved by using magnetic field monitoring. The novel phase-coherent, short-interval excitation scheme, which ensures a robust and continuous operation of NMR probes regardless of applied imaging parameters, is also verified in practice. In summary, it can be concluded that the presented developments, i.e., the phase-coherent, short-interval excitation scheme and the ^{2}H NMR probes, provide significant progress toward the clinical implementation of magnetic field monitoring in MRI.

Zusammenfassung

In der Kernspintomografie können Imperfektionen der Gradientenkodierung zu einer signifikanten Beeinträchtigung der Bildqualität führen. Dies trifft besonders auf neuere Anwendungen zu, wie die der Schnellakquisition, die der phasenkontrast-basierten Flussquantifizierung und Diffusionstensorbildgebung. Physikalisch erklären sich Gradientenimperfektionen durch Wirbelströme in leitende Strukturen des Scanners, weiterhin durch nichtlineare Gradientenverstärker und anisotrope Zeitverzögerungen sowie durch Instabilitäten und Parameterdrift, verursacht von Erwärmungseffekten. Entsprechend wird angenommen, dass eine Beseitigung dieser Ungenauigkeiten der Gradientenkodierung die Bildgebungsperformance sowohl für klinische als auch für Forschungszwecke wesentlich erweitern und verbessern kann. Im Rahmen dieser Dissertation werden zugunsten der Verbesserung der kernspintomografischen Bildqualität verschiedene Ansätze von Magnetfeld-Monitoring untersucht, insbesondere für die oben aufgeführten Anwendungen.

Basierend auf der grundlegenden Physik der kernspintomografischen Bildkodierung werden die Spezifikationen für dezidierte Magnetfeld-Monitoring-Systeme hergeleitet. Auf diesen fußt die Bewertung der bekannten Magnetometer-Technologien. Die vielversprechendsten Ansätze in Form von Faradayspulen und Kernmagnetresonanzsonden werden praktisch implementiert und im Detail untersucht. Dabei zeigt sich, dass von den beiden verfolgten Ansätzen nur die Kernmagnetresonanzsonden auch tatsächlich die notwendigen Spezifikationen erfüllen.

Verschiedene auf Kernmagnetresonanzsonden basierte Magnetfeld-Monitoring-Architekturen werden daraufhin weiterentwickelt. Ein unabhängiges Add-on-Messsystem erweist sich jedoch als besonders geeignet, da es leicht an herkömmliche Kernspintomografen angeschlossen werden kann, keine besonderen Modifizierungen der Pulssequenzen erfordert und auch keine unerwünschten Artefakte oder Signal-zu-Rausch-Störungen bewirkt.

Das dezidiert entwickelte System beinhaltet ein fortgeschrittenes Anregungsschema zur Aufrechterhaltung der Phasenkohärenz zwischen dem präzisierenden Spinensamble und der Radiofrequenz-Anregungsspule. Diese Technik wird vorgestellt, welche eine attraktive Lösung darstellt auf dem Weg zu einem kontinuierlichen Magnetfeld-Monitoring. Im Gegensatz zu dem herkömmlichen Anregungsschema bietet das neue Verfahren robuste Performance, unabhängig von den Bildgebungsparametern wie Auflösung und Repetitionszeit. Weiters reduziert sich durch dieses Design auch die Herstellungskomplexität mit dem Ausblick auf eine einfachere und kosteneffektivere Systemintegration in Radiofrequenzspulen, Patiententisch und Magnetbohrung.

Die eigens hergestellten ^{1}H- und ^{2}H-Kernmagnetresonanzsonden sowie das für deren Betrieb entwickelte unabhängige Messsystem wird auf einem 3-Tesla-Hochfeld-Kernspintomografen charakterisiert. Es wird verifiziert, dass die Performance dieser Kernmagnetresonanzsonden den spezifischen Anforderungen für das Magnetfeld-Monitoring genügen. Aufgrund der Frequenzentkopplung zwischen ^{2}H-Kernmagnetresonanzsonden und standard ^{1}H-basierter Bildgebung sowie dem damit verbundenen Fehlen von Interferenzartefakten werden diese Proben im Vergleich zu standard ^{1}H-Kernmagnetresonanzsonden als klar überlegen bewertet.

Durch die Verwendung von ^{2}H-basiertem Magnetfeld- Monitoring verbessert sich ebenso die Bildgebungsqualität für fortgeschrittene Schnellakquisition und phasenkontrast-basierter Flussquantifizierung. Die Funktionalität des neu entwickelten, schnellen und phasenkohärenten Anregungsschemas für ein robustes und kontinuierliches Betreiben der Kernmagnetresonanzsonden wird ebenfalls aufgezeigt. Zusammenfassend bedeuten die im Rahmen dieser Dissertation präsentierten Entwicklungen, i.e., der raschen und phasenkohärenten Anregung sowie ^{2}H-Kernmagnetresonanzsonden, einen wesentlichen Fortschritt in Richtung einer klinischen Implementierung von Magnetfeld-Monitoring.

Contents

List of Figures

List of Tables

1

Introduction

Since the first nuclear magnetic resonance (NMR) signal was observed by Isidor Rabi in 1938 [1], the technique of utilizing NMR phenomenon has been evolving to its present form of a highly accurate diagnostic and research tool. The fields of application of NMR range from material sciences and biology to high-resolution clinical imaging, also known as the magnetic resonance imaging (MRI).

One challenge facing present-day MRI scanners is insufficient magnetic field fidelity for novel image-acquisition applications that offer faster imaging and improved functionality. With such novel techniques, the nonideal field characteristics induced by eddy currents and imperfect gradient-field hardware often result in image artifacts at unacceptable levels.

This thesis explores the possibilities of improving the functionality and quality of MRI by utilizing a magnetic field monitoring system to address these nonideal magnetic fields. The problem is further detailed in this chapter and an overview of existing methods to counter the shortcomings is given. Outlining the structure of the thesis concludes this chapter. For the reader not familiar with the physics of MRI, Chapter 2 is recommended as a prerequisite. For a more retrospective introduction to magnetic resonance (MR), the article by Hahn is recommended [2].

1.1 Magnetic field imperfections in MRI

The quality of MR images can be degraded by various imperfections in the magnetic fields applied for image acquisition. The main magnetic field of an MRI scanner is produced with only a certain level of homogeneity. These field imperfections in the parts-per-million (ppm) range can generate noticeable artifacts

in MR images [3, 4]. Further background field inhomogeneities arise from the magnetic moments of the patients themselves. Challenging for imaging are not only paramagnetic implants but also air-tissue interfaces, especially those around lungs, ear tunnels, and nasal cavities. In addition to static perturbations, the susceptibility differences can also lead to dynamic field disturbances when a patient is moving during imaging (e.g., breathing).

Imperfect gradient fields are typically caused by errors related to gradient drivers, gradient coils, or eddy currents [5, 6]. Gradient drivers may not fully reproduce the desired waveforms owing to imperfect timing or to device nonlinearities. As indicated by Maxwell's equations, the magnetic fields in free space are divergence and curl free. Hence, having perfectly linear x-, y-, or z-gradient fields for spatial encoding is fundamentally impossible and concomitant fields always exist to some extent.

Temporally changing magnetic fields introduce eddy currents in any conductive structures inside MRI scanners. Subsequently, the eddy currents generate secondary magnetic fields, which decay with time constants ranging from microseconds up to several seconds. In addition to the mentioned imperfections, environmental changes (e.g., air pressure and temperature drift) can deviate the background field and the gradient hardware performance.

Magnetic field imperfections in MRI can be divided into two categories depending upon the magnitude of errors and on the imaging functionality. Field perturbations of the first kind affect the imaging to an extent such that real-time compensation of these is needed to preserve the functionality of the imaging sequence. An exemplary magnetic field imperfection of the first kind is a severe background field inhomogeneity inside an imaging slice. Dark regions result in an image that corresponds to regions where spins are left partly or completely unexcited.

Magnetic field errors of the second kind are less severe in nature. They relate to acquisitions that provide all the necessary data for image reconstruction. However, because of distorted field profiles, the resulting images are degraded. The severity and the nature of image artifacts are related to the chosen acquisition schemes and reconstruction strategies. Field imperfections of the second kind can be in principle compensated in postprocessing by using knowledge of the actual field behavior. For example, small local background field offsets during spiral imaging are known to lead to blurring and ghosting artifacts in the acquired images [7].

In addition to the static magnetic and slowly varying gradient field imperfections, MRI is susceptible to imperfection in the magnetic fields for spin excitation, which are at radio frequencies. These imperfections influence especially imaging at higher background field strengths as the wavelengths of the radio fre-

quency (RF) fields become comparable to the dimensions of a human body and the effects of field propagation and attenuation become more observable. The topic of RF domain magnetic field inhomogeneity is not further discussed here as it is considered to be beyond of the scope of this thesis.

1.2 Strategies to address nonideal magnetic fields in MRI

A large variety of methods have been introduced to improve the image quality in MRI despite the existing imperfections in applied magnetic fields. A variety of pulse sequences exist that are inherently less sensitive to background magnetic field inhomogeneities, gradient imperfections, and eddy currents, [6, 8, 9, 10, 11, 12]. Standard Cartesian gradient and spin echo sequences are well-known examples.

For more advanced imaging sequences, the insensitivity to magnetic field imperfections is not the case however. For example, diffusion-weighted and phase-contrast imaging are strongly influenced by eddy-current-related errors because both of these sequences are based on strong motion sensitizing gradients prior to image data acquisition. [6, 13, 14]. In addition, fast imaging acquisitions, e.g., echo planar imaging (EPI), as well as spiral imaging are known to be notorious for distorting static and gradient fields [7, 15]. Of the mentioned examples, fast imaging schemes are found to be especially attractive despite their sensitivity to magnetic field imperfections. This is because the total imaging time of a patient can be reduced by roughly an order of magnitude with these acquisition schemes. In other words, utilizing these fast imaging sequences for everyday clinical use can lead to significant increase in patient throughputs.

A variety of software and hardware improvements have been pursued to increase the fidelity of MRI. With passive and dynamic shimming of the background field, field homogeneity on the order of 1 ppm over the scanner's imaging field of view is achieved in present-day clinical scanners [16]. This statement holds valid only in the absence of a patient. Higher order inhomogeneities that are experienced in air-tissue interfaces in nasal and oral cavities as well as in ear tunnel can be further tackled with diamagnetic patches acting as local passive shims [17]. The level of eddy-current-related imperfections has been significantly reduced by hardware innovations such as shielded gradients [18] and gradient preemphasis [19].

Calibration scans can be performed to map the background field and gradient characteristics [20, 21, 22, 23, 24, 25, 26, 27]. In the reconstruction phase, the information on field characteristics is merged into acquired raw data for improved image quality. Although calibration scans can be applied to accurately

correct field perturbations of the second kind, these scans can take longer than the actual imaging scan [28]. In addition, calibration scans fail to correct for any parameter drifts or nonreproducible effects during imaging, such as heating of the (gradient) hardware during gradient-intensive functional MRI studies or patient motion.

Methods have been introduced to measure the magnetic field behavior with dedicated magnetometer systems [24, 29, 30, 31]. To overcome the drawbacks experienced with calibration-type measurements, sensor systems for real-time magnetic field monitoring during MRI acquisitions have been developed [32, 33, 34, 35]. An illustration of such a real-time magnetic field monitoring setup consisting of four field sensors is shown in Fig. 1.1. Real-time magnetic field monitoring in clinical applications is expected to concentrate on correcting gradient-related errors only. Measuring static field errors is considered to be too inaccurate already owing to the local background field perturbations that are caused by a patient.

Of time-varying fields, gradient field monitoring in clinical applications is best suited for correcting spatially constant and linear field error terms. This is because the presence of a patient prevents measurement points close to the isocenter, which are ideally required for accurate monitoring of higher order field terms. Alternatively, some prior knowledge, which is based on gradient field models, can be fused to higher order monitoring data. With this approach, an acceptable level of accuracy for higher order field monitoring might still be achieved despite the absence of measurement points in the vicinity of the isocenter. If no real-time monitoring is required but the monitoring hardware is applied only for calibration purposes in the absence of a patient, higher order field cameras with isocenter measurement points can be utilized of course [36].

If one part of the field monitoring probes is attached to a patient, the possibility to track patient movement becomes available. In reconstruction, this information can be utilized for damping motion-related image artifacts [37].

Magnetic field monitoring hardware can be utilized for correcting field imperfections of the first kind with a dedicated feedback loop to the gradient hardware. A similar technique already exists in present-day clinical MRI scanners and the system is based on monitoring currents fed to the gradient coils. However, it is expected that a direct measurement of the four-dimensional field patterns can offer potentially higher precision for such a correction scheme.

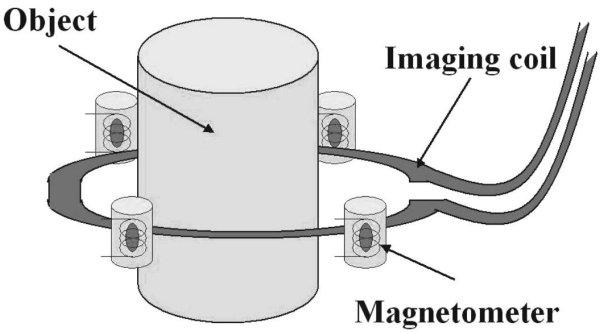

Fig. 1.1. *An MRI acquisition can be accompanied with a dedicated magnetometer array to map magnetic field profiles for improved MR image quality. In this example, the magnetic field sensors are placed around the object of interest for two-dimensional field monitoring.*

1.3 Magnetic field monitoring assisted image reconstruction

The gridding reconstruction algorithm is utilized to use field monitoring data for restoring image quality in magnetic field monitoring assisted MRI [38]. This algorithm is more typically utilized for non-Cartesian imaging (e.g., spiral or rosette) and the governing idea is to interpolate data values that are obtained from such imaging acquisition to corresponding Cartesian encoding values (cf. Fig. 1.2).

The fundamental difference between non-Cartesian imaging and magnetic field monitoring assisted MRI is that the utilized field monitoring system provides the actual k-space values that correspond to each acquired imaging sample point. The interpolation of the sample values to the corresponding Cartesian grid restores the applicability of fast-Fourier-transform-based image reconstruction. A drawback of the algorithm in its original form is that it is time consuming. For speeding up the reconstruction process, for example, techniques proposed by Beatty et al. [39] are recommended.

1.4 Outline of the thesis

Of the techniques to correct imperfect gradient-field-related image artifacts, real-time magnetic field monitoring is considered to be the most complete solution. With a proper magnetometer technique, the concept is precise. It does not

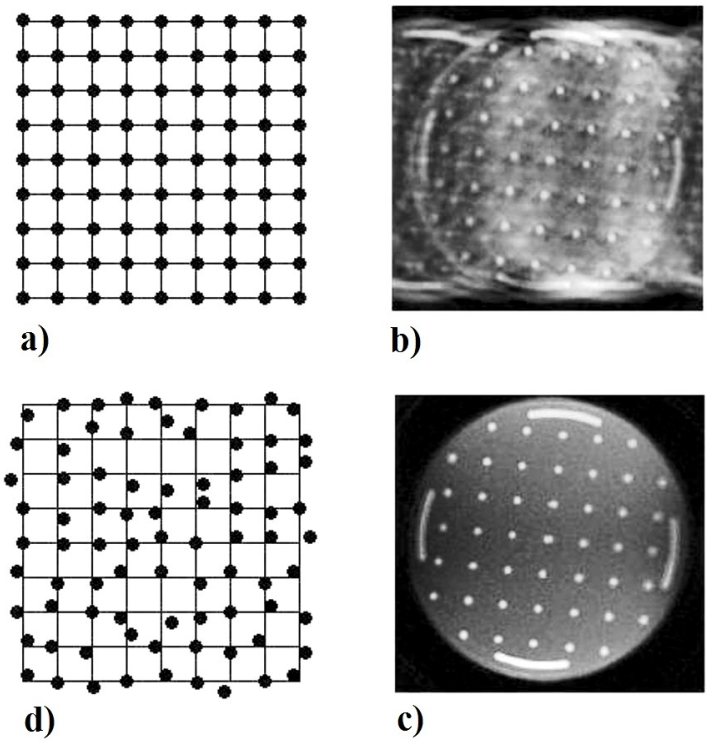

Fig. 1.2. *Simplistic illustration of gridding-based image reconstruction. Normal MRI acquisitions are based on a Cartesian gradient encoding of the object, as is shown in (a). If gradient fields are incapable of matching the required waveforms, the assumption of ideal gradients can lead to image artifacts, as is seen in (b). If the actual gradient values are known, as is the case in (c), the sample points can be interpolated to match the Cartesian values and the outcome is ideally an undistorted image, as is shown in (d).*

lengthen imaging sequences, and it is not vulnerable to drifts in different system parameters. The field monitoring system can also be utilized for corrections of field errors of the first kind as well as distortions from patient motion. This thesis aims to study the requirements for such a field monitoring system (cf. Chapter 3). It studies different magnetic field sensor technologies, and it seeks the most potentially useful technologies for practical implementations (cf. Chapter 4).

In this thesis, it will be shown that the most feasible magnetometer technologies for real-time magnetic field monitoring are pick-up coils (cf. Chapter 5) and NMR probes (cf. Chapter 6). Of these technologies, theoretical considerations, which are backed up with practical experiments, show that only NMR probes can fulfill the demanding performance requirements for magnetic field monitoring assisted MRI (cf. Chapters 5 and 9).

Various NMR probe designs and implementations for magnetic field monitoring exist with corresponding advantages and drawbacks. Different design considerations and the required electronics for operation are studied and discussed in Chapters 6, 7, and 8. The focus of the work is to develop an independent magnetic field monitoring system that is easily integrated into clinical MRI scanners. Such monitoring systems have performance characteristics fulfilling the derived requirements, do not introduce any unwanted image artifacts in standard MRI, and are applicable for any existing MRI acquisition scheme.

In Chapter 9, NMR probes based on different designs are characterized and their application to magnetic field monitoring assisted MRI is verified. Improved image quality with magnetic field monitoring is demonstrated for fast imaging acquisitions as well as with phase-contrast imaging experiments. A discussion and conclusions about the work done around the framework conclude this thesis (cf. Chapter 10).

2

Principles of MRI

In this chapter, the principles of MRI are introduced. The treatment of the topic leans on the references [6, 40, 41, 42, 43] if not otherwise mentioned. These profound works on MR are also recommended if more in-depth understanding is desired by the reader.

2.1 Spin polarization

A subatomic particle with a nonzero charge distribution spinning about its axis generates a magnetic moment μ, also known as a spin. If the particle has mass, the rotation also includes an angular momentum component. The relation between the angular momentum and the magnetic moment is known as the gyromagnetic ratio, γ. For a nucleus with an odd number of nucleons or protons, the angular momentum cannot obtain a zero-momentum configuration [6]. For MRI, ^{1}H nuclei are typically utilized owing to their abundance in living organs, and because these have one of the highest observable γ values ($2\pi \cdot 42.56$ MHz/T).

In the presence of an external magnetic flux density B_0, magnetic moments of a proton spin ensemble are split between two states, a phenomenon known as Zeeman splitting. The two states correspond to cases where the magnetic momentum components along B_0, denoted as μ_z, are oppositely oriented (cf. Fig. 2.1). The state in which μ_z is parallel to B_0 is the state with lower energy preferred under normal conditions. The energy difference between the states, ΔE, can be formulated through the classical Bohr relation given in

$$\Delta E = \mu_z B_0 = \gamma \hbar B_0, \tag{2.1}$$

where $\hbar$ is Planck's constant divided by 2π. In thermal equilibrium, the distribution between the high-energy state N_α and the low-energy state N_β is Boltzmann distributed and

$$\frac{N_\alpha}{N_\beta} = \exp\left(\frac{\Delta E}{k_B T}\right), \tag{2.2}$$

where k_B is Boltzmann's constant and T is the temperature in kelvins.

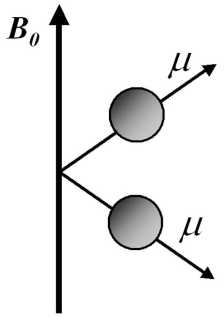

Fig. 2.1. *A spin in the presence of a magnetic field may align itself to either a parallel or an antiparallel state. The energy difference of the states is the origin of nuclear magnetic resonance.*

In a spin ensemble, a nonzero value of the bulk magnetization $\mathbf{M}$ is experienced as a result of the polarizing effect of the flux density B_0 (cf. Fig. 2.2). At room temperature, Curie's law gives the total magnetization over a volume V, with a spin density n; thus,

$$\mathbf{M} = \frac{1}{V}\sum \mu_z \hat{\mathbf{u}}_z = \frac{n(\gamma\hbar)^2 J(J+1)B_0}{3k_B T}\hat{\mathbf{u}}_z, \tag{2.3}$$

where n is the spin density per unit volume, J is the spin quantum number, and $\hat{\mathbf{u}}_z$ is the unit vector along the z axis (i.e., the axis pointing along B_0).

The amount of bulk magnetization relates to the number of spins relevant to the generation of MR signals. If one combines Eqs. 2.1 to 2.3, the bulk magnetization is seen to have a linear dependency on the polarizing field. This has been the motivation for gradually increasing magnetic field strengths in NMR spectrometers and MRI scanners.

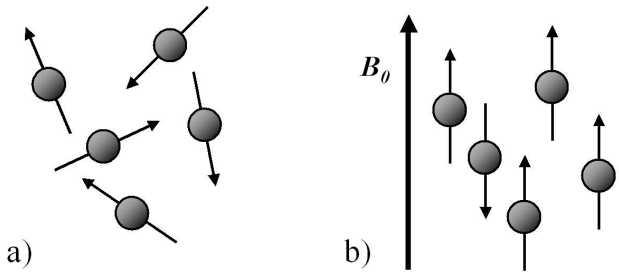

Fig. 2.2. *In the presence of a magnetic field, the probability that spins are aligned along the magnetic field increases, giving a rise to a net bulk magnetization.*

2.2 Spin excitation

By absorbing a photon, a spin can flip into a higher energy state and hence become antiparallel to the background field (cf. Fig. 2.3). Flipping back to the original state of low energy generates a photon. Nuclear magnetic resonance by definition is the irradiation of electromagnetic fields at a frequency matching the energy difference between the two spin states. This frequency is known as the Larmor frequency, ω. From Eq. 2.1, the relation between the Larmor frequency and the flux density B_0 can be derived, and for a spin 1/2 system one can write

$$\omega = \gamma B_0. \tag{2.4}$$

The total process of increasing the antiparallel spin population by radiating spins with an RF pulse is referred to as spin excitation. One of the most important factors of spin excitation is that the excitation generates coherence of the transverse spin components of the spin ensemble. This coherence at the quantum level reflects a macroscopic transverse magnetization that precesses at the Larmor frequency.

By relying on classical physics, the excitation process is depicted as a torque induced to a bulk magnetization by an external magnetic field. Thus, the equation of motion becomes

$$\frac{d\mathbf{M}}{dt} = \gamma \mathbf{M} \times \mathbf{B}, \tag{2.5}$$

where $\mathbf{B}$ is the superposition of static and radiating magnetic flux densities.

The excitation field can be divided into two circularly polarized fields in the xy plane with amplitudes corresponding to flux densities of B_{1+} and B_{1-}. Here, "$-$" indicates clockwise rotation and "+" indicates counterclockwise rotation.

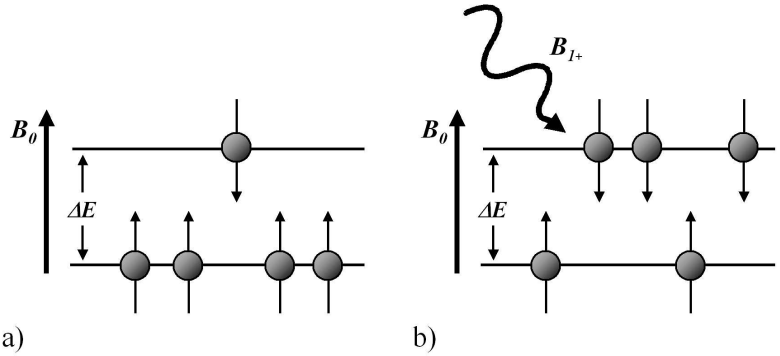

Fig. 2.3. *A spin can absorb a photon at the Larmor frequency and consequently flip into the higher, antiparallel energy state.*

Only the field component rotating along the spin precession is relevant for spin excitations. The effective spin rotating field ($\mathbf{B}_{eff}$) can be derived from Eq. 2.5 as

$$\mathbf{B}_{eff} = \hat{\mathbf{u}}_z \left(B_0 - \frac{\omega_r}{\gamma} \right) + \hat{\mathbf{u}}'_x \frac{B_{1-}}{2}, \tag{2.6}$$

where ω_r is the angular frequency of the excitation field and $\hat{\mathbf{u}}'_x$ is the x coordinate of a rotating frame, in which the spin magnetization is stationary. Figure 2.4 illustrates the excitation process with respect to the rotating frame. The rotation of the spins is most effective when $\omega_r = \gamma B_0$, and hence when the excitation field resonates with the spin ensemble.

In a 3.0-T background flux density, the precession corresponds approximately to a frequency of 127.7 MHz in ^{1}H nuclei. The transverse excitation field in MRI systems is generated by resonating RF coils, into which appropriate power levels at the Larmor frequency are fed [44, 45, 46].

2.3 Spin relaxation

After the excitation, spins start to relax toward the thermal equilibrium state. The behavior in a stationary coordinate system is illustrated in Fig. 2.5. The relaxation process is different for the longitudinal and the transverse magnetizations. The equations of the motion, better known as the Bloch equations, become

$$\frac{d\mathbf{M}_z}{dt} = \gamma(\mathbf{M} \times \mathbf{B})_z - \frac{M_0 - M_z}{\mathrm{T1}}, \tag{2.7}$$

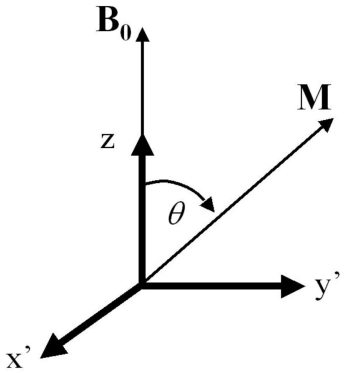

Fig. 2.4. *In the classical description, an RF excitation field applies a torque to the bulk magnetization of the spins and tilts it away from the direction of the background magnetic field. The coordinate frame here is set to rotate along the spin precession and the exciting RF field is seen to point toward the x' axis*

$$\frac{d\mathbf{M}_{x,y}}{dt} = \gamma(\mathbf{M}\times\mathbf{B})_{x,y} - \frac{M_{x,y}}{\mathrm{T2}}. \tag{2.8}$$

where M_0 stands for the thermal equilibrium magnetization and T1 and T2 are relaxation time constants for the longitudinal and transverse magnetizations, respectively.

After a pulse excitation that flips the magnetization toward the transverse plane, Eqs. 2.7 and 2.8 predict an exponential decay for the transverse magnetization and a$[1-\exp(-t/\mathrm{T1})]$ recovery for the longitudinal one. The decaying transverse magnetization is better known as the free induction decay (FID). For the general solution of the Bloch equations, the reader is referred to the book by Abragam [47].

The relaxation times are dependent on the material parameters *in situ*. The longitudinal T1 relaxation is also referred to as spin-lattice relaxation. It describes how effectively the energy stored in excited spins is transferred to the surrounding lattice to return to the equilibrium state. The transverse T2 relaxation is referred to as spin-spin relaxation. It illustrates how strongly the background field experienced by a spin is disturbed by neighboring spins.

A higher level of incoherency in the Larmor frequencies of the spin ensemble caused by the background field inhomogeneity relates to a stronger dephasing effect and subsequent signal loss. Typically, the relaxation constant T2* is utilized instead of T2 to take account of both effects. Thus,

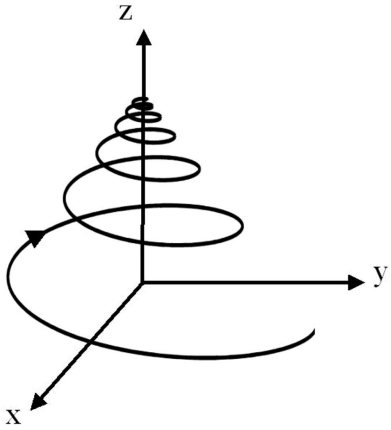

Fig. 2.5. *Bulk magnetization relaxes toward thermal equilibrium after an RF excitation. Owing to the precessing motion of the spins, a spiral-shaped trajectory of magnetization results in the laboratory frame.*

$$\frac{1}{\mathrm{T2}*} = \frac{1}{\mathrm{T2}} + \frac{1}{T_{inhomog.}}, \tag{2.9}$$

where $T_{inhomog.}$ is a time constant describing the level of field inhomogeneity.

2.4 Signal detection

A precessing transverse magnetization generates a time-varying magnetic field at radio frequencies and the signal is typically detected by a receiver coil. In its simplest form, the coil can be a single conductive loop perpendicular to the main magnetic field. As stated by Faraday's law of induction, a time-varying magnetic field causes a curl of an electric field **E** and

$$\nabla \times \mathbf{E} = -\frac{d\mathbf{B}_{1-}}{dt}. \tag{2.10}$$

In a loop c closed over an area A, this leads into an induced electromotive force U, and thus

$$U = \oint_c \mathbf{E} \cdot dl = -\frac{d}{dt} \int_A \mathbf{B}_{1-} \cdot d\mathbf{S}. \tag{2.11}$$

For increased signal coupling to the receiver electronics, the coils are electrically tuned to resonate at the Larmor frequency of the selected nuclei in a given background field strength. The electrical resonance is achieved by utilizing either

lumped elements, i.e., capacitors and inductors, or transmission lines, in which standing waves emerge. The latter becomes more feasible at higher operating frequencies (>200 MHz).

Based on the principle of reciprocity, a transmit RF coil can be utilized for RF detection with comparable performance. Separate local receive or transmit-receive coils are often preferred as received signal levels are increased if the sensing coil is placed closer to the region of interest [41, 46, 48].

2.5 Spatial encoding

For MRI applications, spatial differentiation of signals is required over the region of interest. In a one-dimensional case, a linear magnetic field gradient across the object of interest ensures that for each location there is a corresponding Larmor frequency. This is also known as the read-out gradient as the signal is sampled simultaneously to the applied gradient.

A second linear gradient perpendicular to the first one is utilized to differentiate the phases of the signals from different spatial locations. This occurs before the read-out gradient. Figure 2.6 illustrates the utilization of phase- and frequency-encoding gradients. In MRI, the plane perpendicular to the magnet symmetry axis is customarily referred to as the xy plane, and the symmetry axis of the magnet bore becomes the z axis.

If two-dimensional images are acquired, the spins are excited only at the selected slice, thereby avoiding any interferences from spins beyond the slice. The gradient is applied perpendicularly to the image slice, and the frequency spectrum of the RF excitation pulse is adjusted to match the Larmor frequencies of the spins in this slice. In three-dimensional imaging, the third imaging dimension is phase encoded in a similar fashion to the second dimension. Thus, if the three-dimensional applied gradient waveform $\mathbf{G}(t)$ is

$$\mathbf{G}(t) = G_x(t)\hat{\mathbf{u}}_x + G_y(t)\hat{\mathbf{u}}_y + G_z(t)\hat{\mathbf{u}}_z, \tag{2.12}$$

the phase of the MR signal from a spin, $\varphi(t,\mathbf{r})$, becomes

$$\varphi(t,\mathbf{r}) = \int_0^t (\gamma\mathbf{G}(\tau))\cdot\mathbf{r}d\tau = \left(\gamma\int_0^t \mathbf{G}(\tau)d\tau\right)\cdot\mathbf{r}. \tag{2.13}$$

Here $\mathbf{r}$ indicates the spatial location of a spin isochromat. The image-encoding space is better known as k space and Eq. 2.13 can be rewritten as

$$\varphi(t,\mathbf{r}) = \mathbf{k}(t)\cdot\mathbf{r}, \tag{2.14}$$

and thus

$$\mathbf{k}(t) = \gamma \int_0^t \mathbf{G}(\tau) d\tau. \tag{2.15}$$

A simple relation exists between the image resolution Δx and the maximum k-space-encoding value applied in the same direction, k_x:

$$k_x = \frac{\pi}{\Delta x}. \tag{2.16}$$

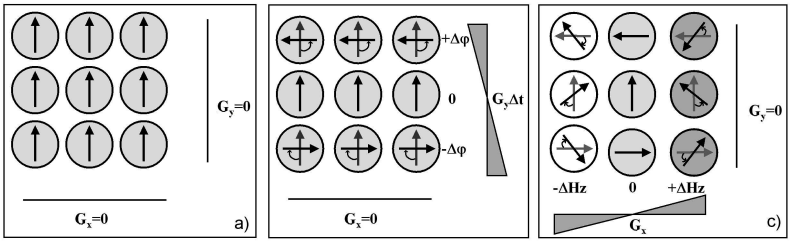

Fig. 2.6. *A gradient pulse of length Δt is applied (a) to introduce a phase difference in the precession of spins in one dimension (b). The second gradient forces spins to rotate at different Larmor frequencies in the second dimension (c). This introduces further dephasing. Here, the background color of the symbols indicates the Larmor frequency and the direction of the arrow indicates the phase.*

2.6 Image reconstruction

A signal detected by a receiver RF coil, $S(t)$, is an integral over individual spins over the whole excited volume, V. Thus,

$$S(t) = \omega \int_V \Psi_-(\mathbf{r}) M_{x,y}(\mathbf{r}) e^{i\mathbf{k}(t)\cdot\mathbf{r}} dV, \tag{2.17}$$

where the receiver sensitivity of the coil is denoted as $\Psi_-(\mathbf{r})$. In this notation, the influence of the Larmor-frequency-related term, ωt, is subtracted from the signal-phase term for simplicity. It should also be observed that the exponential term in Eq. 2.17 is the Fourier image-encoding kernel. Thus, the image reconstruction is simply done by applying the inverse Fourier transform to the detected signal (cf. Fig. 2.7).

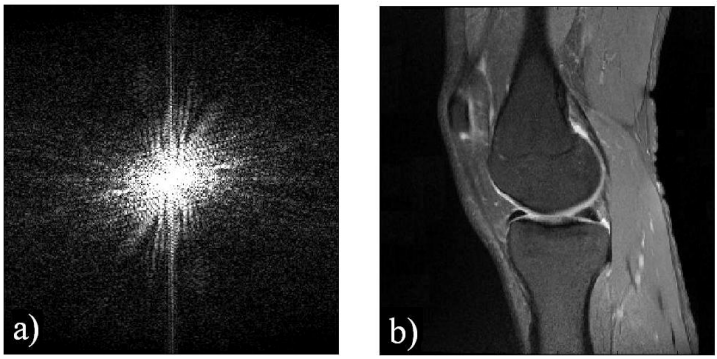

Fig. 2.7. *Example of an MRI image reconstruction, where (a) raw data received by an MRI scanner is converted into (b) the desired image of a human knee through the Fourier transform.*

2.7 MRI system overview

An illustration of a clinical MRI scanner is shown in Fig. 2.8. The device consists of coaxial elements where the outermost one is the superconductive magnet generating the strong background field for spin polarization. For clinical use, polarizing field strengths typically correspond to magnetic flux densities between 0.5 and 3.0 T. For research use, the highest field strength scanner made for human studies has a 9.4-T flux density over its field of view [49].

A set of three gradient coils is placed inside the superconductive coil to generate gradient fields for image encoding. The most common way to generate xy gradients is to utilize a set of interleaved saddle coils, where the z gradient is generated with a Helmholz coil. Gradient strengths can reach values of 50 mT/m in present-day clinical scanners.

The innermost part of the scanner is the whole-body RF coil for spin excitation and detection. During a spin excitation several tens of kilowatts of RF power can be driven into such a whole-body coil. To ensure patient safety, the maximum RF field strength and deposited heat energy, i.e., specific absorption rate (SAR), are controlled by federal standards [50, 51]. When studying a defined anatomical region, such as a knee, local transmit-receive and receive-only coils are typically utilized for higher signal-to-noise ratio.

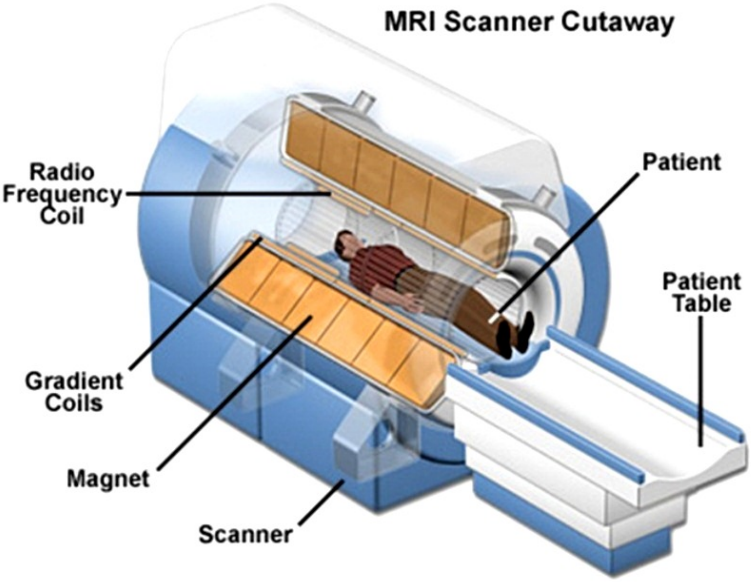

Fig. 2.8. *A cross-sectional illustration of a clinical MRI scanner showing the superconductive main magnet coils, the gradient coils, the RF coil, and a patient laying on a patient table. (The figure is reprinted with the permission of the National High Magnetic Field Laboratory, Tallahassee, FL, USA.)*

3

Attribute Requirements for Magnetic Field Monitoring in MRI

In this chapter, performance requirements for a field monitoring system for MRI are derived based on prior knowledge of clinical MRI systems and on MR image-encoding simulations. The aim of this chapter is to derive a set of criteria that should serve as performance references for the subsequent screening of magnetometer techniques.

3.1 Precision and drift

The performance requirements for a magnetic field monitoring system are closely dependent on the MRI system to which the hardware is implemented. In this work, a clinical 3.0-T MRI scanner (3T Signa Excite, GE Healthcare, Milwaukee, WI, USA) functions as a platform for validating the developed magnetic field monitoring techniques. The scanner manifested capabilities that are achievable by modern clinical MRI devices. The relevant operational characteristics are the maximum gradient strength of ± 40 mT/m, the maximum gradient slew rate of 150 T/m/s, and the maximum field of view of 40 cm.

Simulations were conducted to derive the precision requirement for a magnetic field monitoring system. With Fourier gradient encoding, the k-space location at a certain time point is determined by the gyromagnetic ratio and the gradient waveform according to Eq. 2.15. A generic MR raw data set was derived from the Shepp-Logan phantom with a single-shot EPI k-space trajectory sampling [52]. The ideal single-shot EPI k-space trajectory was assumed to exactly follow a Cartesian grid of matrix size 256. Since the EPI trajectory is a perfect mesh grid, one can neglect the effect of gradient limitations in the simulations.

Error sources corresponding to linear drift ($\Delta\mathbf{k}_{drift}$), random uncertainty in measured k-space location ($\Delta\mathbf{k}_{noise}$), and timing offsets (t_0) were subsequently introduced into the ideal imaging trajectory. The effective image-encoding k-space trajectory ($\mathbf{k}_{eff}$) can be expressed in this case as

$$\mathbf{k}_{eff}(t) = \mathbf{k}(t+t_0) + \frac{2\pi}{\mathrm{FOV}}\left(\Delta\mathbf{k}_{noise} + \frac{t+t_0}{T_{acq}}\Delta\mathbf{k}_{drift}\right), \tag{3.1}$$

with FOV describing the field of view and T_{acq} the acquisition period. According to Eq. 3.1, $\Delta\mathbf{k}_{drift}$ and $\Delta\mathbf{k}_{noise}$ were given in normalized k-space units of 2π/FOV. Single-shot EPI k-space data were obtained by an inverse gridding of the Shepp-Logan phantom along the corrupted k-space trajectory. Subsequently, the k-space data were reconstructed via gridding by assuming an undistorted k-space trajectory.

To quantitatively study the level of image artifacts, an error norm was introduced according to

$$\frac{\sum_{i,j=0}^{N,M} |S_{dist}(i,j) - S_{true}(i,j)|}{\sum_{i,j=0}^{N,M} |S_{true}(i,j)|} \leq 10^{-2}, \tag{3.2}$$

where i and j are the pixel indices and S_{dist} and S_{true} are the pixel values of the distorted and true image, respectively. Figure 3.1 illustrates image artifacts resulting from random error and linear drift in k-space trajectories.

The relation between $|\Delta\mathbf{k}_{noise}|$ and the precision of the field measurements, $\Delta B_{\mathrm{noise}}$, can be written as

$$\frac{2\pi}{\mathrm{FOV}}\,|\Delta\mathbf{k}_{noise}| = \sqrt{2}\gamma\frac{\Delta B_{noise}}{|\mathbf{r}|}\Delta t, \tag{3.3}$$

where the imaging sampling interval is Δt. Typically the magnetic field sensors are placed close to the edges of the FOV, i.e., $|\mathbf{r}| \approx \mathrm{FOV}$. The factor $\sqrt{2}$ in the uncertainty of monitoring the k-space trajectory arises from the fact that the noise of two magnetic field sensors is assumed to be uncorrelated. The assumption is expected to be justified for NMR probes, of which noise is coil dominated and the cross-coupling is insignificant owing to the large probe-to-probe distance.

Similarly, the relation between field measurement drift, ΔB_{drift}, and k-space drift can be written as

$$\frac{2\pi}{\mathrm{FOV}}\,|\Delta\mathbf{k}_{drift}| = \sqrt{2}\gamma\frac{\Delta B_{drift}}{|\mathbf{r}|}T_{acq}. \tag{3.4}$$

Thus, drift-related measurement errors become more detrimental for imaging at longer acquisition periods. Therefore, sensors suffering from high levels of $1/f$ noise are less suitable for rMFM.

Based on the simulations, it was concluded that $\Delta B_{noise}\Delta t = \sqrt{2}\pi\,|\Delta\mathbf{k}_{noise}|\,/\gamma \leq$ 53 pTs does not violate the error norm criteria. From Eq. 3.3, one notes that longer imaging sampling intervals set higher precision requirements for field sensing. If imaging and monitoring sampling rates are considered to be separate, the Nyquist limit for the relevant gradient activity limits the minimum monitoring bandwidth. Based on typical specifications of an MRI scanner, gradient activity is considered to be below 25 kHz. With a sampling rate fulfilling the Nyquist criterion, it is obtained from Eq. 3.3 that $\Delta B \leq 2.7\ \mu$T, i.e., 12 nT/$\sqrt{\text{Hz}}$.

For the maximum applicable measurement drift, a criterion is derived from Eq. 3.4 that $\Delta B_{drift} T_{acq} = \sqrt{2}\pi\,\left|\Delta\mathbf{k}_{drift}\right|/\gamma \leq 170$ pTs with $|\mathbf{r}| = \text{FOV}$. In typical MRI experiments, acquisitions can be up to 100 ms long, and the criterion transforms to a measurement drift of $\Delta B_{drift} \leq 1.7$ nT.

3.2 Synchronization and sampling clock jitter

Drift and jitter in the clock signal of a magnetometer system influence how accurately monitoring data and MRI signals can be aligned in temporal space. The effect of timing-related errors in field monitoring data was studied by introducing a time offset, t_0, to Eq. 3.1. The error norm of Eq. 3.2 was likewise applied, and the criterion was found to be fulfilled if $t_0 < 40$ ns. This synchronization limit is well above values that are typically obtained with hardware designs based on phased-locked-loop electronics and shared clock signals.

The error maximum in measured k-space trajectories from clock jitter occurs when encoding gradients are at their maximum value. If one combines Eqs. 2.15 and 3.3, a criterion for the level of clock jitter can be written as

$$\Delta t_{jitter} \leq \frac{2\pi\,|\Delta\mathbf{k}_{noise}|}{\gamma\, G_{max}\,\text{FOV}}. \tag{3.5}$$

In Section 3.1, the result $\sqrt{2}\pi\,|\Delta\mathbf{k}_{noise}|\,/\gamma \leq 53$ pTs was obtained for the precision requirement of field monitoring. This result, combined with the given values of $G_{max} = 40$ mT/m and FOV = 40 cm, gives a criterion of $\leq$4.7 ns for sampling clock jitter. Typically, jitter levels that are experienced with voltage-controlled crystal oscillators are several orders of magnitude lower than the derived criterion.

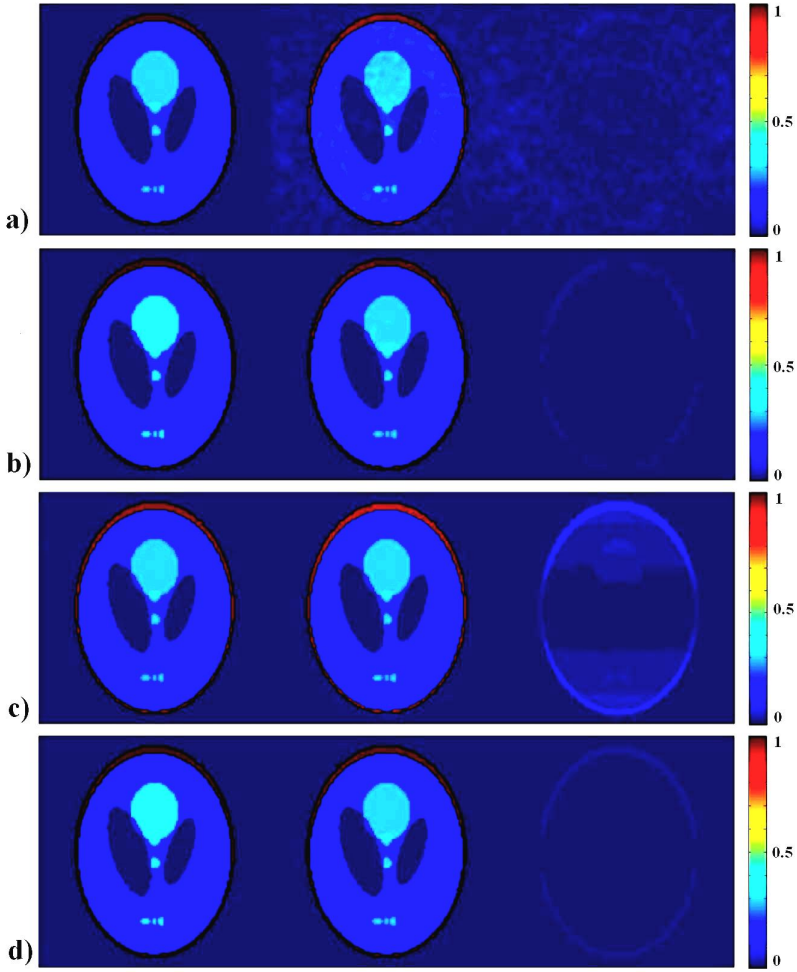

Fig. 3.1. *Simulated images of a Shepp-Logan phantom based on a single-shot EPI trajectory. True images are shown on the left, distorted images are at the center, and difference images are on the right. The color scale shows the normalized signal strength. In the distorted images on the two top rows, a random uncertainty into applied k-space trajectories was introduced to correspond to error norms of (a) 0.1 and (b) 0.01. On the bottom two rows, a linear drift was introduced to similarly correspond to error norms of (c) 0.1 and (d) 0.01.*

3.3 Electromagnetic compatibility and patient safety

In his article, Schenck [53] has studied the MRI compatibility of magnetically different materials. Soft and hard ferromagnetic materials experience strong forces and torques inside an MRI scanner, and such materials can generate significant image distortions even if placed far away from the patient. These materials are considered to be MRI incompatible and their use should be highly restricted.

Materials that do not experience strong forces or torques in a magnetic field and do not cause image artifacts as long as they are not placed in close proximity of a patient are considered to be MRI compatible materials of the first kind. Such materials are specified to have volume susceptibility of ≤ 0.01. Titanium and stainless steel are examples. Because these examples are conductive, noticeable Lorentz forces during gradient activity can however be induced if the objects are large in size.

Material	**Susceptibility [ppm]**
Silver	-24.0
Lead	-15.8
Pyrex glass	-13.9
Epoxy	$\sim(-12$ to $-9.0)$
Human tissue	$\sim(-11$ to $-7.0)$
Copper	-9.63
Nylon	-9.10
Water	-9.05
Heavy water	-8.99
Fluorinert (FC-43)	-8.2
Silicon	-4.2
Hemoglobin	0.15
Air (NTP)	0.36
Tin	2.4
Aluminum	20.9

Table 3.1. *List of selected MRI-compatible materials given with the corresponding susceptibility values [34, 53, 54, 55, 56, 57].*

Materials of the second kind of MRI compatibility do not experience strong forces or torques and do not create image artifacts even if these are placed close to or within the field of view. The susceptibility value of such materials should not differ by more than 10 ppm from the value of water (i.e., -9.05 ppm). In Tab. 3.1, some materials of the second kind of MRI compatibility are listed with susceptibilities of a few other elements relevant for MRI. Because sensors for magnetic field monitoring are placed close to or within the field of view, magnetic compatibility of the second kind is required.

During the RF excitation phase of MRI acquisitions, several kilowatts of RF power can be supplied inside the magnet bore. The magnetic fields generated with these power levels can induce damaging voltages to electronic devices if adequate protection is neglected. RF pulsing can also lead to strong electric fields at the vicinity of any conductive structures. These electrical fields can consequently lead to a local breaching of the SAR limits, which are set by federal standards, potentially causing injurious burns to a patient. When designing hardware for clinical applications, patient safety should be the first priority, and it should also be carefully addressed in the design of a magnetic field monitoring system for MRI. For further reading on the topic of MRI safety, see the review article by Shellock [58].

3.4 Other design considerations and summary

A magnetometer system for real-time field monitoring should be easily integrated into a clinical MRI system, and it should require no modifications with respect to existing hardware or pulse sequences. The magnetic field monitoring system should not create a significant cost burden for a clinical MRI device either. Thus economically feasible solutions with robust functionality should be favored. Device integration to existing receiver coils, gradient inserts, or stereotactic frames should be considered. In practice, this requirement would limit the total sensor size to several centimeters or less. In Tab. 3.2, the requirements derived in this chapter for a potential magnetometer system for magnetic field monitoring assisted MRI are summarized.

Requirement	**Value**
B_0	3.0 T
B_0 swing	$\pm$10 mT
Precision	3 nT/$\sqrt{\text{Hz}}$
Drift	$<$1.7 nT @ 10 Hz
Nyquist bandwidth	$\sim$50 kHz
Dynamic range	90 dB @ 50 kHz
Timing error	$<$40 ns
Sampling clock jitter	$<$4.7 ns
MRI compatibility	second kind

Table 3.2. *Sensor requirements for real-time magnetic field monitoring in MRI.*

4

Magnetometers and Application to Magnetic Field Monitoring in MRI

Available techniques for magnetic field sensing are introduced in this chapter. The sensing concepts are divided into subcategories roughly based on their principle of operation. Many such divisions are possible, and the one presented here is by no means exclusive. The goal of the literature search in this chapter is to study which of the available techniques are feasible for magnetic field monitoring in MRI. The screening of magnetometers is based upon the requirements concluded in the previous chapter. A summary of the magnetometers available along with a decision on which technologies to chose for further studies concludes this chapter. For further reading, references such as [59, 60, 61, 62] are encouraged. For a comprehensive list of magnetometer manufacturers, reference [62] is recommended. Throughout the text, the quantity of the magnetic flux density is preferred over the magnetic field strength. This decision is based on the governing practice in the MRI community.

4.1 Faraday induction magnetometers

4.1.1 Pick-up coils

As is stated by Faraday's law of induction (cf. Eq. 2.10), a temporal change of a magnetic field causes a curl of an electric field. This induces an electromotive force into a conductive loop, as is given by Eq. 2.11, and by resolving the time integral of the detected signal one obtains a measure of the applied magnetic flux density [59, 60, 62].

Pick-up coils are one of the most versatile magnetometers available. One can optimize the performance characteristics of pick-up coils to a large extent

by changing the coil cross-sectional area, the number of turns, and the core permeability. Pick-up coils for detecting flux densities as small as 20 fT have been manufactured [59]. Air-core coils are preferred for measuring high field strengths as ferromagnetic cores saturate at fields that corresponds to 10-100 mT flux densities in vacuum; as with air-core coils, no upper limit for measurable field strengths exists.

A drawback of this technique is that measurement of DC fields is not possible and noticeable drift-related errors in measurements are experienced at lower frequencies owing to the detection scheme requiring a time integral of the signal. Beyond the $1/f$ noise regime, precisions on the order of 10 ppm/$\sqrt{\text{Hz}}$ or spectral noise densities of 20 fT/$\sqrt{\text{Hz}}$ can be expected. The threshold frequency for $1/f$ noise depends upon the coil geometry and core material, and it is commonly on the order of 10 Hz to 1 kHz. An upper limit for a measurement bandwidth is in practice set by the self-resonance of the coil, and this can be shifted above gigahertz values by reducing the number of turns and the cross-sectional area. With ferromagnetic cores, however, the self-resonance and the intrinsic losses limit the high-frequency operation to below 1 MHz.

4.1.2 Flux-gate magnetometers

In a flux-gate magnetometer, a drive and sense coil are sharing the same soft magnetic core [59, 60, 62]. The sensing concept is based on the hysteretic characteristic of soft magnetic materials when driven into and out of saturation. Generally, a sinusoidal signal is used for this purpose, and it is fed into a drive coil. During periodic saturation of the magnetic core, the external magnetic flux is either attracted to or repelled from the core. The nonlinear behavior results in a harmonic mixing of the components of these two signals. Typically, the second harmonic is utilized, and effective filtering is required to eliminate the influence of the other harmonics.

One benefit of flux-gate sensors over pick-up coils is that measured voltages are directly proportional to the magnetic field strength being measured. Thus, no integrative detection scheme is required, and truly DC field measurements become possible. Owing to the absence of the signal integration, the technique is less prone to $1/f$ noise. However, flux-gate magnetometers do suffer from higher spectral noise density than air-core pick-up coils beyond the $1/f$ noise regime. This is due to Barkhausen noise in the soft magnetic cores. Intrinsic noise values down to 30 pT/$\sqrt{\text{Hz}}$ are achievable with flux-gate sensors. Beyond the sensitivity limit, field measurements with precisions around 50 ppm/$\sqrt{\text{Hz}}$ are typically achieved.

In practice, flux-gate sensors can detect signals up to amplitudes corresponding to 10-mT flux densities. The upper boundary of field measurements is limited by the high AC power levels required and by the relatively long response time of the ferromagnetic core. The response time of the core also restricts the upper limit of the measurement bandwidth, which is on the order of 10 kHz.

4.2 Hall-effect devices

A magnetic field applied perpendicular to an electric current deviates propagating charges from their original linear path. The deflecting force, perpendicular to both the magnetic field and the current, is known as the Lorenz force. This deflection of the charge carriers and the consequent voltage buildup is known as the Hall effect, which is utilized for magnetometric applications in various configurations.

4.2.1 Hall plate magnetometers

One of the most simple structures with which to observe the buildup of Hall voltages is a rectangular plate in which a drive current is fed into two ends of the plate and sense nodes are placed perpendicular to this axis [61, 62, 63, 64]. To have a high power efficiency, the substrate should have a small number of charge carriers with high mobility. Materials that best fulfill these requirements are semiconductors, especially gallium arsenide, indium antimonide, and silicon.

The sensitivity of a Hall plate depends on the material chosen. Indium-antimonide-based sensors offer the highest sensitivity, reaching 100 pT/$\sqrt{\text{Hz}}$. If silicon is chosen for the material, the sensitivity is clearly higher, typically on the order of 100 nT/$\sqrt{\text{Hz}}$. Hall plates are influenced by $1/f$ noise and typical 1/5 noise knee frequencies are between 1 and 10 kHz, depending on the material. Above the sensitivity limit, measurement precisions on the order of 10 ppm/$\sqrt{\text{Hz}}$ are typically obtained. In theory, there is no maximum value for field strengths that can be detected with Hall plates, and measured flux densities as high as 23 T have been reported [63]. Measurement bandwidths are limited by sensor noise and are typically not above 1 MHz.

4.2.2 MOSFET magnetotransistors

In a metal-oxide-semiconductor field-effect magnetotransistor (MAGFET), the normal operation as a field-effect transistor produces the drive current for the

Hall effect [61, 65, 66, 67, 68]. The fundamental difference from a standard field-effect transistor is that there are Hall sense nodes at both sides of the channel.

In another MAGFET design, a transistor with two drains is constructed. An applied magnetic field deflects the charges in a way such that the current through one drain is increased, while it is reduced in the other one. The imbalance between the drain currents becomes the measure of the magnetic field.

One of the advantages of magnetotransistors is the possibility of having a sensor element as a part of the read-out and signal conditioning circuitry. Silicon MAGFETs have an order of magnitude higher spectral noise density in comparison to Hall plates, and sensitivities close to 1 μT/$\sqrt{\text{Hz}}$ can be expected. Values close to 1 000 ppm/$\sqrt{\text{Hz}}$ have been reported for the signal-to-noise ratio in the nonsensitivity-limited region. The upper boundary for detectable field strengths is limited by the practicality of the implementation and is typically on the order of 1 T. Typical measurement frequencies can range up to 1 MHz.

4.2.3 Magnetodiodes

A magnetodiode resembles a standard pn-junction diode with an intrinsic region in between the p and the n regions [59, 61, 64, 69]. The magnetic field deflects flowing charges in the intrinsic region from their straight path. The holes and the electrons are mutually bent toward one of the device edges, which leads to a lengthening of the current lines and consequently to an increased recombination rate. Both of these effects reduce the saturation current, thus relating magnetic field strength to a change in the characteristic exponential current-voltage curve of a diode.

Sensitivities of magnetodiodes are at the same order of magnitude as they are for silicon Hall plates. The highest measurable field limit is in practice on the order of 1 T. The noise and the bandwidth characteristics of magnetodiodes are comparable to other Hall-effect-based semiconductor devices.

4.2.4 Bipolar magnetotransistors

In bipolar junction transistors, the Hall effect can be exploited in several ways for magnetometric purposes [59, 61, 70]. A bipolar transistor with two collectors resembles the operation principle of the dual-drain MAGFET construct. Thus, the charge carriers in this design are deflected by the Lorentz force, which leads to unbalanced collector currents.

Another bipolar transistor structure for magnetic field sensing is to have the base replaced by a Hall plate. By applying a biasing current, the Hall effect

modulates the current injection by changing the electrical potential along the base.

A third common bipolar magnetotransistor structure is based on the same effect as magnetodiodes. In this magnetotransistor design, two transistors have a common emitter. The requirement for the operation as a magnetometer is that the transistor is in a high injection state, thus a large number of minority charge carriers are flowing through the substrate. An applied magnetic field increases the concentration of charge carriers in one of the transistors, i.e., decreasing the base-emitter resistance. In the other transistor, the base-emitter resistance is simultaneously increased, and the difference in the resistances becomes the measure of a detected magnetic field.

In practical implementations of bipolar magnetotransistors, the described effects are either exploited individually or as a combination. Bipolar magnetotransistors are expected to have sensitivities 100 times better than silicon Hall plates partly becasue of the clearly lower $1/f$ noise knee frequency (typically $<$10 Hz). The intrinsic white-noise density in bipolar magnetotransistors can be as low as 10 nT/$\sqrt{\text{Hz}}$. The maximum detectable flux densities with bipolar magnetotransistors lay in the region of 1 T and are limited by the practicality of the implementation. Measurement bandwidths are constrained by the level of noise and are typically between 1 kHz and 1 MHz.

4.3 Magnetoresistive magnetometers

In magnetoresistive materials, a change in a magnetic field across the sensing element alters material properties in such a way that the conductivity of the material changes. In typical measurements, magnetoresistive elements are connected to a Wheatstone bridge configuration [71, 72].

4.3.1 Extraordianary magnetoresistance

An extraordinary magnetoresistance (EMR) sensor is based on the inhomogeneity domains of high conductivity implanted into a semiconductor substrate [73, 74, 75]. One example of such a geometry is a circular gold plate surrounded by a coaxial semiconductor disk (cf. Fig. 4.1). Classical electromagnetism states that at a boundary of a conductor and an insulator the electric field will be perpendicular to the surface of the conductor. In the absence of an external magnetic field, charge carriers follow the electric lines and the current flows through the highly conductive disk.

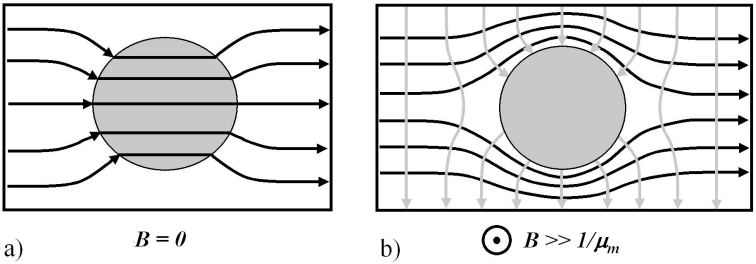

Fig. 4.1. *An EMR sensor based on a conductive disk surrounded by a semiconductor substrate. (a) In the absence of an external field, the current lines (indicated as black lines) conform to the electric field lines (indicated as gray lines), and charge carriers follow the low-resistance path through the disk. (b) If a magnetic field pointing toward the reader is applied, the charge carriers are deflected to a more resistive path, avoiding the highly conductive disk.*

If a magnetic field through the device is applied, the charge carriers are deviated from the original path by Lorenz dispersion. The Lorentz force causes an accumulation of charge carriers at the edges of the device and consequently gives rise to a Hall voltage. If the applied magnetic field is strong enough, the Hall voltage, perpendicular to the original drive voltage, overwhelms. The Lorentz dispersion subsequently forces the current lines to converge toward a 90° angle with respect to the electric field, and a phenomena emerges in which the charge carriers avoid the conductive disk. In this state, the total electrical resistance of the device increases. This phenomena is better known as extraordinary magnetoresistance.

EMR sensors vary from other magnetoresistance sensors in that their operation does not rely on the properties of ferromagnetic materials. EMR sensors exhibit a strong magnetoresistive effect of up to 750 000% at 4 T. A benefit of EMR sensors, over other magnetoresistive sensors, is that they do not suffer from Barkhausen noise nor do they saturate at high fields. Hence, EMR sensors offer high precision (of approximately 10 ppm/$\sqrt{\text{Hz}}$), and in principle there is no maximum limit for the field of operation. Measurement precisions achieved with EMR sensors are approximately 10 pT/$\sqrt{\text{Hz}}$. EMR devices suffer from $1/f$ noise only remotely, and the $1/f$ noise corner frequency is on the order of 10 Hz. Owing to the relatively low spectral noise density, measurement bandwidths can be extended up to 1 GHz.

One drawback of the technique is that a biasing field is required if one needs to measure flux densities lower than approximately 50 mT. EMR-based devices are also still immature and sensor elements are not yet commercially available.

4.3.2 Anisotropic magnetoresistance

In anisotropic magnetoresistive (AMR) materials, the material resistance depends on the angle between the direction of the magnetization and the direction of the current flowing through it [59, 60, 62, 70, 76, 77]. An external magnetic field applied across the sensor element causes the magnetization to turn toward the direction of the field. This rotation alters the density of states at the Fermi Level and leads to a change in dispersion, i.e., in electrical resistance.

To linearize the otherwise quadratic response to the applied magnetic field, several methods have been developed. One of the most typical ones is to tilt the angle between the drive current and the spontaneous magnetization by $\pm 45^\circ$. To minimize the error arising from the offset resistance of the material, a set-reset method has been developed. In this scheme, the direction of the magnetization is flipped by applying a strong magnetization pulse with a short duration.

An alloy containing about 80% nickel and 20% iron provides a magnetoresistive effect of approximately 4%, and it is the material commonly used for AMR sensors. The $1/f$ noise regime of an AMR magnetometer is typically below 10 Hz. Above 10 Hz, an intrinsic white-noise density of 100 pT/$\sqrt{\text{Hz}}$ is achievable. The precisions of AMR sensors in nonsensitivity-limited measurements are on the order of 100 ppm/$\sqrt{\text{Hz}}$. Measured fields should remain below the value that would saturate the sensing material to ensure reliable operation of AMR sensors. Typically, these fields correspond to magnetic flux densities on the order of 10 mT. AMR sensors can be utilized to detect fast field changes, and with open-loop read-out electronics measurement bandwidths can be up to 100 MHz.

4.3.3 Giant magnetoresistance

Giant magnetoresistive (GMR) devices received their name because the magnetoresistive effect in GMR sensors can be up to three times higher than that with the best available AMR sensors [59, 62, 70, 77, 78, 79, 80]. A GMR sensor is based on thin layers of ferromagnetic materials. Here, two thin ferromagnets are separated by a thin conductor (Fig 4.2). In one of the ferromagnets the rotation of its magnetization is inhibited by a strong antiferromagnet deposited in parallel. When the magnetizations of the two ferromagnetic layers are parallel, a traveling electron in the conductor experiences more available states in the band structure of the free ferromagnetic layer. This corresponds to a reduced level of scattering. The opposite is true when an applied field flips the magnetization of the unpinned ferromagnet to an antiparallel state.

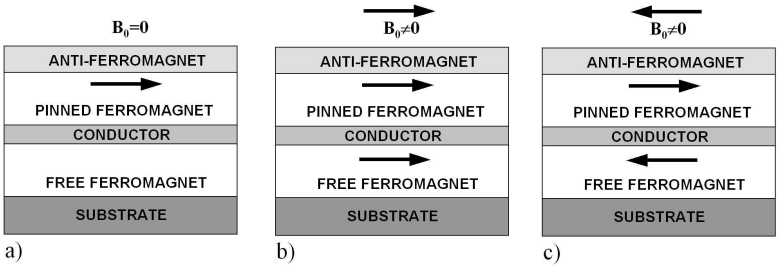

Fig. 4.2. *An illustration of a GMR sensor element. The resistance of the device is reduced from (a) the nominal value if an applied magnetic field is (b) parallel to the magnetization of the pinned ferromagnet. (c) The resistance is increased if the field is antiparallel.*

There are some distinct benefits of GMR magnetometers over AMR ones: namely slightly higher sensitivity and a better temperature stability. GMR sensors do not suffer from offset errors to the same extent as AMR sensors, and hence a set-reset measurement scheme is not required. The $1/f$ noise regime of a GMR sensor depends on its design parameters and is typically between 1 and 100 kHz. Above $1/f$ noise, measurements can be extended to the gigahertz range until the ferromagnetic resonance becomes the limiting factor. The spectral density in the white-noise regime is comparable to AMR sensors, and thus it is on the order of 100 pT/$\sqrt{\text{Hz}}$. The saturation of the ferromagnetic layers in GMR sensors limits the measurable flux densities to below 100 mT.

4.3.4 Magnetic tunnel junctions

A magnetic tunnel junction (MTJ) magnetometer is based on a structure similar to a spin-valve GMR sensor with the distinction that the conducting spacer between the two ferromagnetic plates is replaced by an insulator of $\sim$1 nm thickness [77, 81, 82]. The thinness of the insulator ensures that the conducting electrons can tunnel over it.

MTJ sensors provide magnetoresistive coefficients up to 220%, outperforming any existing GMR sensors. The dominant noise source of a MTJ device is shot noise and the measurement precision in nonsensitivity-limited measurements is typically, despite the higher magnetoresistive effect, slightly poorer than with GMR magnetometers. With respect to the sensitivity, and the maximum field and bandwidth limits, the MTJ sensors resembles their GMR counterparts.

4.3.5 Colossal magnetoresistance

In many ferromagnetic materials, a negative magnetoresistive effect is seen in the vicinity of paramagnetic-ferromagnetic transitions [78, 83]. The magnetic domains start to pin more in one direction when the applied field strength is close to the value where the material becomes ferromagnetic. This reduces the fluctuation of the magnetic domains and the phenomena is subsequently observed as reduced scattering, i.e., resistivity. In materials such as perovskite, $LaMnO_3$, the magnetoresistive effect is higher than in any known GMR sensors (up to 80% at 0°C) , and the phenomena is typically referred to as colossal magnetoresistance (CMR).

An advantage over GMR sensors is that CMR devices can operate reliably at magnetic flux densities above 1 T. CMR sensors do suffer from a high level of $1/f$ noise at room temperature, and typically the precision of field measurements is considered to be significantly worse than with comparable GMR sensors. CMR was recently discovered and no devices based on the effect are commercially available.

4.3.6 Ballistic magnetoresistance

In ballistic magnetoresistance (BMR), the dimensions of a sensing element between two ferromagnets are smaller than the typical scattering paths of electrons [75, 84, 85]. Thus, the trajectory of an electron is now dominated by the influence of an existing magnetic field. Here, electrons are spin polarized by the emitting (ferromagnetic) contact, and the level of the scattering depends on the magnetization state of the collecting ferromagnet.

BMR-based sensors are still immature, but results of up to 3100% in the magnetoresistive effect at room temperature are promising. The noise of the device is expected to be dominated by magnetic and shot noise, and precisions of $1\,000$ ppm$/\sqrt{\text{Hz}}$ can be expected. Flux densities as high as $\sim$100 mT can be measured with BMR sensors before any significant saturation of the device is observed.

4.3.7 Giant magnetoimpedance

Materials showing a giant magnetic impedance (GMI) response exhibit an effect to the total impedance of the conductor in the presence of an external magnetic field [62, 78, 86, 87, 88]. The giant magnetoimpedance effect is based on changes in the transverse susceptibility with respect to the direction of the wave

propagation induced by an external magnetic field. These changes are subsequently observed as alterations of the complex propagation constant and hence in the skin depth the AC signal experiences. The GMI phenomena is seen most strongly in amorphous wires, in ribbons, and in thin films of uniform phase and soft ferromagnetic properties.

For high sensitivity, the operation frequency is set in a way such that the skin depth is clearly smaller than the GMI element diameter. In addition to the Wheatstone bridge measurement scheme, a GMI element can be used as an inductor in an oscillator circuit or in a LC resonator [65, 62].

Magnetoimpedance effects of up to 1 000% have been reported. In comparison to GMR sensors, GMI sensors show slightly better performance with respect to the intrinsic noise, and precisions of 50 ppm/$\sqrt{\text{Hz}}$ are reported. Typically the operation frequencies of GMI sensors are beyond the effective $1/f$ noise regime. The upper frequency limit for the biasing of a GMI sensor is set by the response time of the soft ferromagnetic material. This is reported to be up to 100 Mhz. Commonly, the sensing bandwidth is an order of a magnitude lower than the bias frequency. GMI sensors can measure flux densities of up to 100 μT before the applied field saturates the ferromagnetic sensing element.

4.4 Magneto-optical devices

An external magnetic field can actuate several physical phenomena in magneto-optical devices, which are subsequently observable as changes in the characteristics of visible or near-visible light [59, 62, 89, 90, 91]. These phenomena include splitting of an emission line into two circularly polarized components by a longitudinal magnetic field (i.e., the Zeeman effect), rotation in the polarization plane of linearly polarized light by an applied longitudinal magnetic field (i.e., the Faraday effect), a phase shift between perpendicular and parallel linearly polarized waves by a transverse magnetic field (i.e., the Voigt effect), a change in polarization typically from linear to elliptical as a wave is reflected from a magnetic surface (i.e., magneto-optical Kerr effect), and anisotropy in attenuation of right- and left-handed circular polarization in the presence of a magnetic field (i.e., magnetic dichroism).

Of all the magneto-optical effects, Faraday rotation is found to be the most suitable for magnetometric applications because of the high sensitivity of the effect to magnetic field changes. The Faraday effect arises from the fact that clockwise and counterclockwise polarizations have different indexes of refraction depending on whether the rotation is about the electron rotation in the material or against it. An applied magnetic flux density affects the precession rate

of the electrons, which is subsequently detected as a change in the refractive indexes observed by the two polarizations.

To detect rotation shift in linearly polarized light from the Faraday effect either a polarimetric or interferometric read-out scheme is utilized. In the polarimetric scheme, a linearly polarized laser light is diverted after a magneto-optical fiber to two photodiodes by a polarization beam splitter (i.e., a Glan cube). Of all the optical interferometer designs, the Sagnac interferometer is the most advisable as it cancels the residual birefringence in fiber optics. A lock-in amplifier to match the oscillation of the phase modulation can be utilized to increase the sensitivity at the expense of the measurement bandwidth.

Magneto-optical sensors have a very short response time and sensors operating in the gigahertz range are manufactured. Because of component limitations, the polarimetric scheme is more suitable for high-bandwidth ($>$10 MHz) and high-dynamic-range applications. In contrast, the interferometric approach is advantageous for measurements requiring high sensitivity at slowly varying fields, and values down to 100 pT/$\sqrt{\text{Hz}}$ for sensitivity are reported.

There is no theoretical limit to the highest measurable field strength with magneto-optical devices and magnetic flux densities of several tens of teslas have been measured. Fiber-optic sensors have relatively high measurement uncertainty ($\sim$1 000 ppm/$\sqrt{\text{Hz}}$) owing to high-temperature dependency of the sensing elements and noise in the utilized light sources. However, novel magnetometers based on Bragg grating filters are bringing the polarimetric detection scheme with noncoherent light sources closer to the sensitivities earlier only available with interferometric devices [92].

4.5 Microelectromechanical systems for magnetometry

By definition, a microelectromechanical system (MEMS) is a a micron-sized device and its operation is based on both the electrical and the mechanical properties of the construct. The physical principles of operation in MEMS-based magnetometers can significantly differ from one to another. The unifying factor is the manufacturing process of the devices, which is closely related to the manufacturing of semiconductor devices.

4.5.1 Lorentz force and magnetic torque MEMS

Different magnetometer designs exist that utilize displacements of micromachined cantilevers by forces induced by magnetic fields [59, 93, 94, 95]. If a

current is fed through such a micromachined cantilever, the cantilever is consequently bent or twisted by the Lorentz force. Alternatively, one can manufacture a cantilever sensitive to magnetic fields by depositing hard ferromagnetic material onto the cantilever.

The cantilevers can act as the second plate of variable capacitors in measurement configurations where the change in capacitance is measured with a charge amplifier or observed as a change of resonance frequency in an oscillator circuitry [65]. Optionally, piezoelectric, optical, and tunneling-current-based methods can be utilized to detect the displacement of the cantilever. By driving the cantilever into its mechanical resonance state, the sensitivity is increased in theory by the quality factor of the mechanical resonator. Furthermore, the technique raises the measurement bandwidth farther away from the $1/f$ noise region.

The maximum limit for detectable fields is set by the cantilever spring constant, which can be tailored for the application. Typically, measurable fields as high as 10 mT are reported. Owing to self-resonance effects and the consequent highly nonconstant frequency response, MEMS-based magnetometers are favored for detecting only modestly varying fields ($<$10 kHz). Sensitivity limits of below 1 nT/$\sqrt{\text{Hz}}$ have been reported with a MEMS device based on a Lorentz-force-actuated cantilever with an optical detection scheme for measuring the displacement of the cantilever. More than two orders of magnitude better results can be achieved if tunneling current is utilized to measure the displacement instead.

4.5.2 MEMS flux concentrators

MEMS technology can be utilized to enhance the performance of magnetometers suffering from $1/f$ noise [59, 96]. Soft ferromagnetic flux concentrators on a MEMS cantilever are driven into an oscillating motion that consequently modulates the external field above the $1/f$ noise regime. The magnetometer element itself (e.g., MTJ or GMR) is placed between the flux concentrators for improved sensitivity. At low frequencies, field variations smaller than 10-10^3 with an unenhanced sensor can be observed with the described construct.

4.6 Magnetostriction magnetometers

In magnetostrictive materials, an external magnetic field causes changes in elastic strain [97]. The phenomena is fundamentally based on the reorientations of magnetic domains in ferromagnetic materials for minimum total energy. For magnetostrictive detection schemes, several approaches have been developed.

A magnetostrictive MEMS magnetometer is constructed by depositing a magnetostrictive layer on top of a cantilever. The bending of the cantilever is detected with similar methods as with other MEMS cantilever magnetometers [59, 60, 98].

A device better known as a magnetoelectric device is based on laminated layers of piezoelectric and magnetostrictive materials [99]. In such a construct, a change in the length of the magnetrostrictive material by an external magnetic field is transformed into a voltage across the piezoelement.

In an optical detection scheme of magnetostriction, a sensing element is attached onto an elastic optical fiber [100, 101, 102]. A change in the geometry of the magnetostrictive element by an external magnetic field is converted into a change in the optical length experienced by traveling light. This dimensional change is detected with optical phase detectors or, more accurately (however, at the expense of bandwidth), with Mach-Zehnder or Michelson interferometers, for example.

Magnetoelectric and magnetostrictive fiber-optic magnetometers have sensitivities down to 10 pT/$\sqrt{\text{Hz}}$, thus outperforming cantilever-based magnetostrictive MEMS sensors, which typically have sensitivities of 100 nT/$\sqrt{\text{Hz}}$. Since the magnetostriction sensors are based on soft magnetic materials, these sensors get saturated at high magnetic fields. Magnetic flux densities above 10 mT are considered to be beyond the detection range. To avoid nonlinear effects in the measurement response at low fields, magnetostrictive sensors are biased with flux densities close to the millitesla regime. Measurement bandwidths are limited to relatively low values by the ferromagnetic resonances in utilized magnetrostictive materials, and time- invariant fields only up to 60 kHz are reported to be measured.

4.7 Superconductive magnetometers

At low temperatures, current flow in certain materials cease to obey the classical Ohm's law. Below the so-called critical temperature, conductive charge carriers condense into pairs known as Cooper pairs and the material becomes superconductive. In addition to being a lossless conductor, phenomena known as flux quantization and the Josephson effect can arise. These phenomena give the basis for Meissner-effect-based magnetometers and superconducting quantum interference devices.

4.7.1 Meissner-effect flux concentrators

In superconductors, eddy currents induced by a penetrating magnetic flux do not decay over time as would occur in normal conductors. Instead, the field induced by the secondary eddy current permanently remains and expels the original field. This phenomenon is better known as the Meissner effect [103].

Meissner-effect-based flux-to-field concentrators can be applied to enhance the sensitivity of a magnetometer placed close to a superconducting loop [104, 105]. In this design, a narrow cross section is implemented into the superconductive pick-up loop to locally enhance the magnetic field at the vicinity of the magnetometer. This technique has been implemented to enhance the sensitivity of a GMR sensor at 4 K by a factor of 3×10^5 from a value of 30 fT/$\sqrt{\text{Hz}}$, which is typically achievable with standard GMR sensors at room temperature.

4.7.2 Superconducting quantum interference device magnetometers

Magnetometers based on superconducting quantum interference devices (i.e. SQUIDs) utilize the phenomena of flux quantization and Josephson tunneling [60, 62, 76, 106, 107]. The flux quantization criterion is defined such that a magnetic flux through a superconductive loop has to obtain quantized values of a so-called flux quantum. Josephson tunneling occurs in a junction consisting of two superconductors that are separated by a so-called weak link. This weak link can, for example, be a thin insulator or a segment of a superconductor with a narrow cross section.

The effects of Josephson tunneling and flux quantization can be utilized in two different configurations for magnetometry: DC and RF operated SQUIDs (cf. Fig. 4.3). In a DC SQUID, two Josephson junctions on two sides of a loop are first biased with a current source into a state in which a voltage can build up over the junctions but still being below the critical current of superconduction. If an external magnetic field is applied, a secondary current gets induced into the supecrconducting loop to oppose the change in the magnetic flux. This current would expel the applied flux completely if the loop were not interrupted by the two Josephson junctions. Since the loop is superconductive, the total flux through the loop has to obey the flux quantization criterion, which determines the strength of the secondary current, and hence the voltage over the Josephson junctions. In DC SQUIDs, this voltage buildup becomes the measure of the external magnetic flux. The sensor response would otherwise oscillate as a function of applied flux with the period of the flux quantum if one does not use flux-locked-loop electronics to linearize the signal. To raise the signal above the $1/f$ noise region, altering magnetic flux modulation with an external coil can be utilized in a sensor configuration.

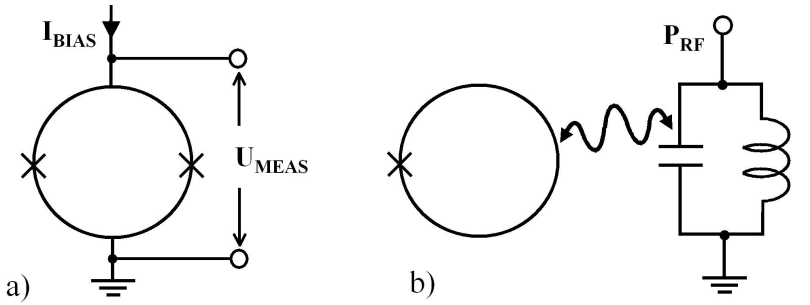

Fig. 4.3. *(a) Two Josephson junctions in a superconductive loop constitute a DC SQUID magnetometer. The voltage over the biased Josephson junctions fluctuates with the period of a flux quantum, giving an accurate measure of the applied magnetic field. (b) In an RF SQUID construct, an LC tank couples to a superconductive loop interrupted by one Josephson junction.*

In an RF-driven SQUID, a superconductive loop with a single Josephson junction is driven through a LC tank circuit via mutual inductance. The applied flux versus total loop flux curve becomes hysteretic with the right design parameters of the loop. The corresponding quantum transitions can be detected as dissipated energy, and thus as a periodic modulation of the quality factor of the LC circuit. If an RF SQUID is operated in a nonhysteretic mode, the level of coupling between the LC tank and the SQUID loop varies periodically by the applied flux through the loop. Consequently, the shift in the level of coupling is observed as a periodic change in the effective inductance of the LC tank, and thus as a shift in the resonance frequency of the tank.

Of all the available magnetometer technologies, a DC-biased SQUID magnetometer provides one of the most accurate ways to measure magnetic fields, and sensitivities below 1 fT/$\sqrt{\text{Hz}}$ have been reported. In comparison to RF SQUIDs, the sensitivities of DC SQUIDs are approximately an order of a magnitude better. DC SQUID magnetometers with a flux-locked-loop detection scheme can operate up to bandwidths of 10 MHz, and the bandwidth can be extended up to the gigahertz range with microwave-operated RF SQUIDs. For nonsensitivity-limited measurements, an accuracy of 0.2 ppm/ $\sqrt{\text{Hz}}$ can be estimated.

In principle, the maximum measurable field strength with SQUIDs is limited by the critical current of the superconductor. Such flux densities can be tens of teslas with modern high-critical-field superconductors and SQUIDs have been manufactured to measure flux densities up to 9 T [107]. The drawback of

SQUIDs is the complexity of the implementation owing to the cryogenic environment required.

4.8 Atomic magnetometers

The Zeeman splitting either of electrons or nuclei is the fundamental basis of atomic magnetometers. In comparison to many other magnetometers, these devices offer very high precision and sensitivity. Atomic magnetometers are, with one exception (i.e., the spin-exchange relaxation-free magnetometer), total field magnetometers. The total field detection provides certain advantages since the magnetometers are less sensitive to orientation errors and noise from mechanical vibrations.

4.8.1 Nuclear magnetic resonance magnetometers

The principles of nuclear magnetic resonance have already been introduced in Chapter 2. For magnetometric applications, a small NMR sample is accompanied with an RF excitation and detection hardware [2, 30, 62, 108, 109]. The resonance effect is monitored as an absorption peak in a so-called continuous-wave scheme, or more accurately in a pulsed mode where a free induction decay curve is monitored after a pulse excitation.

NMR-based magnetometers show high sensitivity down to the range of $\sim$10 pT/$\sqrt{\text{Hz}}$. Above the sensitivity-limited region, high precisions of $\sim$0.01 ppm/$\sqrt{\text{Hz}}$ are also achieved. The drawback of NMR-based magnetometers with Faraday detection is that obtainable signal levels scale as the square of the detected field. This forces to use additional biasing fields at lower field strengths or a substitute method for the Faraday detection, such as SQUID-based magnetometers. With wideband read-out electronics, the measurement bandwidth can be several tens of megahertz. Low-conductivity NMR samples are typically preferred, and the total noise of NMR magnetometers is typically dominated by noise from the pick-up coil and the read-out electronics.

4.8.2 Overhauser magnetometers

In Overhauser magnetometers bulk nuclear magnetization is artificially increased beyond thermal equilibrium to gain stronger NMR signal levels [59, 62, 110]. The scheme exploits the coupling between electron and nuclear polarizations and the fact that electron polarizations close to 100% are achieved in a relatively straightforward manner. In this magnetometer scheme, free radicals are

added to a solution containing NMR signal sources, and the free radicals are radiated with an RF corresponding to the energy difference between the electron and the nuclear spin states. The polarization of the electrons is consequently transferred to nuclei through electron-nucleus cross-relaxation coupling, a phenomenon known as the Overhauser effect.

Dynamic nuclear polarization can increase NMR signal levels by a factor of 100-2 000. A typical application of Overhauser magnetometers is magnetic field measurements in the range of the Earth's field strength, where a normal NMR-based magnetometer has limited signal levels. Another benefit of an Overhauser magnetometer is that continuous measurements with high precision can be performed since excitation and signal reception can be done in parallel because of their different frequency regions. A drawback of the technique is the increased complexity in implementing this detection scheme in comparison to typical NMR magnetometers.

4.8.3 Electron paramagnetic resonance magnetometers

Electron-paramagnetic-resonance-based sensing of magnetic fields is similar to the NMR phenomenon with the exception that the resonance of the orbital electrons is now exploited for the signal detection [59, 108, 109, 110]. Electron paramagnetic resonance (EPR) sensors outperform their NMR counterparts with respect to sensitivity owing to the significantly larger gyromagnetic ratio of electrons. In comparison to hydrogen, whose isotopes have the highest gyromagnetic ratios of all nuclei, the gyromagnetic ratio of electrons is roughly 500 times larger with a value of 28.6 GHz/T.

For signal detection, sensing electronics similar to those of NMR magnetometers are utilized with the distinction that the measurement region can be extended to lower field strengths before the need to utilize a biasing field. A drawback of the magnetometer technique is in making measurements at high fields ($>$500 mT) since the high-frequency electronics required for the operation become more challenging to manufacture.

4.8.4 Optically pumped magnetometers

Optically pumped magnetometers resembles their EPR counterparts since the operation is based on the Zeeman splitting of electron states when placed in an external magnetic field [59, 62, 111, 112, 113, 114]. Two approaches for detecting the Zeeman splitting via optical pumping are discussed here: coherent population trapping and direct optical measurement of the Larmor precession frequency.

In coherent population trapping (CPT), electrons at two hyperfine Zeeman-split energy levels are excited by two laser beams into a common higher energy level. If the laser beams are coherent with respect to each other, the excited electrons interfere destructively at this higher energy level. Subsequently, the rate of photon absorption of the atom system becomes significantly reduced. This phenomena can be optically observed, and the difference in the wavelengths of the two pump beams becomes the measure of the magnetic field.

In direct optical measurement of the electron precession frequency, a population at the higher Zeeman state is first increased with optical pumping. The pumping leads to a state of fewer electrons ready for excitation, and a consequent reduction in photon absorption. If pumped electrons are radiated with a continuous magnetic field that equals the Larmor frequency of the electrons, coherent precession follows. The coherent rotation of spins modulates the absorption of the probe beam at a rate dependent on the phase and amplitude of the resonant RF field. This measurement technique results in very narrow resonance linewidths at the Larmor frequency.

Optically pumped magnetometers offer very high sensitivity, which on a laboratory scale are close to that of DC SQUIDs. Chip-scale magnetometers based on the CPT method ($\sim$1 mm) can measure magnetic fields at 40 pT/$\sqrt{\text{Hz}}$ sensitivity. With the direct optical measurement scheme, the sensitivity can be improved to 6 pT/$\sqrt{\text{Hz}}$. So far only narrow operation bands ($\sim$1 kHz) with optically pumped magnetometers have been reported.

4.8.5 Spin-exchange relaxation-free magnetometers

The equation of motion for magnetization in an external magnetic field was introduced in Chapter 2 (cf. Eq. 2.5). In the absence of an RF field, the quasistatic external magnetic field is solely responsible for the rotation of the magnetization [114, 115]. After optical pumping to increase the electron population at a higher energy state, a coherent rotation of magnetization can be observed if an external magnetic field is applied. The reorientation of the polarization can be subsequently observed as changes in the absorption of a linearly polarized probing beam, aligned perpendicular to the applied field, owing to circular dichroism.

Typically, the decay times of alkali-metal vapor atoms are relatively fast owing to the spin-exchange-induced relaxations. However, the precession rate of the magnetization resulting from the applied field is very slow. The combination of these two dynamic effects makes the measurement scheme typically very inaccurate. It has however been discovered that if the density of an alkali metal vapor is very high and the applied magnetic field is very small, the relaxation occurs via the much weaker and slower spin destruction process. This effect is

exploited in spin-exchange relaxation-free (SERF) magnetometers, and sensitivities approximately 100 times better in comparison to other optically pumped magnetometers are observed.

Above the $1/f$ noise region, which can be up to 100 Hz, sensitivities of 70 fT/$\sqrt{\text{Hz}}$ have been achieved with SERF magnetometers. These sensors can offer a considerable alternative to SQUIDs since the magnetometer technique is easier to miniaturize and requires no complex cooling system. One drawback of the method is that it can only be used for measuring magnetic flux densities below 100 nT.

4.9 Discussion and conclusions

The relevant characteristics of different magnetometer techniques have been summarized in Tab. 4.1. The ultimate comparison of each sensor technique is challenging as the performance characteristics of different sensor elements can vary significantly from application to application. Therefore, it is noted that the values given in Tab. 4.1 are general in nature, and the purpose of the summary is more to give the reader a relative estimate about the capabilities of each magnetometer technique.

To find suitable candidates for magnetic field monitoring in MRI, the characteristics of each magnetometer technique are compared with the requirements derived in Chapter 3. Based on the requirement for MRI compatibility of the second kind, all magnetometer concepts containing ferromagnetic materials–hence flux-gate, magnetostrictive, and magnetoresistive sensors apart from EMR–are eliminated.

EMR magnetometers, as with other Hall-effect-based devices, can be optimized for high field strengths. Benefits of these sensors include the simplicity of the detection scheme and the economical manufacture of sensing elements by semiconductor processes. InSb Hall plates and EMR sensors can potentially offer high enough precision for certain specific MRI applications as long as $1/f$ noise is kept constrained. Since the scope of this thesis is to develop a general magnetic field monitoring system for MRI that holds its functionality regardless of an applied MRI sequence or application, the Hall-effect-based techniques are considered not to have enough potential for further studies.

Optical and MEMS-based magnetometers can also be tailored for high-field operations. However, this tailoring occurs at the expense of sensitivity for lower field changes, and these techniques are therefore not considered to be precise enough for applications in the context of this thesis.

The functionality of SQUIDs has been proven at magnetic flux densities above 1 T as well, but the high critical field for superconduction requires a bulky coolant system. This fact, in addition to the most likely method not having the required dynamic range, reduces the chances of SQUIDs being feasibly implemented for magnetic field monitoring in MRI.

Optically pumped magnetometers have the high precision required, but the functionality at high fields and with high dynamic range has not been sufficiently proven. In addition, the complexity of the detection schemes makes the technology less desirable.

Pick-up coils offer a simple and economically feasible detection scheme with a proven high precision also at high field strengths. Since temporal gradiometric measurements are considered more viable in the context of real-time magnetic field monitoring, the lack of static field measurement with pick-up coils is not considered to be a major drawback. However, with long MRI acquisition times, which can be up to 100 ms, one should carefully address the $1/f$ noise issues that generally impede the performance of pick-up coils.

Of the existing atomic magnetometers, NMR probes are an intuitive solution for magnetic field monitoring in MRI since the sensing concept is based on the same physical principle as MRI itself. As the effect of EPR probes resembles the NMR phenomenon, the same conclusion can also be made for this magnetometer technique. The EPR and NMR magnetometers are total field sensors, and therefore they are less influenced by errors from sensor disorientation or mechanical vibrations. Although EPR probes, including Overhauser effect sensors, also offer better sensitivity over NMR ones, the required millimeter-wave electronics for tesla-range operations makes the concept economically less attractive. However, RF components for NMR detection at 10-500 MHz are inexpensive and available from various commercial vendors. Therefore it seems encouraging to proceed further with the NMR-based technique for magnetic field monitoring in MRI.

Despite the large variety of available magnetometers, only very few technologies have been estimated to meet the demanding requirements for magnetic field monitoring in MRI. Pick-up coils can potentially fulfill the performance requirements, and these are chosen for further study owing to the simplicity and the cost effectiveness of the technique. Although NMR probes are more complex to implement, the proven high precision in the absence of $1/f$ noise indicates that NMR probes can best fulfill the desired performance requirements for precision and dynamic range.

Magnetometer	B_{min} [T/$\sqrt{\text{Hz}}$]	B_{max} [T]	ΔB [ppm/$\sqrt{\text{Hz}}$]	BW [Hz]	$f_{1/f}$ [Hz]
SQUID (at 4 K)	1 f	10	0.2	1 G	10
Pick-up coils	20 f	>10	1	1 G	10-1 000
SERF	70 f	100 n	1 000	100 k	–
Optically pumped	100 f	100 μ	<0.01	100 k	–
Electron precession	500 f	100 m	<0.01	1 G	–
MEMS (tunneling)	2 p	10 m	200	10 k	100
Nuclear precession	10 p	>10	0.01	100 M	–
Magnetostriction (magnetoelectric)	10 p	10 m	100	50 k	–
EMR	10 p	>10	10	1 G	10
Flux-gate	30 p	10 m	50	10 k	–
AMR,	100 p	5 m	100	100 M	10
GMI	100 p	100 μ	50	10 M	–
GMR	100 p	100 m	100	1 G	1-100 k
MTJ	100 p	10 m	200	1 G	10 k
MEMS (Lorentz force)	1 n	10 m	100	1 G	100
Magneto-optical	1 n	>10	1 000	10 M	–
BJT magnetotransistor	10 n	1	100	1 M	10
Hall plate	100 n	1	10	1 M	10 k
Magnetodiode	100 n	1	100	1 M	1 k
MAGFET	1 μ	1	100	1 M	1 k

Table 4.1. *Summary of magnetometer techniques with corresponding performance characteristics. Here, B_{min} stands for a measurement sensitivity, B_{max} for a maximum operating magnetic flux density, ΔB for a precision, BW for the maximum bandwidth, and $f_{1/f}$ for the $1/f$ noise knee frequency.*

5

Inductive Pick-up Coils for Monitoring Magnetic Field Gradients in MRI

Detecting inductively the time-varying magnetic fields of MRI potentially offers a simpler and more cost-effective approach in comparison to NMR-based magnetometers. The inductive pick-up coils were briefly introduced in Chapter 4. This chapter delves into further theoretical details, which are relevant for the performance analysis later in the text. The profound work of Senaj et al. [31] forms the basis for the treatment with some required additions. The limitations of the technique are described, and the outcome is discussed with respect to the performance characteristics required from a magnetometer system for real-time magnetic field monitoring in MRI. A presentation of the results from a practical implementation concludes the chapter.

5.1 Principles of pick-up coil gradiometers

Based on Faraday's law of induction, i.e., Eq. 2.11, a changing magnetic field induces a voltage over a coil. If two identical but counterwound coils are placed $|\mathbf{r}|$ apart and connected in series, the induced differential voltage $U_{in}(t)$ becomes the measure of the gradient of the magnetic flux density between the coils, $G(t)$. From Eq. 2.11, it can be shown that

$$G(t) = -\frac{1}{AN|\mathbf{r}|}\int_0^t U_{in}(\tau)d\tau, \tag{5.1}$$

where A is the cross-sectional area of a coil, N is the number of turns, and t is the measurement time. After resolving the three-dimensional gradient profiles, one can subsequently resolve the temporal k-space locations from Eq. 2.15.

An electrical circuit for an analog integration is illustrated in Fig. 5.1 [31, 65]. It can be shown that the measured signal at the output of the integrator

becomes

$$U_{out}(t) = -\frac{1}{R_i C_i}\int_0^t U_{in}(\tau)d\tau, \tag{5.2}$$

where R_i and C_i are the resistor and the capacitor, respectively, in the schematic in Fig. 5.1. One gets from Eqs. 5.1 and 5.2 that

$$G(t) = \frac{R_i C_i}{AN|\mathbf{r}|}U_{out}(t). \tag{5.3}$$

In a digital integration scheme, the differential input signal of the coil pair is directly sampled by an analog-to-digital converter (ADC), and a digital or a software-based integration algorithm for the data is applied subsequently. In the following section, the capabilities of both of these methods are theoretically studied.

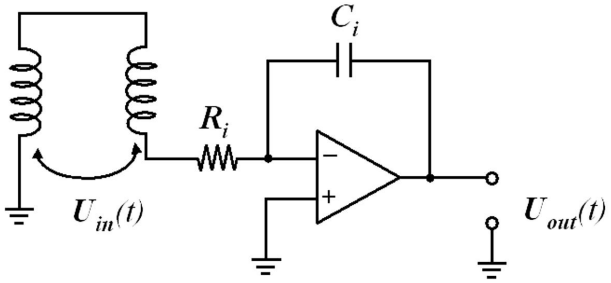

Fig. 5.1. *After an analog integration, the differential voltage induced into two counterorientated coils becomes the measure for the temporal magnetic field gradient between these two coils.*

5.2 Analog integration

To investigate the noise characteristics of an analog integrator, the ideal integrator scheme shown in Fig. 5.1 is modified by introducing the relevant noise sources, as is illustrated in Fig. 5.2. In practice, the analog integrator scheme should not be too sensitive to suppress the influence of the integrator-related noise errors. Thus, the product of R_i and C_i should be kept large enough, as is seen from Eq. 5.2.

In Section 3, it was derived that a gradiometric drift $\Delta G = 4.3$ nT/m (i.e., $\Delta B = 1.7$ nT at FOV = 40 cm long probe displacement) is acceptable at monitoring periods of 100 ms. On average, this relates to a relative integrator output error of

$$\Delta u_{err} = \frac{\Delta G}{G_{max}}, \tag{5.4}$$

which is 0.1 ppm at the maximum gradient strength, G_{max}, of 40 mT/m.

Error related to the input bias current I_{bias} limits the smallest value for the integrative capacitor C_i [31], and

$$C_i \geq \frac{I_{bias} t}{U_{outMax} \Delta u_{err}}, \tag{5.5}$$

where U_{outMax} is the maximum output voltage and Δu_{err} is the acceptable level of the relative measurement error (a unitless quantity).

A chopper-stabilized, high-precision operational amplifier, such as TLC2656A (Texas Instruments, Dallas, TX), is a good reference for performance characteristics that are achievable with present-day operational amplifiers. For TLC2656, $I_{bias} \approx 4$ pA, and $U_{outMax} = \pm 5$ V is obtained from the manufacturer.

From the error related to the input offset voltage U_{off} at the integrator output, one gets a constraint for the value of R_i [31]:

$$R_i \geq \frac{U_{off} t}{U_{outMax} \Delta u_{err} C_i}. \tag{5.6}$$

Here, $U_{off} \approx 0.5$ μV for a TLC2656, which can be reduced to $\sim$5 nV by utilizing an input offset compensation circuit [31]. For the Johnson noise of a lossy electrical component R, one gets that

$$u_n = \sqrt{4 k_B T R \mathrm{BW}}, \tag{5.7}$$

where k_B is Boltzmann's constant, T is the temperature, and BW is the measurement bandwidth. The error related to the Johnson noise of R_i is limiting itself, and

$$R_i \geq 4 k_B T \mathrm{BW} \left(\frac{t}{U_{outMax} \Delta u_{err} C_i} \right)^2. \tag{5.8}$$

With the given characteristics of TLC2656, one concludes from Eq. 5.5 that $C_i \geq 0.8$ μF (with monitoring periods of 100 ms). Typically, R_i is limited more by U_{off} than by Johnson noise, and one gets by combining Eqs. 5.5 and 5.6 that the minimum RC time constant of the integrator becomes

$$\tau_{RC} = \frac{U_{off} t}{U_{outMax} \Delta u_{err}}. \tag{5.9}$$

Thus $\tau_{RC} \geq 10$ ms, which clearly would not fulfill the 25-kHz monitoring bandwidth requirement (cf. Chapter 3). Thus, one can conclude that, with the given $1/f$ noise and bandwidth requirements, utilizing the analog integration scheme for the pick-up-coil-based gradient field detection method would not be the most optimal method.

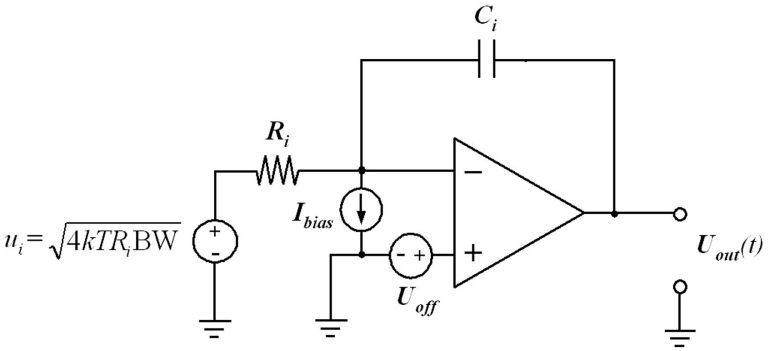

Fig. 5.2. *An ideal operational amplifier is supplemented with external noise sources to simulate the effect of the input offset voltage U_{off} and input bias current I_{bias}. In addition, the Johnson noise u_i of the input resistor is included in the noise analysis.*

5.3 Digital integration

A digital integration scheme is advantageous over an analog one because it is immune to operational-amplifier-related imperfections such as input offset voltages and input bias currents. In addition, the resistance R_i is omitted, thereby reducing the overall Johnson noise in the signal.

For a digital integrator, the expected dynamic range of the detected signal is solved to derive the number of bits required from an ADC. For the lowest measurable signal, it can be shown that [31]

$$U_{inMin} = -AN\,|\mathbf{r}|\left(\frac{\Delta G}{t}\right), \tag{5.10}$$

where ΔG is 4.3 nT/m at 10 Hz, as has been derived in Chapter 3 (i.e., $\Delta B = 1.7$ nT at a probe displacement of 40 cm FOV). For the maximum signal, one gets that

$$U_{inMax} = -AN|\mathbf{r}|\left(\frac{G_{max}}{t_{rise}}\right), \tag{5.11}$$

where G_{max}/t_{rise} is the slew rate of an MRI scanner, typically on the order of 150 T/m/s. The estimated dynamic range is given as the ratio of the maximum and minimum signal values (140 dB). This result reflects an ADC with a resolution of approximately 24 bits and corresponds to the upper limit of typically available ADCs on the market. However, the effective bit rate of such devices, especially at the required bandwidth of 50 kHz, falls well below these requirements. For example, AD1556, a 24-bit ADC from Analog Devices, has a maximum sampling rate of 16 kHz, at which its dynamic range is only 40 dB.

5.4 Application to magnetic field monitoring

A two-dimensional pick-up-coil-based gradiometer has been manufactured for verifying the theoretical considerations. Two counterwound coils of 640 turns and 9-mm average diameter are placed 15 cm apart (cf. Fig. 5.3a). To avoid erroneous signal coupling during gradient switching via the coil leads, coaxial cables are utilized to connect the coils to the read-out electronics.

An analog integration scheme is chosen, and it is based on a TLC2656A operational amplifier as is shown in Fig. 5.3b. Here, the integrator capacitor is discharged between each measurement with a relay, and the error related to the input offset voltage is reduced by approximately two orders of a magnitude with offset compensation circuitry [31]. A differential output is provided to increase common-mode rejection.

The integrator R_iC_i time constant is set to 1/(22 kHz). A 14-bit analog-to-digital converter is utilized after the integration, thus offering a dynamic range of 84 dB. The requirement of 0.3 ppm/$\sqrt{\text{Hz}}$ for the dynamic range of field monitoring (cf. Tab. 3.2) relates to a value of 87 dB for gradient measurements in the absence of the $1/f$ noise, at 22-kHz measurement bandwidths (Eq. 5.4). Thus, the dynamic range of the ADC is estimated to be sufficient.

The developed pick-up coils show good noise characteristics of 6.3 nT/$\sqrt{\text{Hz}}$ beyond the $1/f$ noise regime, thus being close to the precision requirement of 3 nT/$\sqrt{\text{Hz}}$. However, the $1/f$ noise characteristics are observed to be, as expected, roughly six orders of magnitude above the required 2 pT at 10 Hz. The consequence of the drift can be observed in the measured two-axis spiral trajectory (slew rate = 150 T/m/s and G_{max} = 8.75 mT/m), as is shown in Fig. 5.4. Although, the gradients can be in principle be tracked with the required precision, the $1/f$ noise in the sensors causes random walk in the k-space trajectories to such an extent that the reconstructed images become unusable.

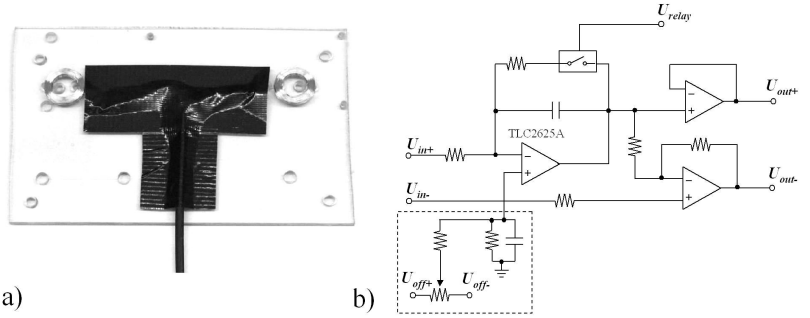

Fig. 5.3. *(a) Two counterwound coils are placed 15 cm apart to measure gradients in the direction of one of the MRI gradient axes. Induced signals in the coils are integrated analogically as is shown in (b). Here, the circuitry for the input offset voltage compensation is highlighted with a dashed box with dedicated control voltages U_{off+} and U_{off-}. The voltage U_{relay} controls the capacitor-discharging relay.*

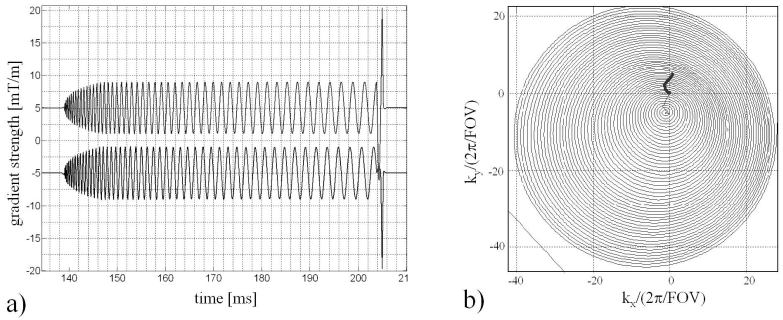

Fig. 5.4. *Two-dimensional gradient profiles are measured during a single-shot spiral scan (a). The unacceptable level of $1/f$ noise in the measured data is seen as asymmetry in the spiral trajectory and as a drift of the center point (b).*

5.5 Discussion and conclusions

The requirement of 4.3 nT/m for gradient drift at 10 Hz is shown to be too demanding for pick-up coils. Theoretical calculations and practical experiments show that the analog integration scheme suffers from $1/f$ noise to such an extent that the scheme cannot fulfill the precision requirements at the desired bandwidths and the maximum length of MRI acquisition periods. The noise characteristics of the coil pair and the integrator could be improved by operating these

at cryogenic temperatures. This however would not be in line with the desired requirement that the system should be simple, robust, and economically feasible.

By performing the integration digitally, one resolves some noise issues that plague the analog integrators. This however does not change the fact that MRI is very sensitive to $1/f$ noise and that integration-based detections have fundamentally high $1/f$ noise characteristics. Therefore, the digital integrator should perform at a very high dynamic range, equaling the effective bit rate of 24. This range is beyond the capabilities of present commercial ADCs when combined with the sampling rate requirement of 50 kHz.

It is therefore concluded that the utilization of inductive pick-up coils for real-time monitoring of gradient fields in MRI is not feasible. The achievable level of precision at low frequencies with this technique does not meet the requirements set by modern MRI sequences. One could find specialized pulse sequences that are insensitive to B_0 drifts and with short acquisition windows to relax the performance requirements. One such example would be to monitor just the velocity-encoding lobes in phase-contrast imaging. As the scope of this thesis is to develop a universal magnetometer system applicable for all MRI applications, no further work within the field of pick-up coils will be done in the context of this thesis.

6

NMR Probes for Magnetic Field Monitoring in MRI

NMR-probe-based magnetic field sensing for improved MRI image quality is introduced in this chapter. In comparison to continuous-wave-based monitoring of NMR signals, higher precision and better temporal resolution are achieved if NMR probes are operated in a pulsed mode. This means that after a short RF excitation pulse, NMR signals from relaxing spins are detected [2, 30, 108]. This chapter introduces the details of pulsed NMR signal detection and its application to general magnetometry, especially for magnetic field monitoring in MRI. Different approaches to operate pulsed NMR probes in an MRI environment are described, as well as the required probe electronics and decoupling strategies to standard MRI acquisitions.

6.1 Principles of NMR-probe-based magnetic field monitoring

A constrained NMR sample (e.g., a water droplet), along with detector RF electronics, constitutes the fundamentals of pulse-operated NMR probes. The Larmor relation gives the relation between the signal phase of an NMR sample and applied magnetic flux density; thus,

$$\frac{d\varphi}{dt} = \gamma B(\mathbf{r},t). \tag{6.1}$$

One sees here that the signal phase measures the time integral of the spatiotemporal magnetic field. If a Taylor expansion is applied to the monitored flux density and only the effects of the spatially constant term (i.e., temporal main magnetic flux density inhomogeneity $\Delta B_0(t)$) and the first-order terms (i.e., the linear flux density gradients $\mathbf{G}(t)$) are studied, Eq. 6.1 can be rewritten to

$$\varphi(\mathbf{r}_n,t) = \varphi_{0,n} + \gamma \int_0^t (\mathbf{G}(\tau)\cdot\mathbf{r}_n + \Delta B_0(\mathbf{r}))\, d\tau. \tag{6.2}$$

Here, $\mathbf{r}_n$ is the location of the nth probe in real space, and φ_0 is the phase offset in the nth probe signal. A three-dimensional magnetic field monitoring experiment requires four NMR probes for solving four unknowns, i.e., the spatially constant term and the three-dimensional k-space location. Thus, the matrix formulation of monitored k-space trajectories becomes

$$\begin{bmatrix} \gamma\int_0^t \Delta B_0(\tau)d\tau \\ k_x(t) \\ k_y(t) \\ k_z(t) \end{bmatrix} = \begin{bmatrix} 1 & x_1 & y_1 & z_1 \\ 1 & x_2 & y_2 & z_2 \\ 1 & x_3 & y_3 & z_3 \\ 1 & x_4 & y_4 & z_4 \end{bmatrix}^{-1} \cdot \left(\begin{bmatrix} \varphi_1(\mathbf{r}_1,t) \\ \varphi_2(\mathbf{r}_2,t) \\ \varphi_3(\mathbf{r}_3,t) \\ \varphi_4(\mathbf{r}_4,t) \end{bmatrix} - \begin{bmatrix} \varphi_{0,1} \\ \varphi_{0,2} \\ \varphi_{0,3} \\ \varphi_{0,4} \end{bmatrix} \right). \tag{6.3}$$

With more NMR probes, the higher order terms of the k-space trajectories can be solved, and Eq. 6.2 can be rewritten as [36]

$$\varphi(\mathbf{r},t) = \varphi_0 + \sum_{l=1}^{N_l-1} k_l(t) f_l(\mathbf{r}) + \int_0^t \gamma \Delta B_0(\tau) d\tau, \tag{6.4}$$

where N_l is the number of orthogonal spatial basis functions, which are denoted as f_l.

The offset phases and the spatial locations of the probes are calibrated before extracting the magnetic field data from the probe signals. The calibration is done in analogy to tracking localizations [116]. In this scheme, a short, $\sim$10 ms, pulse sequence is applied where a FID signal is followed by turning on each gradient direction successively (cf. Fig. 6.1). Here, the gradient amplitudes and ramping are set modestly, $\leq$1% from the maximum, to avoid any distortions from eddy currents. The offset and the spatial location term of an individual probe are subsequently solved from Eq. 6.2.

The temporally constant, spatially varying three-dimensional field gradient, ΔG_0, can be solved with four NMR probes as long as the intrinsic chemical shifts of each probe are calibrated in a known background field. Thus, one gets from 6.3 that

$$\begin{bmatrix} B_0 \\ \Delta G_{0,x} \\ \Delta G_{0,y} \\ \Delta G_{0,z} \end{bmatrix} = \begin{bmatrix} 1 & x_1 & y_1 & z_1 \\ 1 & x_2 & y_2 & z_2 \\ 1 & x_3 & y_3 & z_3 \\ 1 & x_4 & y_4 & z_4 \end{bmatrix}^{-1} \cdot \begin{bmatrix} (\varphi_1(\mathbf{r}_1,t) - \varphi_{0,1})\gamma_1^{-1} \\ (\varphi_2(\mathbf{r}_2,t) - \varphi_{0,2})\gamma_2^{-1} \\ (\varphi_3(\mathbf{r}_3,t) - \varphi_{0,3})\gamma_3^{-1} \\ (\varphi_4(\mathbf{r}_4,t) - \varphi_{0,4})\gamma_4^{-1} \end{bmatrix} t^{-1}. \tag{6.5}$$

A phase-unwrapping algorithm is applied to remove 2π phase jumps in the monitored signal phases. A failure in this algorithm is the determining factor of

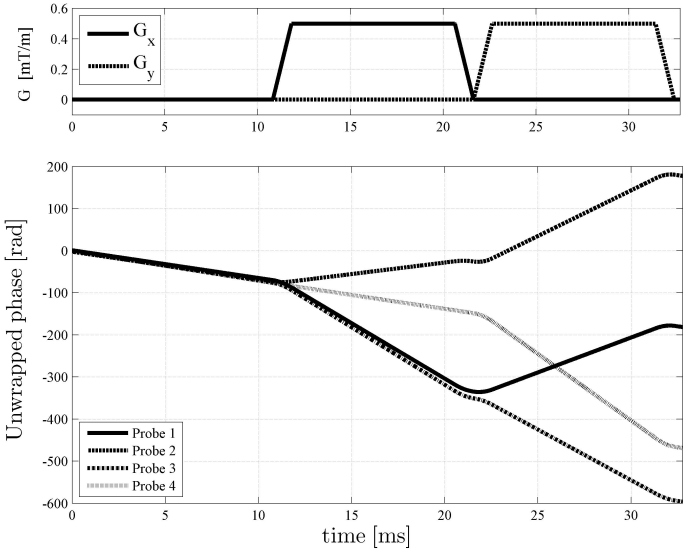

Fig. 6.1. *An illustration of a calibration scan to locate four NMR probes in a two-dimensional plane, as well as to solve the intrinsic phase offsets of the probes. The top figure indicates the temporal gradient performance, and the bottom one the signal phases of four NMR probes.*

how long k-space trajectories can be tracked for, and a criterion can be formulated that

$$\left| \frac{\gamma \mathbf{G} \cdot \mathbf{r}_n}{f_m} \right|_{\max} < \pi, \tag{6.6}$$

where f_m is the monitoring frequency. Thus, the likelihood of a failure increases at stronger gradient fields. If the monitoring frequency is limited, one can exploit nuclei with lower gyromagnetic ratio for higher applicable gradient strengths or wider probe displacements, respectively. In contrast, longer distances between probes transform to relaxed precision requirements, as is shown by Eq. 3.4.

6.2 Parallel operation of NMR probes with MRI

6.2.1 Standard, long-interval excitations-based operation scheme

Exciting the spin ensemble of an NMR probe and measuring the following free induction decay curve once per each imaging repetition resembles the basic operation of MRI. This operating scheme is hereafter referred to as standard, long-interval excitations-based magnetic field monitoring. If NMR samples are based on the same nuclei as imaged objects, which are typically ^{1}H, the existing MRI transmit-receive RF hardware can be utilized also for operating the NMR probes. No additional RF excitation hardware is needed as long as the NMR probes are placed inside the excitation plane of the imaged objects. Modern clinical MRI scanners can be equipped with receiver systems for up to 128 channels [117] and connecting ^{1}H NMR probes in parallel to imaging coils in such a receiver system is also a straightforward process. As the receiver channels are already optimized for accurate signal detection with high dynamic range, no hardware changes are required.

Although using receive-only ^{1}H NMR probes and relying on system excitations offers one the simplest ways to implement NMR probes for magnetic field monitoring in MRI, the implementation has certain drawbacks. Typically only suboptimal, i.e., non-90°-flip-angle, excitations are delivered for the NMR probes since excitation profiles are optimized for imaging purposes. This issue can be tackled to some extent if specially made pulse designs, which compromise between imaging and magnetic field monitoring, are designed. Another drawback of the implementation is the unwanted signal coupling between imaging and monitoring since the monitoring and imaging systems would operate within the same frequency band.

To move toward a more independent monitoring system that does not require specially made pulse sequences, separate MR transmit-receiver hardware is needed. Such hardware ensures optimal spin excitation independent of applied pulse sequences, does not occupy relatively expensive receiver channels in an MRI system, and allows the use of non-proton-based NMR probes. One of the most important reasons for using non-proton-based NMR probes is that it practically eliminates signal coupling between ^{1}H imaging. This topic of signal decoupling will be further discussed later in this chapter.

In standard, long-interval excitations-based magnetic field monitoring, the amplitude of the FID signal should remain high throughout the active gradient section of each repetition. In certain single-shot image acquisitions, the acquisition length can last as long as 100 ms. Consequently, the T2 transverse relaxation time of an NMR probe should be at or preferably above this value.

Local magnetic field inhomogeneities over the NMR sample can severely shorten read-out times from the intrinsic limit of T2 decay (cf. Eq. 2.9). Differences in the magnetic susceptibility of the materials used in NMR probe constructs should therefore be kept small. Achieving this can be challenging since T2* values above 100 ms can relate to values below 100 ppb for the acceptable levels of average field variation over the sample volume [56, 118]. The requirement for field homogeneity can be relaxed to some extent by using non-proton-based NMR probes of lower gyromagnetic ratio, as can be seen from Eq. 6.1. This topic of minimizing sample B_0 field inhomogeneity is further discussed in Chapter 8.

In addition to static field inhomogeneities, gradient-induced signal dephasing over the probe sample can also lead to undesirably low signal levels. This effect forces one to restrict the probes to small sample sizes. If Δl is the sample dimension in the direction of an applied gradient envelope, and it is assumed that the sample cross section perpendicular to this direction remains constant, as it is along the axial direction of a cylindrical sample, one can derive from Eq. 6.2 by calculating the volume integral of the NMR signal over the complete sample volume that [119]

$$U_{signal}(\mathbf{k},\mathbf{r}) = U_0 e^{i\mathbf{k}\cdot\mathbf{r}} \mathrm{sinc}(|\mathbf{k}|\,\Delta l/2), \tag{6.7}$$

where $\mathbf{r}$ indicates the center of the sample and U_0 is the intrinsic signal level in the absence of gradient activity. If the same type of NMR nucleus is utilized in imaging and in NMR probes, it is seen from Eqs. 2.16 and 6.7 that NMR sample sizes are constrained to dimensions of less than twice the imaging resolution, Δx; thus, $\Delta l < 2\pi/k_{\max} = 2\Delta x$. In high-resolution imaging, the criterion leads to smaller sample sizes and lowered signal amplitudes, as well as to manufacturing challenges in miniaturizing the NMR probe design. Nuclei with smaller γ are less shifted in k space by the image-encoding gradients (cf. Eq. 2.15), and for their benefit larger sample sizes or higher resolutions become possible.

Undesired loss in a signal level is also observed with imaging sequences where the repetition rate TR is less than the T1 longitudinal relaxation time of the NMR sample. In such cases, longitudinal magnetization does not have enough time to recover. If perfect spoiling of transverse magnetization at the end of each repetition is assumed, the system converges toward a steady state, and one can write for the longitudinal magnetization [120]

$$M_z = M_0 \left(\frac{1 - e^{-\mathrm{TR/T1}}}{1 - \cos(\theta)\, e^{-\mathrm{TR/T1}}} \right), \tag{6.8}$$

where θ stands for the applied flip angle. In contrast, the transverse magnetization becomes

$$M_{xy} = M_z \sin(\theta) e^{-\mathrm{TR}/\mathrm{T2}*}. \tag{6.9}$$

By applying the so-called Ernst angle, θ_e, one maximizes the signal level at a given TR/T1 ratio. From Eqs. 6.8 and 6.9, one gets that

$$\theta_e = \arccos\left(e^{-\mathrm{TR}/\mathrm{T1}}\right). \tag{6.10}$$

It is noted from Eqs. 6.9 and 6.10 that achievable signal amplitudes converge toward zero at repetition rates significantly shorter than the T1 relaxation time constant.

To make standard, long-interval excitations-based magnetic field monitoring effective for the largest possible range of TR values, the T1 time of the NMR sample should be kept as short as possible. Since T1 is always greater than T2, the value of T1 is limited by the minimum affordable value for T2. However, T2, or effectively T2*, is limited by the longest applied monitoring window, and hence it is $\sim$100 ms.

Dissolved paramagnetic salts (e.g., $CuSO_4$ or $GdCl_3$) can be utilized to adjust the T1 and T2 relaxation times of water-based samples. The relations between paramagnetic salt concentration in water and the corresponding T1 and T2 values are given as [53]

$$\frac{1}{\mathrm{T1}} = \frac{1}{\mathrm{T1}_0} + \frac{N_d}{c1} \tag{6.11}$$

and

$$\frac{1}{\mathrm{T2}} = \frac{1}{\mathrm{T2}_0} + \frac{N_d}{c2}, \tag{6.12}$$

where $\mathrm{T1}_0 = 3.56$ s and $\mathrm{T2}_0 = 2.20$ s are undoped relaxation times, N_d is the number of dopant molecules in the solution, and $c1$ and $c2$ are constants. For example, for $CuSO_4$ $c1 = 8.67 \times 10^{23}$ s/m^3 and $c2 = 8.07 \times 10^{23}$ s/m^3, respectively. Here it should be noted that the T1/T2 ratio converges toward $c1/c2$ = 1.07 at high $CuSO_4$ concentrations, which is close to the desired state of T1 = T2.

In practice, perfect RF spoiling is difficult to achieve and some residual transverse magnetization typically exists after each repetition. Since the phase of the residual transverse magnetization before each consecutive RF excitation is not determined beforehand, achieved signal levels distribute randomly around the steady-state value. The worst case occurs when a succeeding RF pulse flips the transverse magnetization back to zero. To counter such an effect of destructive interference in transverse magnetization, special hardware to phase-lock the precessing spins and the excitation pulses is required.

6.2.2 Coherent, short-interval excitations-based operation scheme

The shortcomings of the standard, long-interval excitations-based operation scheme can be avoided with a more advanced method to operate NMR probes. By reducing the sample T1 and T2 times with proper sample doping, one optimizes the probe operation for short TR acquisitions (cf. Eq. 6.8). To ensure that transverse magnetization does not decay to too low values even during the longest read-out windows, typically at 100 ms per repetition, the probes can be excited in a repetitive manner. To ensure quasicontinuous monitoring data, the excitation periods should be kept short (i.e., $<1/f_m$).

The phase evolution of the spin ensemble cannot be determined beforehand, and the excitation pulses will have a random phase difference to precessing transverse magnetization if no special attention for phase coherency is given. In the worst case, destructive interference in the total transverse magnetization may occur if newly excited spins have an opposite phase to the already exited spins. The significance of phase-coherent excitation pulses to ensure high signal levels is further illustrated with simulation results shown in Fig. 6.2. This advanced scheme of operating NMR probes is hereafter referred to as coherent, short-interval excitations-based field monitoring.

Operating NMR probes with the coherent, short-interval excitations-based scheme offers certain further benefits over the standard, long-interval excitations-based monitoring. The sample T2 value can be significantly reduced, which leads to relaxed sensitivity to local field inhomogeneities, i.e., T2* $\approx$ T2. This simplifies the probe manufacturing process, as well as improves integration to imaging coils, patient tables, stereotactic frames, and magnetic bores. In addition, probe placement becomes possible in the outer regions of the MRI bore where the background magnetic field is intrinsically less homogeneous. Because of the high frequency of excitations, the probe sample sizes become less restricted by gradient-induced dephasing. This characteristic can be exploited by using stronger gradients or larger samples for higher signal levels. To ensure that the repetition rate, TR_{probe}, is high enough to counter the gradient-induced dephasing, a criterion can be derived from Eq. 6.7 that

$$\gamma G_{\max} \Delta r \mathrm{TR}_{probe} < \pi. \tag{6.13}$$

For example, at $\Delta r = 2$ mm and $G_{\max} = 40$ mT/m, Eq. 6.13 gives TR_{probe} = 150 μs.

In the standard, long-interval excitations-based monitoring scheme, a single exciter is sufficient for exciting all the probes regardless of whether a volume RF coil is utilized, or the transmission signal is split to locally excite all the spin ensembles in each transmit-receive NMR probe. With the coherent, short-interval

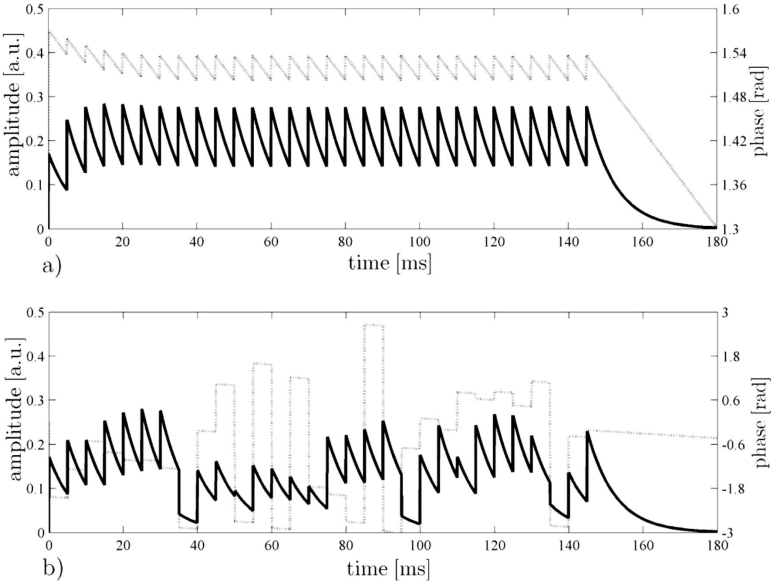

Fig. 6.2. *Transverse magnetization with an NMR probe based on the coherent, short-interval excitations scheme. Here, the amplitude of the magnetization is plotted with a solid line, and the phase with a dashed line. If RF pulses are (a) in phase with precessing spins, a steady state of magnetization emerges instead of (b) a pseudo-random one. The parameters of T1 = 8 ms, T2 = 9 ms, and TR = 5 ms were applied in these simulations.*

excitations-based monitoring scheme, each probe requires its own exciter as the phase evolution is unique to each probe location. The design of such exciters will be further studied in Chapter 7.

Utilizing the coherent, short-interval excitations-based operating scheme for NMR probes significantly tightens the decoupling requirement with standard MR imaging. This is because the transmission pulses are now also applied during the image-acquisition phase and because the transmission pulses must have amplitudes that are several orders of magnitude larger than those of the NMR signals.

6.3 NMR probe electronics

In this section, the electronics required for NMR signal detection are described, as well as the factors contributing to the total signal-to-noise ratio of an NMR

probe. It is shown that only little modification is required in the probe electronics if the probes are operated in transmit-receive fashion instead of the simpler design of receive-only probes, which rely on system excitations. For transmit-receive probes, some additional adjustments are required if the probes are operated with the coherent, short-interval excitations-based method in comparison to the standard, long-interval excitations-based operation scheme.

6.3.1 Signal-to-noise ratio and electronics for receiving NMR signals

At the Larmor frequencies of typical clinical MRI background field strengths, pick-up coils outperform other magnetometers for detecting the relaxing transverse magnetization of NMR samples. To derive the equation for the received signal amplitude U_{probe}, Eqs. 2.11, 2.17, and 6.2 are combined, giving

$$U_{probe}(\mathbf{r},t) = \omega \int_V \Psi_-(\mathbf{r}) M_{x,y}(\mathbf{r},t) e^{i\varphi(\mathbf{r},t)} d\mathbf{r}, \tag{6.14}$$

where V stands for an NMR sample volume and Ψ_- is the receiver coil sensitivity.

The SNR of an NMR probe determines how accurately the phase information can be extracted from the NMR signal. For SNR analysis, an NMR probe can be modeled with a Thevenin source, as is shown in Fig. 6.3. If electromagnetic interference to the probe is assumed to be negligible, the Johnson noise arising from the lossy components of the probe, R_{probe}, is the sole contributor to the noise in SNR calculations. By applying Eqs. 2.3, 5.7, and 6.14, one gets [41, 121]

$$\mathrm{SNR} = \frac{U_{probe}}{U_{noise}} = \frac{\Psi_- V n \gamma J(J+1)\hbar^2\omega^2}{3k_b T\sqrt{4k_b T R_{probe}\mathrm{BW}}}, \tag{6.15}$$

where $\hbar$ is Planck's contant divided by 2π, J is the spin quantum number, T is the temperature, k_b is Boltzmann's constant, and BW is the measurement bandwidth. Here, one assumes a 90° excitation pulse, a constant signal phase over the sample, and a homogeneous NMR sample volume and receiver profile.

Sensing electronics ensure effective signal coupling from RF coils to NMR receivers. The total system noise figure, NF_{tot}, can be expressed as a ratio of input and output SNRs:

$$\mathrm{NF}_{tot} = \frac{\mathrm{SNR}^2_{input}}{\mathrm{SNR}^2_{output}}. \tag{6.16}$$

The Friis formula illustrates the influence of each system component on the total system noise figure, NF_{tot}:

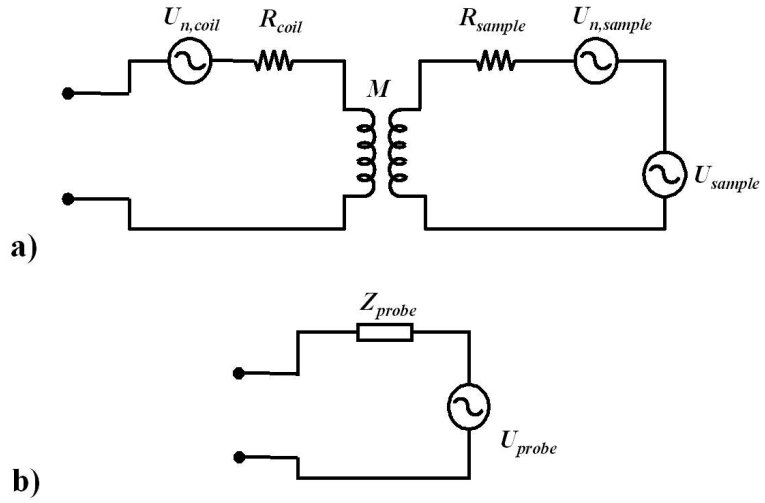

Fig. 6.3. *(a) Equivalent electrical circuit for modeling signal coupling from an NMR sample, U_{sample}, to an RF probe via mutual inductance,M. The sample and the coil losses, i.e., R_{sample} and R_{coil}, with equivalent noise sources $U_{n,sample}$ and $U_{n,coil}$ are included. (b) The circuitry can be simplified to a Thevenin source with an output impedance $Z_{probe}(\omega) = R_{probe}(\omega) + jX_{probe}(\omega)$.*

$$\mathrm{NF}_{tot} = \mathrm{NF}_1 + \frac{\mathrm{NF}_2 - 1}{G_1} + \frac{\mathrm{NF}_3 - 1}{G_1 G_2} + \cdots + \frac{\mathrm{NF}_n - 1}{G_1 G_2 \cdots G_{n-1}}. \tag{6.17}$$

Here, the receiver chain has been divided into n components with corresponding noise figures NF_n and gains G_n. From Eq. 6.17, one notes that the total system noise figure is dominated by the noise figure of the preamplifier, and the noise from the subsequent components is suppressed by the gain of the preamplifier. Thus, it is desired to place a low-noise preamplifier as close to the NMR probe as possible.

Figure 6.4 shows an NMR probe with an adjacent low-noise amplifier (LNA) and other relevant probe electronics for reception. The probe is tuned to the Larmor frequency of the chosen nuclei at the applied background field strength, and it is matched to the impedance equaling the noise minimum of the LNA. Typically, the noise minimum is 50 Ω. A reactive matching and tuning network is preferred to conserve the SNR. Since typically $R_{coil} < 50\ \Omega$, the matching and tuning transformation produces the first amplitude gain for the signal. This

suppresses the effects of cable losses and electromagnetic interference picked up by the cable before the LNA.

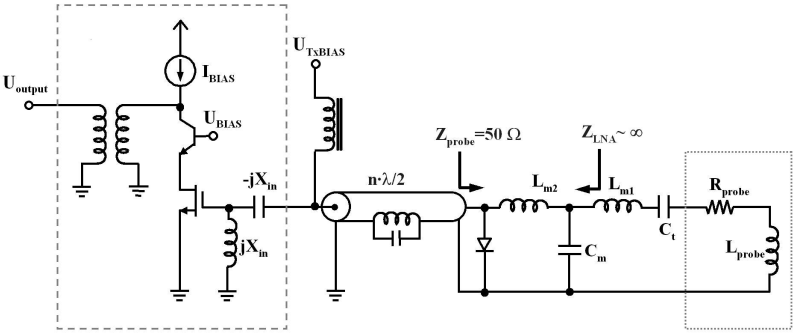

Fig. 6.4. *Electrical schematic of an NMR probe (the dotted box on the right) connected to an LNA (the dashed box on the left). The cascaded transistor network with operating point biases U_{BIAS} and I_{BIAS} illustrates a common LNA design for NMR applications. High-electron-mobility transistors (e.g., GaAs-based devices) are preferred for the input field-effect transistor. The capacitor and the inductor at the LNA input provide low impedance at the Larmor frequency. The NMR probe is tuned with a capacitor C_t and matched with a T-transform network (i.e., with inductors L_{m1} and L_{m2} and capacitor C_m). A balanced-unbalanced transformer, illustrated as an LC tank, is integrated into a $\lambda/2$ coaxial line connecting the LNA to the probe. To protect the LNA circuitry during RF excitations, a coil detuning PIN diode is driven into a conductive state by applying a positive voltage U_{TxBIAS}.*

To reduce coupling between NMR probes and imaging elements, a so-called low-input-impedance preamplifier decoupling technique is utilized [48]. In this scheme, a high-quality-factor LC circuit, tuned to the Larmor frequency, is connected at the gate of the input field-effect transistor of the LNA. Because the gate impedance of the field-effect transistor is high, the network looks like a series LC circuit to the probe, i.e., a very low impedance at the Larmor frequency. Now, L_{m2} and C_m are seen as a parallel resonator, and thus as a high-impedance current choke at the Larmor frequency. This scheme effectively reduces the current flow in the coil, i.e., coupling with any neighboring elements.

It is important to make sure that the tuned RF coil of a probe does not shield the RF excitation fields, especially if the probes are relying on MRI system excitations. During such high power transmissions, it is expected that the low-input-impedance decoupling scheme is insufficient. Thus, a more effective detuning

circuitry is required. This can be constructed by having a PIN diode in parallel to the matching and tuning network. During the transmit phase, the PIN diode is driven into a conductive stage that equals a very low impedance at RF frequencies. This low resistance in parallel with the coil and the preamplifier prevents any hazardous voltages or power buildups at the preamplifier input and further enhances the decoupling between the MRI transmit coil and the magnetic field monitoring probes.

Commercial LNAs with integrated RF shields are typically bulky to such an extent ($\sim$10 cm^2) that unwanted B_0 inhomogeneity and eddy-current-related fields may be introduced across the NMR sample and other objects in the vicinity. Therefore, the LNA in Fig. 6.4 is shown to be placed further away from the probe. The low-input-impedance decoupling scheme is not violated if the distance is a multiple of $\lambda/2$ at the Larmor frequency.

A balanced-unbalanced transformer is utilized to prevent any signal losses when connecting NMR probes (i.e., differential signal sources) to single-ended LNAs. This can be done with a bazooka-type balanced-unbalanced transformer integrated into the coaxial cable, for example [122]. By utilizing this technique, one suppresses effectively any potential coupling via common-mode cable currents. In addition, standing waves are suppressed during RF excitations, which would otherwise become potentially hazardous to patients.

6.3.2 Transmit-receive electronics

Based on the principle of reciprocity, the pick-up coil of an NMR probe can be utilized equally well for spin excitation as for signal detection [41]. Several methods exist to bring sufficient RF power to the coil and yet protect the sensitive receiver from damage [123, 124, 125]. Components based on ferromagnets, e.g., circulators, are out of the question, since MRI compatibility of the second kind is required for the utilized materials.

A type of a transmit-receive switch known as a PIN-diode-driven duplexer is shown in Fig. 6.5a. The scheme is reliable and easy to implement, and MRI compatible versions of the required components are readily available from commercial vendors. In comparison to GaAs field-effect-transistor-based transmit-receive switches, the PIN-diode-driven duplexers have higher power handling capabilities and a lower noise figure during reception.

The operation principle of such a duplexer is to have the PIN diodes reverse biased, i.e., corresponding to open circuits, during reception. Now, the circuitry functions like the receive-only circuitry shown earlier in Fig. 6.4. As diodes are reverse biased, no additional shot noise is coupled to the received signal. During the transmit phase, the diodes are forward biased, thus equaling short circuits at

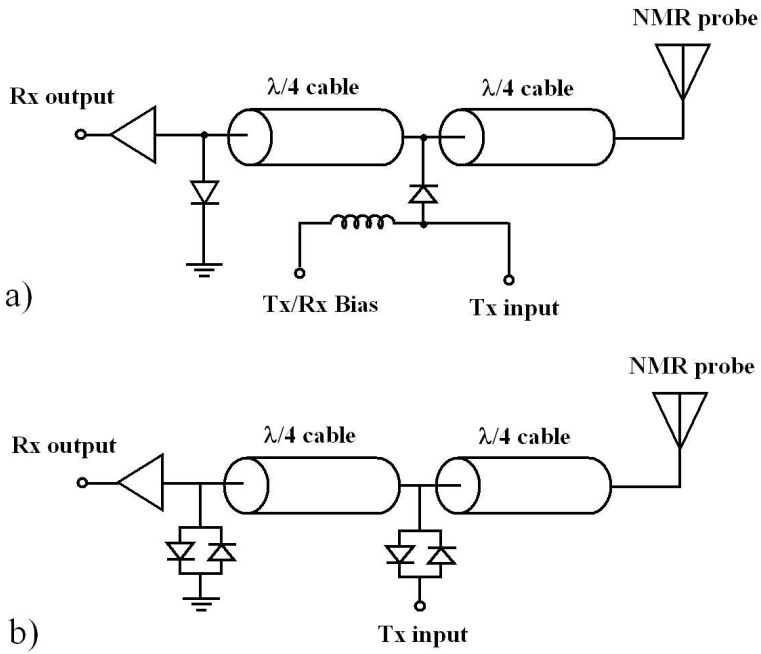

Fig. 6.5. *Schematics of duplexer-type RF transmit-receive switches based on (a) actively driven PIN diodes and (b) passive antiparallel diodes.*

radio frequencies. The diode at the LNA input is consecutively seen $\lambda/4$ away as an open circuit, and the transmit pulse, supplied through the second diode, will be completely absorbed by the RF coil, matched to 50 Ω.

Switching between the receive and the transmit mode can be made actively, as explained, or passively with crossed diode pairs, as is shown in Fig. 6.5b. In the passive design, it is assumed that the received NMR signal level is smaller than the threshold voltage for the diode forward biasing and that the transmit pulse amplitude is significantly larger than the threshold voltage. As the threshold voltage is typically $\sim$0.5 V and the NMR signal voltage is $\sim$1 μV, this assumption is valid with transmit power levels on the order of 30 dBm or more (i.e., at 50 Ω, transmit pulse amplitudes of $\geq$10 V).

A benefit of passive over active switching is a simpler design, which requires no driver electronics for the PIN diodes. Dependent on the antiparallel diodes, the switching can be done within approximately $\leq$10-ns transition times. Actively driven duplexers are significantly slower. This is because the

commercially available MRI-compatible PIN diodes are made with larger intrinsic areas than the MRI-compatible antiparallel diodes. The dissipation of stored charges is not the only slowing component of an active transmit-receive switch. RF chokes must be relatively large (>1 μH) to effectively block the NMR signals at relevant clinical MRI field strengths, which further increases the duration of the transient effects between switching. Typically, switching times of $\geq$5-20 μs are achievable with active switching. Coherent, short-interval excitations-based magnetic field monitoring sets stricter requirements for pulse widths (i.e., $\leq 1/f_m \approx 20$ μs), and the utilization of the passive duplexer design is therefore preferred. Benefits of active switching are typically higher power handling capabilities and lower transition losses during transmissions as the forward biasing reduces the diode forward resistance and obviates the pn-junction threshold voltage. In the receive mode, the performances of the two different switch designs are comparable since the diodes are in a nonconductive stage.

6.4 RF coil design

To design an optimal coil geometry for small-sized NMR samples, several references are recommended [46, 126, 127, 128]. In practice, the solenoid design outperforms other designs of comparable size [46]. In the following section, the relevant equations are introduced for analyzing solenoid microcoils.

The Biot-Savart law [41],

$$\mathbf{B}(\mathbf{r}) = \frac{\mu_0 I}{4\pi} \int_c \frac{d\mathbf{c}' \times (\mathbf{r} - \mathbf{r}')}{|\mathbf{r} - \mathbf{r}'|^3}, \tag{6.18}$$

gives the magnetic flux density around a conductor through which current I is flowing. Here, the ambient magnetic permeability is μ_0, $\mathbf{c}'$ describes the vector direction of the differential current element, $\mathbf{r}'$ is the location of this differential current section, and $\mathbf{r}$ is the point of observation.

Based on the principle of reciprocity, Eq. 6.18 can be utilized also for estimating the spatial receive sensitivity of the coil. Because applied wavelengths ($\sim$1 m) are considerably larger than the coil dimensions ($\sim$1 mm) at relevant Larmor frequencies in clinical MRI scanners, a quasistatic analysis based on the Biot-Savart law is considered applicable.

Figure 6.6 shows the sensitivity profile of an example solenoid coil. If the sample diameter is not too close to the coil diameter, one can estimate with good accuracy that the sensitivity profile perpendicular to the solenoid symmetry axis is constant. Thus, an analytical solution of the Biot-Savart law in this particular case becomes [128]

$$|\Psi_-(\mathbf{r})| \approx |\Psi_+(y)| = \frac{N\mu_0}{\sqrt{2}} \left[\frac{\frac{1}{2} + \frac{y}{l_{coil}}}{\sqrt{d_{coil}^2 + (l_{coil} + 2y)^2}} + \frac{\frac{1}{2} - \frac{y}{l_{coil}}}{\sqrt{d_{coil}^2 + (l_{coil} - 2y)^2}} \right], \tag{6.19}$$

where N is the number of turns, l_{coil} is the coil length, and d_{coil} is the coil diameter. The reduction of $\sqrt{2}$ in amplitude occurs because a solenoid is sensitive to a linearly polarized field, in contrast to the circularly polarized fields generated by spins.

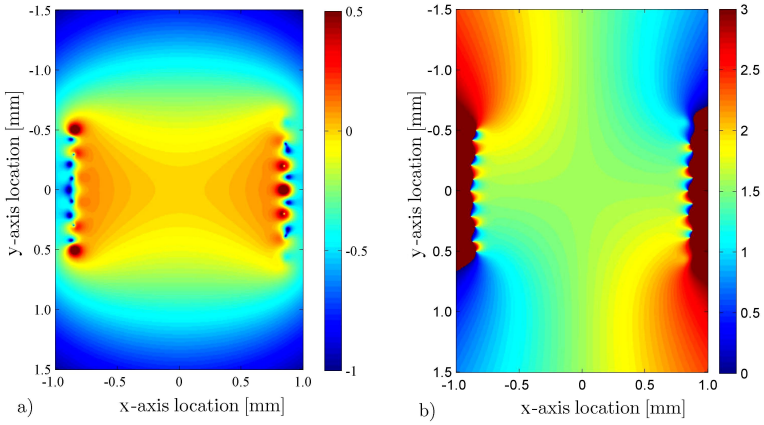

Fig. 6.6. *Sensitivity profile of a five-turn solenoid coil with a radius of 0.85 mm and a length of 1.0 mm. In (a) the absolute values on a logarithmic scale and in arbitrary units (a.u.) are illustrated. In (b), the phase profile in radians is plotted on a linear scale. One can observe that a relatively homogeneous sensitivity profile with a constant phase is obtained over an area of 1 mm × 1 mm in the middle of the solenoid.*

Inductance of a coil gives the relation between total magnetic flux through the loop and the loop current. Minard and Wind provide a semiempirical formula to calculate the inductance of a solenoid coil [128]:

$$L_{coil} = \left(\frac{9850 d_{coil} N^2}{4.5 + 10(l_{coil}/d_{coil})} \right) - 628 d_{coil} N (J_s + K_s)\ [nH]. \tag{6.20}$$

Here, the second term is introduced to take into account the finite number of turns. The given reference provides estimates for geometry-dependent variables J_s and K_s. If the probe is connected to the matching and tuning electronics with long leads, the effect of the lead inductance should also be considered, and

$$L_{leads} = 460 l_{leads} \log_{10}\left[4\left(\frac{l_{lead}}{d_{wire}}\right) - 0.75\right] \; [nH], \tag{6.21}$$

where d_{wire} is the wire diameter.

Probe losses are divided into the relevant components:

$$R_{probe} = R_{coil} + R'_{sample} + R_{leads} + R_{cap}, \tag{6.22}$$

where R'_{sample} is the Thevenin equivalent for R_{sample} seen at the probe output nodes. Here, R_{leads} describes the effect of the losses in the leads that are utilized to connect the probe to a tuning capacitor. In the SNR calculations, the capacitor losses, R_{cap}, should be noted as well, and the value can be obtained from the component manufacturer.

When calculating the wire and the coil resistances, it is estimated that the wire diameter is significantly larger than the skin depth, δ_s:

$$\delta_s = \frac{1}{\sqrt{\pi f \sigma \mu_c}}, \tag{6.23}$$

where σ is the material conductivity and μ_c is the magnetic permeability of the conductor. For example, at the ^{1}H Larmor frequency with a 3.0-T background flux density, $\delta_s = 5.8$ μm. In the skin-depth-limited case, one gets for the wire resistance R_{leads} that

$$R_{leads} = \frac{l_{wire}}{d_{wire}} \sqrt{\frac{\mu f}{\pi \sigma}}, \tag{6.24}$$

where l_{wire} is the wire length and d_{wire} is the wire diameter. Equation 6.24 can be applied for estimating the electric losses in solenoid coils as long as electrical interactions between adjacent loops are also taken into consideration. This is done with a so-called enhancement factor, ζ, an experimental factor dependent on the proximity of the adjacent coil turns [128], and so

$$R_{coil} = \zeta \frac{N d_{coil}}{d_{wire}} \sqrt{\frac{\pi \mu f}{\sigma}}. \tag{6.25}$$

Reference [128] provides a table of ζ values for various coil geometries. The first and last turns of the solenoid experience approximately half the proximity effect that the turns in the middle of the solenoid are experiencing. Thus, a modified enhancement factor ζ' is recommended for solenoids with small number of turns, and this can be written as

$$\zeta' \approx 1 + (\zeta - 1)\left(1 - \frac{1}{N}\right). \tag{6.26}$$

Sample losses can be further divided between dielectric and magnetic losses:

$$R'_{sample} = R_e + R_m. \tag{6.27}$$

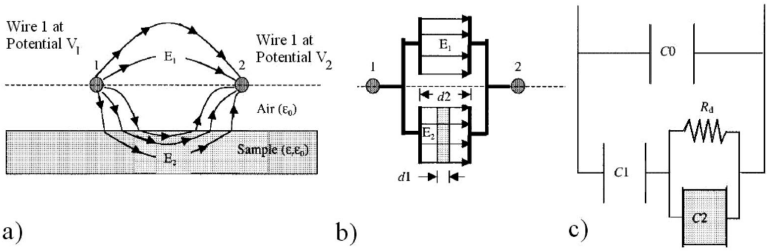

Fig. 6.7. *(a) Penetrating electric fields cause the polarization of particles in an NMR sample. (b) This can be modeled as a series combination of a lossy and an ideal capacitor. (c) The dielectric losses can be further studied with an equivalent electrical circuit model. Here, C0 and C1 are lossless air capacitors, and C2 is a capacitance over the sample with a loss component R_d. (Figures are reprinted with permission from [128].)*

The dielectric losses in the sample can be modeled as a lossy capacitor connected in parallel with the coil (cf. Fig. 6.7). The dielectric properties of utilized materials can be divided between nonconductive ε' and conductive ε'' parts [128]:

$$\varepsilon(\omega) = \varepsilon'(\omega) + j\varepsilon''(\omega). \tag{6.28}$$

For dielectric losses in the NMR sample, R_d, it can be shown that

$$R_d = \frac{\varepsilon'(\omega)}{\omega C2\varepsilon''(\omega)}. \tag{6.29}$$

This lossy element can be transformed by circuit analysis to an element in series with the coil (thus to R_e), and

$$R_e = \omega^2 L_{coil}^2 Y_{real}. \tag{6.30}$$

Here, Y_{real} is the equivalent conductance of the circuit in Fig. 6.7c, and it can be shown that

$$Y_{real} = \frac{\omega^2 R_d C1^2}{1 + \omega^2 R_d^2 (C1 + C2)^2}, \tag{6.31}$$

where capacitances $C1$ and $C2$ can be estimated as

$$C1 = \frac{\pi \varepsilon_0 d_{coil}}{2 \ln(d_{coil}/d_{sample})} \tag{6.32}$$

and

$$C2 = \frac{\varepsilon'(\omega)\varepsilon_0 \pi d_{sample}^2}{4 l_{coil}}. \tag{6.33}$$

Here, d_{sample} is the sample diameter, and l_{coil} is the coil length, which should be equal to or smaller than the sample length, l_{sample}.

A time-invariant field induces currents in any conductive sample, and vice versa: Current noise in conductive samples induces magnetic noise. For cylindrical samples [128],

$$R_m = \frac{\pi \sigma_{sample} l_{sample} \omega_0^2 \mu_0^2 N^2 d_{sample}^4}{128(d_{coil}^2 + l_{sample}^2)}, \tag{6.34}$$

where σ_{sample} is the sample conductivity. One should note here the power of four dependency on the sample diameter.

The so-called quality factor (Q) describes the effectiveness of a resonator as a ratio between the stored and the dissipated energy:

$$Q = \frac{E_{stored}}{E_{dissipated}} = \frac{\omega_0 L}{R} = \frac{\omega_0}{\mathrm{BW_{FWHM}}}, \tag{6.35}$$

where ω_0 is the resonance frequency and $\mathrm{BW_{FWHM}}$ is the full width at half-maximum bandwidth. The quality factor is especially useful in studying the ratio between intrinsic losses (i.e., coil losses) and sample losses. The comparison is achieved by studying the quality factors in unloaded and loaded cases, i.e., with and without the sample.

6.5 Decoupling strategies for NMR probes

A magnetic field monitoring system should not interfere with standard imaging experiments. Signal coupling directly from ^{1}H or other imaging nuclei and indirectly via RF coils are issues to be carefully addressed in designing an NMR-based field monitoring system. In addition to the low-input-impedance preamplifier decoupling technique, the probe-to-probe and probe-to-coil coupling can be reduced by using counterwound solenoid coils. If probes are utilized in transmit-receive fashion, a thin RF shield can effectively reduce the coupling. Alternatively, different nuclei for magnetic field monitoring can be exploited if separate, multinuclear transmit-receive hardware is available. In this section, all these methods are more closely studied.

6.5.1 Counterwound coils

A secondary solenoid coil can be counterwound in series with the primary solenoid coil for NMR signal detection. The counterwound coil can be placed in a way such that it is far enough not to significantly pick up the NMR signal from the sample but close enough so that it will experience roughly the same RF field originating from the neighboring elements as the main coil. In this configuration, the external magnetic fields induce voltages in the counterwindings of an opposite sign to the induced voltages in the main coil, thus suppressing the coupling. As a drawback, the SNR is estimated to be reduced by the increased coil losses (-3 dB) and by the amount of any stray signal that gets picked up by the counterwound coils.

The counterwound coil decoupling concept is further studied by solving coil-sensitivity profiles from the Biot-Savart law, i.e., Eq. 6.18. The outcome of the simulations with respect to a typical ^{1}H coil geometry is illustrated in Fig. 6.8. From the simulations, it is estimated that a reduction of approximately -10 to -15 dB in coupling is achievable with this technique. From Fig. 6.8 one can also note that the sensitivity over the NMR sample, i.e., SNR, is not expected to get significantly reduced by the counterwindings. Hence the expected SNR losses is mostly due to the increased conductor length.

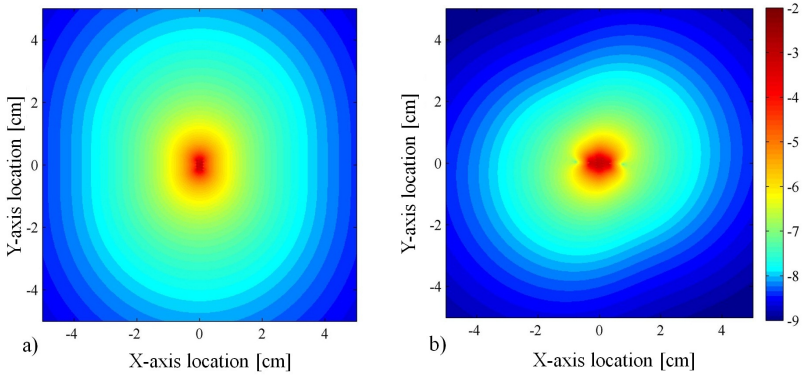

Fig. 6.8. *Sensitivity profiles of two different coil designs illustrated in units teslas per ampere on a logarithmic scale. (a) Magnetic field strength outside of a four-turn coil is reduced by (b) connecting two counterwound two-turn coils in series with the main coil.*

6.5.2 RF shielding

If an independent RF transmitter is at hand, one can excite the probes locally and wrap a thin metal sheet around the NMR probes to block interfering RF fields. If the shield thickness is kept small, roughly on the order of the skin depth at the Larmor frequency, this design is assumed to cause only small variations in the gradient fields.

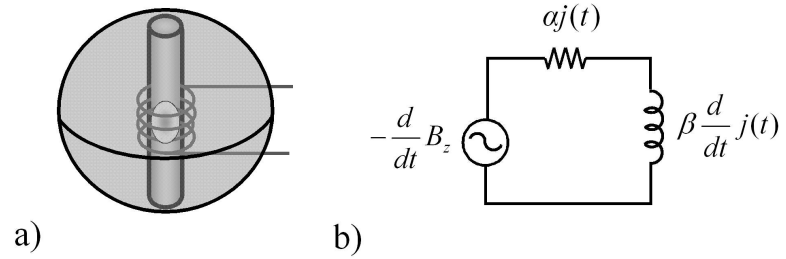

Fig. 6.9. *(a) Illustration of a spherical RF shield wrapped around an NMR probe, and (b) an equivalent electrical circuit of the shield to model the eddy current behavior. Here, symbols α and β stand for constants related to the shield geometry.*

Typically eddy current calculations in conductive structures become complex, and analytical solutions exist only in some special cases [41, 129, 130]. Here, for simplicity, a spherical shield with a diameter a and a thickness t_h is considered along with the application of a spatially uniform magnetic field along the z axis (cf. Fig 6.9a). If a current density is presented in the polar coordinate system as $\mathbf{j} = j_0 \sin\theta \hat{\mathbf{u}}_\varphi$, where $0 \leq \theta \leq \pi$, a differential equation related to the induced eddy current can be written based on Kirchhoff's voltage law (cf. Fig. 6.9b) [129]:

$$\frac{d}{dt}j_0 + \frac{3\sin\theta}{\mu_0 t_h \sigma a} j_0 = -\frac{3}{2t_h\mu_0}\frac{d}{dt}B_z. \tag{6.36}$$

The solution of this differential equation for a sinusoidal stimulus $\mathbf{B}_0 = B_0 e^{i\omega t}\hat{\mathbf{u}}_z$ becomes

$$j_0 = -\frac{i\omega}{\frac{2}{\sigma a} + i\frac{2t_h\mu_0\omega}{3\sin\theta}} B_0 e^{i\omega t} = \frac{1}{\Psi_s(\theta)} B_0 e^{i\omega t}, \tag{6.37}$$

where $\Psi_s(\theta)$ is the sensitivity of the conductor section. The differential current element can be introduced into the Biot-Savart law (Eq. 6.18) to calculate the flux density component from the eddy current:

$$\mathbf{B}_{eddy} = \frac{\mu_0}{4\pi}\int_V \frac{(\mathbf{j}\,dV)\times\mathbf{r}}{r^3} = \frac{\mu_0}{4\pi}\int_V \frac{(\sin\theta\, j_0\hat{\mathbf{u}}_\varphi\, dV)\times\mathbf{r}}{r^3}. \tag{6.38}$$

In the center of the sphere, for the total field one can write

$$\frac{\mathbf{B}_{tot}}{|\mathbf{B}_0|} = \left(1+\frac{\mu_0 t_h}{2}\int_0^\pi \frac{\sin^2\theta}{\Psi_s(\theta)}d\theta\right)\hat{\mathbf{u}}_z. \tag{6.39}$$

Figure 6.10 illustrates the total field as a function of frequency in the middle of a spherical RF shield, based on different shield radii. Here, it is estimated that a shield with a thickness of $t_h = 5\delta_s$ at 127.8 MHz would already provide the sufficient increase in isolation for the standard, long-interval excitations scheme. If probes are based on the coherent, short-interval excitations scheme, thicker shielding is required owing to the expected larger amplitude of the transmission pulses. It is estimated that the RF pulse can be up to 100 dB larger in comparison to the NMR signal, thus indicating a required shield thickness of $h \approx 25\delta_s$.

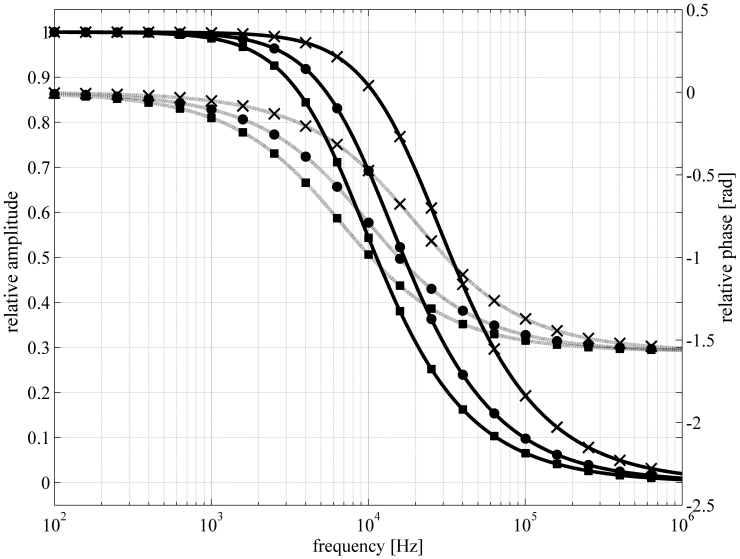

Fig. 6.10. *Screening effect to magnetic fields from a spherical RF shield. The total relative field is plotted at the center of three spheres with different diameters (a = 1.0 cm, ×; a = 2.0 cm, •, a = 3.0 cm, ■). Here, the absolute field values are illustrated with solid lines, and the phase values with dotted ones.*

The simulations show that at gradient frequencies relevant to MRI, i.e., ≤ 25 kHz, shields with the thickness $t_h = 5\delta_s$ alter the fields in a significant manner already. Furthermore, it can be concluded from the simulations that the larger the shield, the stronger the screening effect becomes at lower frequencies. It is also noticed from the simulations that the shielding causes more phase shifting than attenuation at frequencies roughly below 5 kHz. Such shifts correspond to a delayed monitoring signal and can be compensated in to some extent by calibration routines [131]. Simulations show also that in the megahertz range the shielding already screens most of the applied signal.

The cutoff frequency of the RF shielding can be increased by decreasing the shield dimensions within the limits of the NMR probe size. It should be noted, however, that if the RF shield is made very close to the NMR probe, undesired noise coupling between the solenoid and the shield is experienced. Reducing the shield thickness to $t_h = 3\delta_s$ shifts the -3-dB attenuation point to higher frequencies by roughly 60%-70% with the simulated sphere diameters. This outcome is a compromise solution, and a -3-dB point still would lay at the relevant measurement bandwidth. Also, with the reduced shield thickness, the isolation between NMR probes and imaging elements gets compromised, especially if NMR probes are being excited during image acquisition.

Utilizing RF shields for signal decoupling introduces some further challenges because NMR probes are expected to be placed close to patients as well as to imaging coils. The shield can alter the sensitivity profile of the coil, as well as introduce additional loading to some extent, i.e., an increase in detected noise and a detuning of the coil resonance frequency. If probes are placed closer to patients instead, high electric fields can be induced around the shield during RF excitations and potentially increase local SAR, thus jeopardizing patient safety.

6.5.3 Non-proton-based NMR probes

At relevant clinical background magnetic field strengths and gradient swings, the center frequencies and signal bandwidths of different nonzero-spin nuclei are distributed relatively sparsely, as illustrated in Fig. 6.11. Hence, coupling between MRI hardware and field monitoring probes can be reduced significantly by using nuclei different from ^{1}H for the NMR probe design. Therefore the use nonideal decoupling strategies, such as counterwindings or RF shields, is no longer required. As a drawback, a separate RF transmit-receive system is required for the implementation since typical MRI scanners can operate only at a single Larmor frequency at a time.

One of the benefits of utilizing ^{1}H nuclei for NMR probes is the very high gyromagnetic ratio of the nuclei. A naive assumption from Eq. 6.14 is that the

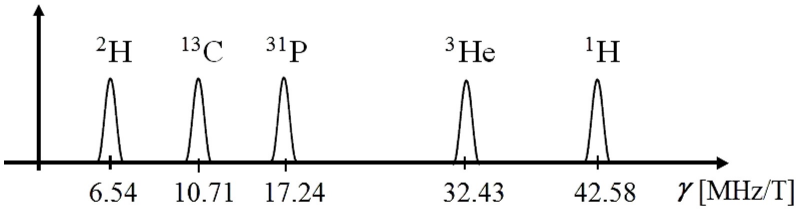

Fig. 6.11. *Selected NMR nuclei are illustrated with respect to their gyromagnetic ratios.*

achieved signal is reduced by a factor of $(\gamma_X/\gamma_{1_H})^3$ when one utilizes nuclei with lower gyromagnetic ratios, noted here with the letter X. A more in-depth analysis of Eq. 6.15, however, shows that several parameters can be turned in favor of nuclei with smaller gyromagnetic ratio.

The sampling bandwidth can be reduced by (γ_X/γ_{1_H}). However, this only holds true down to 50 kHz, which is estimated to be the Nyquist sampling rate for the highest significant magnetic field component for MRI.

Signal dephasing during imaging restricts NMR probe sample sizes in the standard, long-interval excitations-based field monitoring. A lower gyromagnetic ratio relates to slower dephasing, and one gets from Eqs. 2.15 and 6.7 that the sample volume can be increased in a similar fashion to compensate for the $(\gamma_X/\gamma_{1_H})^3$ signal loss.

Scaling up the dimensions can be further studied. From Eq. 6.19, one gets that scaling up the probe dimensions by (γ_{1_H}/γ_X) reduces the solenoid coil sensitivity by approximately the same factor. Furthermore, it is seen from Eq. 6.25 that, if the probe losses are dominated by coil losses, scaling up in dimensions leads to a case where only the skin-depth-based reduction in the coil resistance remains, and thus $\sqrt{\gamma_X/\gamma_{1_H}}$.

The influences of all the components affecting the measurement SNR are combined in Eq. 6.15, and one gets that

$$\frac{\mathrm{SNR}_X}{\mathrm{SNR}_{1_H}} \approx \frac{\left(\frac{\gamma_X}{\gamma_{1_H}}\right)^3 \left(\frac{\gamma_X}{\gamma_{1_H}}\right)^{-3} \frac{\gamma_X}{\gamma_{1_H}}}{\sqrt{\frac{\gamma_X}{\gamma_{1_H}}\sqrt{\frac{\gamma_X}{\gamma_{1_H}}}}} = \left(\frac{\gamma_X}{\gamma_{1_H}}\right)^{1/4}. \tag{6.40}$$

Thus, only a relatively minor reduction in SNR is estimated when one changes from ^{1}H to another NMR nucleus with a smaller γ. With coherent, short-interval excitations-based NMR probes, the high level of sample doping for required T1 characteristics (i.e., $\sim$100 μs) results in the sample magnetic losses dominating the total probe losses. From Eq. 6.34 one sees that, if sample size is increased to

compensate for the reduced gyromagnetic ratio, the total magnetic losses remain unaltered (assuming that the coil dimensions scale up in similar fashion). Thus, the outcome of Eq. 6.40 becomes

$$\frac{\mathrm{SNR_X}}{\mathrm{SNR_{^1H}}} \approx \frac{\left(\frac{\gamma_X}{\gamma_{^1H}}\right)^3 \left(\frac{\gamma_X}{\gamma_{^1H}}\right)^{-3} \frac{\gamma_X}{\gamma_{^1H}}}{\sqrt{\frac{\gamma_X}{\gamma_{^1H}}}} = \left(\frac{\gamma_X}{\gamma_{^1H}}\right)^{1/2}. \tag{6.41}$$

In addition to practically eliminating cross-coupling with ^{1}H imaging, a smaller gyromagnetic ratio brings certain other benefits. Probe-to-probe coupling is reduced owing to the smaller Larmor frequency. The unwrapping algorithm for the signal phase has a smaller chance of failure during high-gradient performance owing to the lower MR signal bandwidths (cf. Eq. 6.6). High-resolution (<0.5 mm) as well as non-proton-based imaging requires smaller NMR sample sizes if NMR probes are based on the standard, long-interval excitations scheme because of the larger gradient envelopes that are applied (cf. Eqs. 2.15 and 6.7). Such probes become difficult to manufacture if these are based on ^{1}H nuclei, and winding the coil close to the sample for high filling factors becomes more challenging. With a smaller gyromagnetic ratio (and thus larger sample sizes), the filling factors are less affected by the coil wire diameter or the sample holder dimensions, e.g., by the wall thickness of a glass capillary.

To avoid premature dephasing of the signal, intrinsic field inhomogeneities over the sample volume should be constrained. This is an especially demanding task if NMR probes are operated with the standard, long-interval excitations-based operation scheme. The requirement for field homogeneity is reduced by a factor of $(\gamma_X/\gamma_{^1H})$ for the benefit of non-proton-based probes (cf. Eq. 6.2), making the manufacturing process of susceptibility-matched probes less demanding for the standard, long-interval excitations-based operation scheme. Furthermore, objects with different susceptibilities can now be placed closer to the probe. This becomes relevant, for example, when the probes are integrated into an imaging coil, a stereotactic frame, or a patient table. An additional benefit is that non-proton-based probes have higher robustness to inherent background field inhomogeneities inside the magnet bore, e.g., fringe fields, and can therefore be placed further away from the isocenter.

6.6 Discussion and conclusions

NMR-based magnetometer systems can be operated in a pulsed mode for higher signal levels than are achievable with continuous-mode operated probes. Here,

the signal from relaxing spins after an excitation pulse is monitored. The signal phase is proportional to the time integral of the applied magnetic field, and hence to a temporal location in k space. In this chapter, different ways to operate NMR probes in the clinical MRI environment have been presented, and the theoretical background on how to optimize sensing electronics for high SNR has been outlined. The simplest form of utilizing NMR probes in MRI is to have matching nuclei with imaging and to exploit the transmit and receive hardware of the MRI system. This method, however, requires that the MRI pulse designs have to be tailored for field monitoring assisted imaging often with compromised performance, e.g., required volume excitation prior to imaging. Also, the minimum number of receiver channels is increased to accommodate the field monitoring probes as well. Signal coupling between the imaging and monitoring systems must be carefully addressed because they operate at the same frequencies. To gain independence from MRI volume excitations, a separate transmit-receiver can be manufactured. This also enables the utilization of RF shields over the NMR probes for reduced cross-coupling with imaging.

The spin ensemble in an NMR magnetometer can either be excited once per each imaging repetition with the standard, long-interval excitations-based operation scheme or multiple times with the short-interval phase-coherent excitations-based operation scheme. A limitation of standard, long-interval excitations-based monitoring is that the probe operation cannot be optimized simultaneously for short and for long repetition time acquisitions. To avoid premature signal dephasing, the concept also sets strict requirements for the sample size, as well as for the level of background magnetic field inhomogeneity over the NMR sample. The former criterion limits the achievable SNR especially in high-resolution imaging, and both criteria make the manufacturing of NMR probes more complicated.

Exciting NMR probes in short intervals with coherent RF pulses allows higher robustness against different imaging parameters such as repetition rate and resolution. In addition, the field homogeneity requirement over the sample volume becomes relaxed and larger sample sizes for higher SNR become possible. For this operation scheme, specialized hardware to phase-lock the excitation pulses with the precessing spins is required to ensure high SNR and to avoid destructive interference in transverse magnetization.

Both NMR probe operation schemes require decoupling methods to ensure that NMR probes and imaging do not interfere with each other. In this respect, standard, long-interval excitations-based monitoring is less demanding since only the NMR signals must be suppressed from coupling to standard imaging; in comparison to transmit pulses, the NMR signal amplitude can be five to six orders of magnitude lower. Unlike counterwound solenoid coils, the utilization

of RF shields is more effective at reducing the cross-coupling to a level that causes artifacts neither to imaging nor to monitoring. As excitations from an MRI system cannot penetrate the RF shield, a separate transmitter for the probes is compulsory. The drawbacks of RF-shielded probes in comparison to counter-wound coils are corrupted field monitoring data at higher frequencies, potential SNR reduction in imaging coils and in NMR probes from noise coupling from the conductive shield, potential B_1 artifacts in standard imaging, and the possibility of compromised patient safety and increased SAR from higher electric fields at the proximity of the shield.

The use of non-proton-based NMR probes offers a more sophisticated approach to tackle the decoupling issue. With this method, strong decoupling is achieved without the negative side effects of RF shields. The utilization of non-proton-based NMR probes requires separate transmit-receive hardware since a normal MRI system can typically operate only at a single frequency band at a time. This is not considered to be a restricting drawback since a separate transmit-receive system is nevertheless desired to operate NMR probes independently and can be potentially valuable for retrofit applications as well. In the following chapter, it will be shown that such hardware can easily be manufactured from off-the-self components.

7

Independent Transmit-Receive Hardware for MR Applications

A magnetic field monitoring system can be made independent of the MRI system's excitations by using separate RF transmitter hardware. Using an independent transmitter ensures that the optimal flip angles are achieved regardless of the applied MRI sequence. In addition, probe placement is no longer restricted to being within the excitation volume of the imaged object.

Standard clinical MRI scanners are typically made for ^{1}H detection alone. Although operations at many Larmor frequencies become possible with separate multinuclear hardware, spins with different Larmor frequencies can be excited and detected only one at a time. However, simultaneous multinuclear detection would enable the utilization of non-proton-based NMR probes for magnetic field monitoring. Moving away from ^{1}H-based probes would offer enhanced signal decoupling with standard MRI acquisitions and certain other benefits with respect to manufacturing, miniaturizing, and probe placement.

In this chapter, novel transmit-receive hardware for multiband MR excitations and reception is presented. The designed hardware can be supplemented with a specialized feedback loop for maintaining the coherency between sample spins and RF pulses. This hardware is preferred if short (TR $\ll$ T1) acquisitions are used or the coherent, short-interval excitations-based monitoring scheme is applied.

7.1 RF transmitter for single-pulse excitations

A separate RF transmitter ensures the RF power required for optimal excitations of NMR probes. High flip angles should also be achieved in the presence of gradient activity to ensure independence from applied imaging sequences. In typical

MRI configurations, this dictates transmission bandwidths of approximately 1 MHz for ^{1}H-based NMR probes. Because the transmitter can be placed far from the magnet bore, no MRI compatibility is required of the utilized components.

The relationship between the applied RF excitation flux density, B_{1-}, and the obtained flip angle, θ, is given by Eq. 2.5. On resonance, and in the absence of gradient fields, it can be shown that

$$\theta(\mathbf{r}) = \gamma \int_{\Delta t} B_{1-}(\mathbf{r}) dt = \gamma \Psi_-(\mathbf{r}) I_{RF} \Delta t, \tag{7.1}$$

where $\Psi_-(\mathbf{r})$ is the probe sensitivity, I_{RF} is the RF drive current, and Δt is the pulse duration. The required RF power, P_{RF}, for a given flip angle and excitation pulse length becomes

$$P_{RF} = R_{probe} I_{RF}^2 = R_{probe} \left(\frac{\theta(\mathbf{r})}{\gamma \Psi_-(\mathbf{r}) \Delta t} \right)^2. \tag{7.2}$$

For a nonhomogeneous excitation profile, the equation that describes the NMR signal level, i.e., Eq. 6.14 should be rewritten, and

$$U_{probe}(t) = \omega_d \int_V \sin(\gamma \Psi_-(\mathbf{r}) I_{RF} \Delta t) \Psi_-(\mathbf{r}) M_{x,y}(\mathbf{r}) e^{i(\varphi(t,\mathbf{r}) + \omega_d t)} d\mathbf{r}. \tag{7.3}$$

Gradient fields change the Larmor frequency experienced by an individual probe, and it is preferred that the probe excitation covers the complete bandwidth determined by the maximum gradient strength achievable with MRI systems ($\sim$1 MHz). This removes the restriction of the time point of excitation belonging to regions of low gradient activity only. Utilization of sinc-shaped excitation pulses in the time domain ensures the ideal rectangular frequency spectra over the desired bandwidth. Such pulses can be easily generated with an arbitrary wave generator, for example. A more cost-effective approach with acceptable performance is to generate hard pulses by chopping an output of a frequency synthesizer with an RF switch (cf. Fig. 7.1). The Fourier transform of the transmission signal indicates a sinc-shaped spectrum with the full width at half-maximum bandwidth given as

$$\mathrm{BW}_{\mathrm{FWHM}} \approx \frac{1}{1.21 \Delta t}. \tag{7.4}$$

Thus, the desired transmission bandwidths of roughly 1 MHz would be ensured by 0.8-μs-long hard pulses.

Power requirements for a separate transmitter must be considered since this parameter can significantly increase the total cost of an NMR-based field monitoring system. For example, a relatively constant sensitivity Ψ_- of $\sim$1.5 mT/A

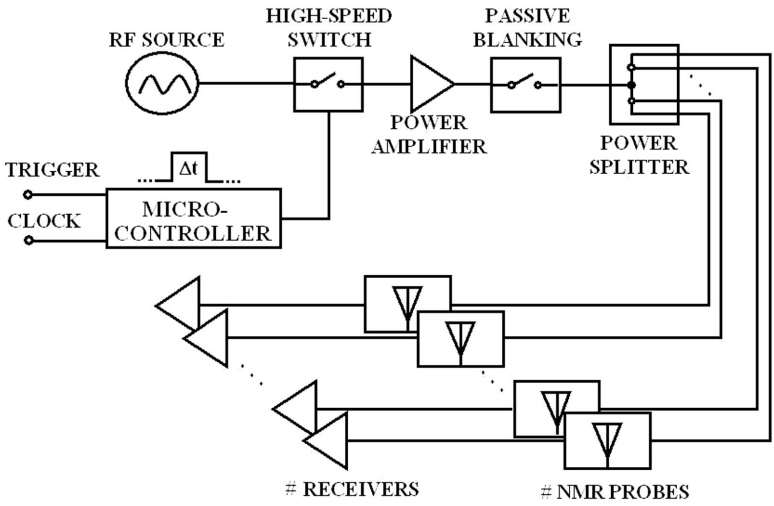

Fig. 7.1. *Schematic of a transmit-receive chain for operating passively switched transmit-receive NMR probes. A microcontroller controls the timing and pulse lengths of the transmit pulses after receiving a trigger signal from the MRI system.*

over the sample volume can be calculated from Eq. 6.19 for an ^{1}H probe having typical coil parameter values (5 turns, 1.6 mm diameter, 0.3 mm copper wire thickness, and 0.1 mm spacing in windings). By combining Eqs. 6.22 and 7.2, it can be concluded that such a coil requires a power of 4.5 W to produce the desired 90° flip angles with a pulse duration of 0.83 μs.

When determining the power levels required to excite non-proton-based NMR probes, several aspects need to be considered. The reduced gyromagnetic ratio reflects a loss of γ_X/γ_{1_H} in the efficiency of transmit pulses (cf. Eq. 7.1). In Chapter 6 it was shown that with non-proton-based probes, sample diameters can be increased to compensate for the otherwise expected signal loss from the smaller gyromagnetic ratio. Such an increase in the sample and consequently in the coil diameter however corresponds to a reduced (transmit) sensitivity of γ_X/γ_{1_H} (cf. Eq. 6.19). For the benefit of non-proton-based NMR probes, the skin depth is increased by $\sqrt{\gamma_{1_H}/\gamma_X}$. If NMR samples of low conductivity are used, the change in skin depth relates to a reduction in the total coil losses with the same ratio, as is shown by Eq. 6.26. If the total influence of the individual components are calculated together, and if one assumes that the transmit power is restricted, based on Eq. 7.1 one can conclude that the transmit pulse length in-

creases by a factor of approximately $(\gamma_{1_H}/\gamma_X)^{7/4}$ to ensure the same flip angle. Vice versa, if the pulse length is kept constant, the RF transmitter power must be increased significantly, i.e., by a factor of $(\gamma_{1_H}/\gamma_X)^{15/4}$, as is seen from Eq. 7.2,

The shift in the Larmor frequencies of low-gamma NMR probes owing to gradient fields is reduced by (γ_X/γ_{1_H}) (cf. Eq. 2.15). This relates to a corresponding reduction in the transmission bandwidths required to cover the complete spectrum of NMR sample Larmor frequencies, and hence longer transmission pulses can be applied. This allowable increase in pulse widths does not completely compensate for the loss in the efficiency of RF pulses. Increasing the pulse width by γ_{1_H}/γ_X reduces the power increment requirement to $(\gamma_X/\gamma_{1_H})^{7/4}$.

Because the number of NMR probes for field monitoring can range from 4 to approximately 32, the required power levels become relatively large, and more expensive power amplifiers are required. The power requirement is drastically reduced if one has a timing control to ensure that the transmit pulses do not occur during very strong gradient activity, e.g., crusher gradients. Based on typical MRI acquisitions, the accuracy of such timing is estimated to be on the order of 10 μs.

7.2 RF transmitter for single-pulse excitations: implementation

A homemade RF pulse transmitter was manufactured for operating NMR probes with the standard, long-interval excitations scheme. A12-bit frequency synthesizer (PXI-5404, National Instruments, Houston, TX) functioned as the sinusoidal signal source. In combination with a passive frequency doubler (MK-3, Mini-Circuits, Brooklyn, NY), the operating bandwidths can be extended up to 210 MHz, which ensured RF excitations for all the existing NMR nuclei exposed to 4.7-T magnetic flux densities or below.

A high-speed single-pole-double-throw switch (ZASW-2-50DR, Mini-Circuits, Brooklyn, NY) provided high (82 dB) isolation, 1.4-dB insertion loss in on-state, and fast pulse chopping at transients below 10 ns. A 5-W power amplifier (ZHL-03-5WF, Mini-Circuits, Brooklyn, NY) was sufficient to provide 90° excitation pulses for four to eight ^{1}H NMR probes at nominal pulse durations of 2-5 μs. Hence, this correlated the full width at half-maximum bandwidths of 410-170 kHz, giving good transmission efficiency also at moderately strong gradient activity. For dividing the RF power to individual probes, commercial power splitters, e.g., ZSC-4.3 (Mini-Circuits, Brooklyn, NY), were utilized.

A blanking switch after the power amplifier was implemented to ensure that amplified noise from the 50 Ω output termination of the RF switch would not

significantly leak through the transmit-receive switches in the NMR probes during signal reception. In this work, a passive medium-power switch, shown in Fig. 7.2, was designed and manufactured. The benefits of such a passive switch, in comparison to active ones, were easier implementation owing to the absence of any biasing network and faster switching times. The implemented switch had a narrow frequency bandwidth defined by the construction, and the $\lambda/4$ cables in the switch design (or comparable discrete components) must be retuned if it is applied for different NMR nuclei.

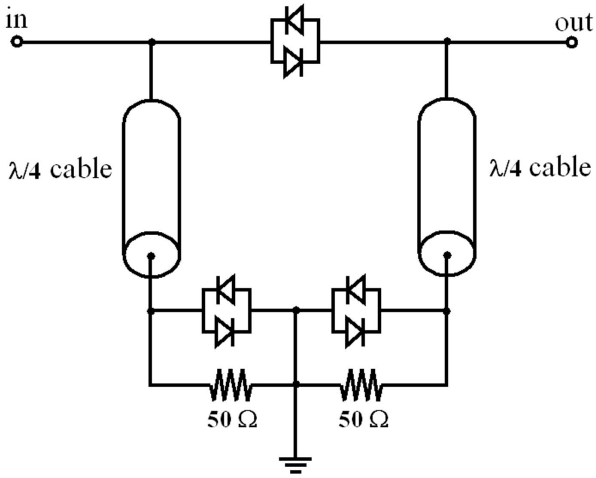

Fig. 7.2. *Schematic of a passive switch to isolate an RF transmitter output during signal reception. During high-power transmission signals, the antiparallel diodes become conductive, thus isolating the 50 Ω terminations and shorting the in and out ports.*

7.3 Design and implementation of an RF transmitter for phase-coherent excitations

If excitation intervals become smaller than T1 and no coherence is maintained with the precessing spins and the consecutive excitations, the amplitude of transverse magnetization after each excitation becomes pseudo-random over the steady-state value determined by Eq. 6.9. For robust field monitoring, such a characteristic is undesired because the transverse magnetization may have values

low enough to jeopardize the SNR requirement and the reliability of the phase-unwrapping algorithm. To make NMR probes more independent from the repetition time of image acquisitions, hardware that ensures that excitations are phase-locked to precessing spins becomes a necessity. More importantly, phase-locked excitations allow the utilization of the coherent, short-interval excitations-based operation scheme, which facilitates higher SNR, provides shorter TR values, and makes NMR-based monitoring more immune to strong gradient waveforms, such as are experienced during high-resolution imaging.

A block diagram of a circuit that ensures phase-coherent excitations with respect to the excited spin ensemble is shown in Fig. 7.3. The design is based on positive feedback, which detects the received signal and amplifies it to power levels corresponding to the required flip angle. For the initial RF pulse, a simple hard-pulse RF exciter as was described in the previous section can be utilized.

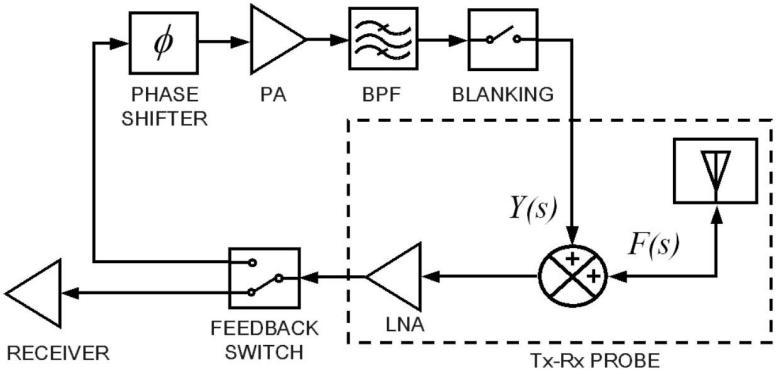

Fig. 7.3. *Block diagram of a positive-feedback-based exciter, which ensures phase coherency between RF pulses and an NMR spin ensemble. Here, LNA stands for a low-noise amplifier, PA for a power amplifier. and,BPF for a band-pass filter. The dashed box indicates the duplexer-based transmit-receive probe design.*

If band-pass filtering is omitted, one can write for the closed-loop gain of the feedback system that

$$\frac{Y(s)}{F(s)} = \frac{A_{\text{gain}} e^{-\tau_0 s}}{1 - A_{\text{gain}} e^{-\tau_0 s}}, \tag{7.5}$$

where $Y(s)$ is the Laplace-transformed output (i.e., the feedback signal), $F(s)$ is the input signal, A_{gain} is the gain, and τ_0 is the delay. The system is inherently unstable for $A(s)e^{-\tau_0 s} > 0$. If only the stimulating frequency component, ω_0, is

considered, the system is simulated (LT Spice, Linear Technologies, Milpitas, CA) to follow roughly a delayed exponential growth:

$$y(t) \approx \alpha e^{(\beta + i\omega_0)(t-\tau_0)}, \tag{7.6}$$

where α and β are constants. Exponential growth is limited by saturation in the gain block of the feedback loop. By adjusting the delay, one ensures that the feedback signal is in -90° phase with the precessing spins (cf. Eq. 7.6).

The total allowable electrical delay of the feedback loop is restricted by the group delay. One can formulate the following criterion to ensure that the phase response of the feedback amplifier does not significantly vary over the signal bandwidth:

$$\gamma G_{\max} |\mathbf{r}| \, \tau_0 < \Delta\varphi, \tag{7.7}$$

where $\mathbf{r}$ is the probe location and $\Delta\varphi$ is the acceptable phase error. If a limit $\Delta\varphi < \pi/10$ is assumed, as well as $G_{\max} |\mathbf{r}| = 20$ mT and a proton NMR sample, one gets $\tau_0 < 60$ ns. This equals a distance of roughly 10 m in a Teflon medium. In addition to cable lengths, the phase responses of the utilized amplifier and the filter should be considered when estimating the total group delay.

The feedback gain should be high enough to (1) ensure that the NMR signal drives the system into saturation instead of any poles in the response function of the feedback loop, (2) keep the transient time before the saturation short, and (3) overcome the insertion losses in the (passive) transmit-receive switch of the probe. Gain ripple over the passband should be avoided as otherwise the system can be driven into saturation by the passband noise. In this work, a ZHL-3010+ (Mini-Circuits, Brooklyn, NY) was chosen for amplification, giving a total open-loop gain of 65 dB with a 1-dB compression point of 26 dBm.

Surface acoustic wave filters offer narrow passbands with tolerable dispersion. In this work, ABFF0417 filters from Amplitronix (Costa Mesa, CA) were used for operations with ^{1}H-nucleus-based NMR probes. Transmission lines with an appropriate length were utilized to tune the phase response of the feedback loop for maximum closed-loop gain. The switching between normal receive mode and the feedback-based transmit mode was done with a ZASW-2-50DR (Mini-Circuits, Brooklyn, NY) switch, which was also used for blanking the feedback power amplifier. For controlling the timing and pulse widths of the RF switches, accurate timing control was required as well. The implementation of such hardware will be discussed later in this chapter.

In validation tests with a clinical 3-T MRI scanner (3T Signa Excite, GE Healthcare, Milwaukee, WI), it was found that no initiating RF exciter was required, because the spins pick up the correct Larmor frequency component from the noise amplified by the unstable feedback loop. After starting the monitor-

ing sequence, the system is self-maintaining and in principle infinitively long acquisition periods become available.

7.4 Multiband receiver

Modern clinical MRI systems are typically based on the heterodyne receiver scheme where the carrier (i.e., the Larmor) frequency is subtracted from the signal by an analog down-conversion [117, 132, 133]. Such receiver systems are designed for operation around a single Larmor frequency at a time. To have an independent magnetic field monitoring system, which potentially would be based on non-proton-based NMR probes, it is necessary to design and build a custom multiband MRI receiver. This section describes the design of such a receiver.

7.4.1 Digital direct-conversion-based complex signal detection

In-phase + quadrature (IQ) detection, which provides both amplitude and phase information, is necessary for receiving MR signals [40, 42]. Receiver topologies can be divided roughly into three different architectures: direct conversion, heterodyne, and image rejection [134, 135].

In the direct-conversion topology, detected signals are directly converted to zero frequency by multiplying the signals with two sine signals from a local oscillator, f_{LO}, with 90° phase difference. This topology is considered challenging to implement analogically owing to a high level of component-induced $1/f$ noise and sensitivity to mismatches in the phase and amplitude of the I and Q channels. Therefore, heterodyne receiving is generally applied for analog IQ detection, and with this architecture, the signal is converted to the center of the sampling bandwidth instead of the zero frequency. Heterodyne detection requires effective antialiasing filtering before down-conversion. These filters can be challenging to manufacture if the signal band is narrow in comparison to the carrier frequency. Image-reject architectures have emerged to counter these challenges.

The aforementioned drawbacks of direct conversion are avoided if implemented digitally, after analog-to-digital conversion, and this architecture offers the simplest approach for IQ detection. For example, Bodurka et al. have implemented the concept with success for MR data acquisitions using high-speed digitizers [132].

In this work, the digital direct-conversion schematic based on direct sampling was chosen because of its simpler implementation for multinuclear MRI

detection. A schematic of the digital direct-conversion architecture is presented in Fig. 7.4. Although some of the design challenges experienced with analog detection are avoided by performing the tasks digitally, digital signal processing (DSP) implementations present other challenges with respect to the processing speed. This is particularly the case if the DSP is performed using standard PC processors, which are not designed for high-speed parallel data processing, in comparison to application-specific integrated circuits for example.

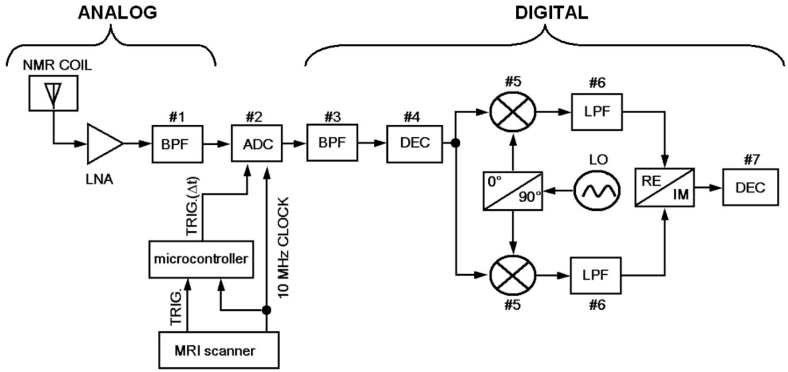

Fig. 7.4. *Block diagram for IQ detection based on the direct-sampling and digital direct-conversion topologies. The timing circuitry required for the operation is accordingly shown. TRIG and TRIG(Δt) correspond to the system "start sequence" trigger and the delayed one that is sent for the receiver. BPF, LPF, and DEC stand for band-pass filter, low-pass filter, and decimation, respectively.*

As data-acquisition duty cycles increase, the user has to deal with a similar increase in the amount of data to be processed. In MRI with conventional hardware, signal bandwidths are usually less than 1 MHz. However, certain cases exist where a significantly higher sampling rate is preferred than would be predicted by the Nyquist-Shannon theorem. This is the case if a higher sampling rate is used to compensate for relaxed filter characteristics. In this case, decimation of the redundant data points is recommended to speed up the DSP. To avoid the folding of noise on top of the signal bandwidth, filtering should be implemented before decimation (step #3 in Fig. 7.4). Finite impulse response (FIR) filters offer superior performance to analog counterparts with respect to passband and stopband characteristics [136, 137, 138]. In addition, they offer perfect linear phase response throughout the entire passband.

7.4.2 Techniques for accelerating digital signal processing

The software implementation for IQ detection should be optimized for speed to keep up with the incoming data and to avoid DSP queuing, especially for short-repetition-time acquisitions. Thus, one should minimize the number of arithmetic operations without compromising signal integrity. The following example of a multichannel MRI data acquisition illustrates the amount of incoming data and the corresponding required processing speed. The data-acquisition window is assumed to be 5 ms, and the NMR signals from an eight-element receiver coil are sampled at a rate of 10 Msamples/s into 16-bit data arrays. This translates into a required processing rate of 800 kB/TR.

The software IQ detection sets two contradicting requirements, when it comes to optimizing processing speed: (1) The signal should be decimated (step #4 in Fig. 7.4) to match the sampling rate of $2 \cdot \Delta f$ as closely as possible, thereby speeding up the subsequent mixing and following low-pass filtering owing to smaller data sets. (2) However, sharp antialiasing filters are required if a high level of decimation is performed. This in turn requires higher order FIR filters with larger number of polynomial coefficients, which can slow down the DSP significantly.

The algorithm to find optimal parameters for different filtering stages follows, with certain adaptations, the concepts of decimation filtering [136, 139, 140]. The requirement for the analog low-pass filter before sampling can be relaxed by increasing the sampling rate, or vice versa, the sampling rate of the digitizer is determined by the steepness of the analog filter. For speeding up the DSP, the sampling rate should be as low as possible of course. The first digital filter size is kept minimal while preventing any increase in noise level through aliasing during decimation of the data set (step #3 in Fig. 7.4). The digital low-pass filter after down-mixing (step #6 in Fig. 7.4) can have a higher filter order, since the data set size is smaller. Figure 7.5 illustrates the implemented DSP process in the frequency domain. To calculate the right balance between the decimation filtering and low-pass filtering, the time that it takes to perform different arithmetic operations must be known.

Thus, the DSP algorithm should be characterized with respect to processing speed when performing the convolution filtering and the rest of the IQ detection. Direct convolution is preferred to fast-Fourier-transform-based frequency domain filtering because of its higher speed in this application. This statement holds true as long as the number of FIR filter coefficients M is small compared to the sample size N. With direct convolution, the processing time $\propto N \cdot M$. If filtering is performed in the frequency domain, then the processing time $\propto 2 \cdot N \cdot \log_2(N) + M \cdot \log_2(M) + N$. The arithmetic operations for addition

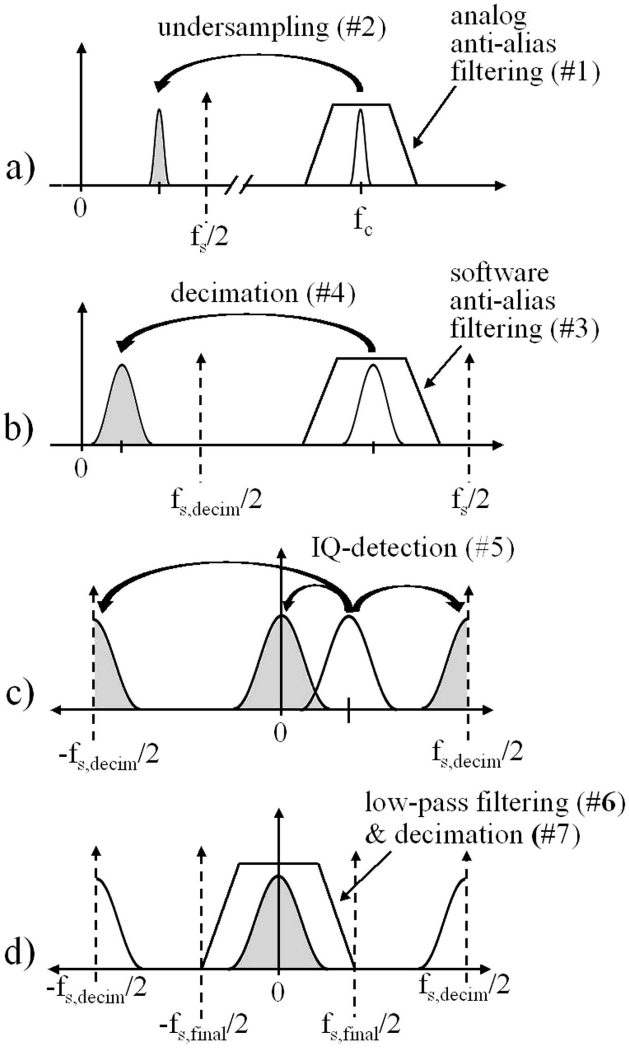

Fig. 7.5. *Illustration of the relevant DSP steps and how the signal is converted from the physical quantity to the complex data set, centered at zero frequency, through decimation, filtering, and down-conversion. The numbers #1-#7 refer to corresponding DSP steps presented in Fig. 7.4.*

and multiplication are assumed to require the same amount of processor time [138]. The first term of the frequency domain approach comes from the forward and reverse fast Fourier transform (FFT) operations. The next term is the FFT of the filter elements, and the last one describes the multiplication process in the frequency domain.

It should be noted that one can combine decimation with the filtering process in the frequency domain. This corresponds to chopping of the Fourier-transformed array at the right locations. As a drawback, an algorithm to maintain synchronization in the time domain would need to be developed. Nonetheless, this approach can only halve the total filtering time at best. Therefore, it was considered in this work to be more optimal to proceed with the direct convolution method for the filtering.

The above considerations for time-efficient DSP can be summarized into the following five-step procedure (cf. Figs. 7.4 and 7.5): (1) Possible decimation factors with respective folded frequency bands were sought, and it was ensured that no folding of the frequency band on top of itself occurs. (2) For the software antialiasing filter (step #3 in Fig. 7.4), the transition band length was determined by how far the aliased signal will end up from the spectrum edges (i.e., DC and $f_{s,decim.}/2$, where $f_{s,decim.}$ is the decimated sampling rate). The shortest of the distances dictates the maximum filter transition band length. For the low-pass filters of the IQ detection, the transition band should be steep enough so that the noise will not alias after the final decimation to $f_s \sim 2 \cdot BW$. (3) The Parks-McClellan method for FIR filter design was applied [137, 138]. The minimum number for the filter elements, N, with passband f_{pass} and stopband f_{stop} ripple characteristics δ_p and δ_s, respectively, can be determined according to

$$N = \frac{K_1 - K_2 \cdot \delta f^2}{\delta f} + 1, \tag{7.8}$$

with

$$\begin{aligned} K_1 = {} & [0.005309 \cdot (\log \delta_p)^2 + 0.07114 \cdot \log \delta_p - 0.4761] \cdot \log \delta_s \\ & - [0.00266 \cdot (\log \delta_p)^2 + 0.5941 \cdot \log \delta_p - 0.42781], \end{aligned} \tag{7.9}$$

$$K_2 = 0.51244 \cdot (\log \delta_p - \log \delta_s) + 11.012, \tag{7.10}$$

and

$$\delta f = (f_{stop} - f_{pass})/f_s. \tag{7.11}$$

(4) Based on the calculations with respect to corresponding decimation rate and filter element sizes, an estimate of the total time required for performing the IQ

detection was made. (5) The fastest combination was chosen, and respective FIR filter coefficients were calculated.

7.4.3 Multiband receiver implementation

The described direct-sampling, direct-conversion receiver architecture was implemented for an eight-channel MR receiver system. Four two-channel PXIe-5122 high-speed digitizers were mounted into a PXI-1065 chassis (National Instruments, Austin, TX). The 14-bit PXIe-5122 boards had a sampling clock of 100 MHz and 8 MB/channel on-board memory. Spectral noise density was measured to be 19 $\mathrm{nV}_{rms}/\sqrt{\mathrm{Hz}}$ at 140 mV_{rms} maximum amplitude level at a sampling rate of 10 MHz and with a 50 Ω termination plugged into the input. The folding of the noise floor could be reduced by increasing the sampling rate, which brings an improvement of $\sqrt{K}$, where K is the ratio of how much the sampling rate is increased. The noise from the 50 Ω termination had no significant effect on the measurement. For the root-mean-square value of the quantization noise v_q, one can derive [141]

$$v_q = \frac{\mathrm{LSB}}{\sqrt{12}}, \tag{7.12}$$

where LSB stands for the least significant bit. If the noise is assumed to be white, the quantization noise becomes 1.14 $\mathrm{nV}_{rms}/\sqrt{\mathrm{Hz}}$ at 70 mV_{rms} maximum input level and at 10 MHz sampling rate. Thus, it can be concluded that the dominant noise of the digitizers is not the quantization noise but rather other undefined intrinsic noise sources. At a 10-MHz sampling rate, and at a 140-mV_{rms} input range, the 19 $\mathrm{nV}_{rms}/\sqrt{\mathrm{Hz}}$ noise level observed would reflect to an effective dynamic range of $17 \times 10^6\sqrt{\mathrm{Hz}}$, thus fulfilling the estimated requirement of 90 dB at 50 kHz.

The phase noise of the digitizers was estimated. It was assumed that the signal (or corresponding aliased signal through the undersampling) was at least 10 kHz away from the spectral edges, and thus clock-jitter-induced phase noise could be assumed to be white noise. The spectral noise density was given by the manufacturer as <-130 dBc/Hz at 10-kHz offset. For example, an ^{1}H NMR signal in a 3-T background field will fold around 2.7 MHz when sampled at 10 MHz. With the given spectral noise density, this corresponded to a jitter of 27 ps, or an uncertainty of <0.46 mrad in the detected phase value [142]. For magnetic field monitoring, this value fulfilled well the estimated requirement of 40 ns (cf. Chapter 3).

The digitizers had a built-in antialiasing filter with a -3 dB point at 110 MHz and a slope of approximately -33 dB/decade. Owing to modest slope of the

antialiasing filter, the narrow-bandwidth MR signals were not expected to suffer from high signal-band ripple even beyond the −3 dB point of the antialiasing filter. Thus, an ^{1}H NMR signal at a 3-T main magnetic field flux density (127.7 MHz) could be measured without significant signal distortions.

The PC-based PXI-8130 controller included a 2.3-GHz dual-core Turion 64 X2 processor (AMD, Sunnyvale, CA) with 1-GB DIMM dual-channel 667-MHz DDR2 random access memory (RAM). The data that were acquired on the digitizer boards should be fetched in a rapid pace before the on-board 4 Msamples/channel memory runs out. Figure 7.6 illustrates the data flow with respect to relevant system blocks. High-speed PCI-express buses, capable of data transfer rates of up to 4 GB/s, were implemented to transfer the measurement data to the 1-GB RAM of the controller. The 4 GB/s speed was well beyond the maximum digitizing speed of the considered eight-channel configuration. The data fetched into the RAM were streamed into a binary file on the local hard drive before overflowing the RAM. A rate of 600 MB/s into a RAID drive was given by the manufacturer. In this particular case with a 60-GB serial ATA hard drive in use, the writing speed was characterized to be 37 MB/s. It should be noted that no special considerations (e.g., turning off the virus protection or firewall) were made to further speed up the system performance. This consideration remains valid also with all the results presented hereafter.

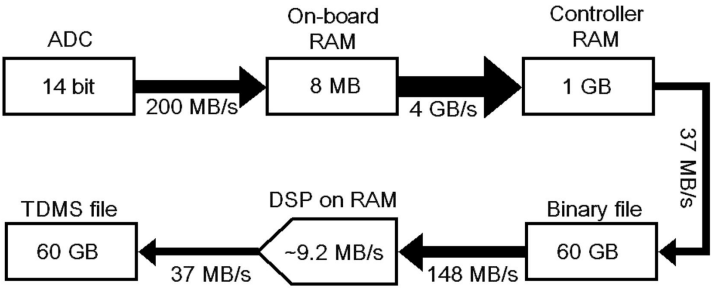

Fig. 7.6. *Flow chart of the data-processing steps from acquiring the signal to writing the final processed data onto a hard drive. The thickness of the arrows indicates the bottlenecks with respect to data flow. In this particular implementation, the TDMS file format from National Instruments was chosen.*

The 1-GB RAM acted as a buffer, decreasing the chance that writing to the binary file becomes the bottleneck process. In MRI experiments, the delay be-

tween each repetition often gives enough time to transfer the data from the RAM before exceeding its capacity. In total, with an eight-channel configuration and without an RF front-end the accumulated cost per channel was ∼$5 000.

The IQ-detection scheme was implemented in LabVIEW (National Instruments, Austin, TX) running under a Windows XP operating system (Microsoft, Redmond, WA). The data-acquisition process and the DSP were performed in parallel. The only exception to this was writing and reading to binary files, where the writing had priority. The designed approach took advantage of the wait time between each repetition that is available for most MRI sequences. The processed data were stored in National Instruments specific ".TDMS" file format, which is specially designed for handling large data sets.

With the homemade receiver, the clock-jitter-related <0.46 mrad phase uncertainty fulfilled the precision requirement of 0.1 rad (cf. Chapter 3) as long as the signal spectrum was down-converted at least 10 kHz away from the spectral edges. The achievable dynamic range of $3.7 \times 10^6 \sqrt{\text{Hz}}$ was approximately an order of magnitude higher than the highest expected SNR levels from NMR probes.

7.5 RF front-end

An RF front-end was constructed for the NMR probes to ensure proper signal conditioning before digitizing. This required amplification to match the dynamic range of the receiver, as well as band-pass filtering to avoid aliasing during sampling. No MRI compatibility was required of the components since they could be placed far enough from the magnet bore.

An amplification of 15-35 dB was implemented after the first gain stage at the NMR probe. Based on Frii's formula (cf. Eq. 6.17), the noise figure requirements for the second-stage amplifiers are relaxed and various wideband receivers are available from commercial vendors (e.g., ZFL-1000LN+, Mini-Circuits, Brooklyn, NY). The fine adjustment of the amplification was performed with manually adjustable attenuators.

NMR-nuclei-specific band-pass antialiasing filtering was preferred over wideband ones to keep the required sampling rates low, i.e., DSP times short. Commercially available surface acoustic wave filters offer narrower bandwidths (∼1 MHz) at relevant NMR frequencies in comparison to typical reactive-element-based filters. When long DSP times are of no concern, the maximum sampling rate of PXIe-5122 digitizers in combination with the in-build low-pass filters could be utilized to omit the filtering in the RF front-ends for Larmor frequencies below 100 MHz.

7.6 Timing and synchronization

Microcontroller-based circuitry was implemented for the pulse width and the timing control of RF excitations, as well as for synchronizing the field monitoring acquisitions with respect to MRI sequences (cf. Figs. 7.1 and 7.4). In this work, a state machine based on a 16-bit ATmega16 microcontroller (Atmel, San Jose, CA) was designed to receive the triggering pulses from the MRI scanner. A delay of arbitrary length could be applied to the trigger signals with a time resolution of $1/f_{clock}$, where f_{clock} stands for the frequency of the clock signal of the microcontroller.

The 10-MHz master clock of the MRI scanner was utilized to clock the microcontroller in a synchronized manner. With the in-build voltage controlled oscillator of ATmega16 microcontrollers, the setup resulted in synchronization on the order of $\sim$1 ns and a timing resolution of 100 ns. Thus, it was concluded that the achievable synchronization and the resolution characteristics fulfilled the requirements for transmit pulses, as well as for timing data acquisitions ($<$40 ns, cf. Chapter 3).

The scanner's 10-MHz master clock was also routed to the high-speed digitizers to synchronize their sampling clocks, i.e., to avoid any drift-related errors in the measurement data. Here, it should be noted that the master clock and the trigger signals were readily provided by the outputs of clinical MRI scanners, and therefore no hardware alterations on the MRI system side were required.

7.7 Validation of the receiver for MRI acquisitions and multiband detection

Based on the performance characteristics, the developed receiver system could be utilized for MRI acquisitions as well. To validate this, a clinical transmit-receive birdcage head coil was connected to one of the ^{1}H channels of the homemade receiver and a gradient echo image of a resolution phantom was acquired. For comparison, the same image was acquired with a clinical MRI system (3T Signa Excite, GE Healthcare, Milwaukee, WI). Similar image qualities could be observed, as is shown in Fig. 7.7, and a quantitative SNR comparison resulted in values of 61.5 dB for the standard MRI receiver and 60.3 dB for the homemade one. In the homemade receiver, the dynamic range at the applied 9.09-MHz sampling rate was 61.8 dB, thus requiring careful adjustment of the receiver gain. It was therefore assumed that the 1.2-dB difference in the measured SNRs was due to a slight signal saturation with the homemade receiver. For further details and characteristics of the developed receiver, reference [119] is recommended.

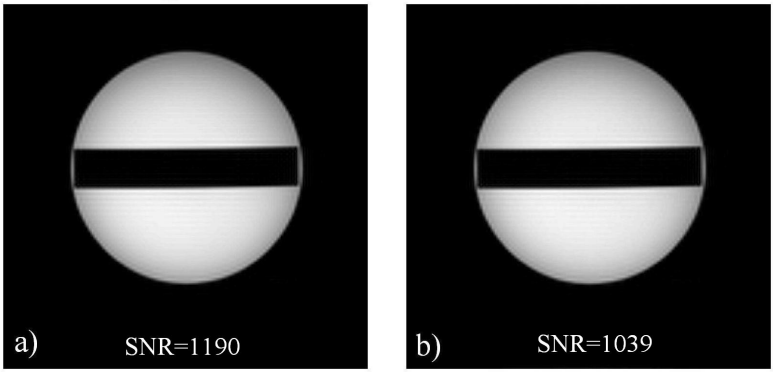

Fig. 7.7. *Two ^{1}H spoiled gradient echo images of a resolution phantom, acquired (a) with the standard receiver of a 3-T Signa Excite MRI scanner (GE Healthcare, Milwaukee, WI) and (b) with the homemade receiver. The applied imaging parameters were as follows: resolution = 128 × 128 pixels, field of view = 180 × 180 mm, slice thickness = 10 mm, bandwidth = ±15.6 kHz, echo time = 10 ms, repetition time = 500 ms, and number of excitations (NEX) = 1. Here, phase-locking on the homemade receiver was performed by using one ^{1}H RF channel of the homemade receiver to monitor the phase of the MRI system local oscillator.*

One benefit of a digital direct-sampling topology is that it can be utilized for detecting multiple signals with nonoverlapping frequency domain with a single receiver channel. To test this concept of multiband detection with the developed receiver, three signals at different frequency bands were analogically combined. The output of the combined signals was subsequently fed into a single acquisition channel of the receiver system. The detected signals were the following: (1) a generic electrocardiogram (ECG) signal mimicking the heart beat of a mouse at a rate of 600 beats per minute, generated with a commercial signal generator (Agilent Technologies, Santa Clara, CA), in which the spectrum of the ECG signal was safely assumed to be below 500 kHz; (2) the FID signal of an ^{2}H probe in a 3.0-T background field, corresponding to a Larmor frequency of 19.6 MHz; and (3) the output of an ^{1}H RF local oscillator, operating at 129.5 MHz. In the combiner, the different signal sources were conditioned by appropriate analog low-pass (ECG signal), band-pass (^{2}H FID signal), and high-pass (^{1}H RF local oscillator signal) filters. After the ADC, the signal bands were separated by using appropriate digital multi-band-pass filtering before applying IQ detection individually for each signal. No loss in SNR nor band-to-band cross-talk was

observed in the resulting three individual data sets, demonstrating the feasibility of simultaneous detection of multiple, nonoverlapping RF signals (cf. Fig. 7.8).

7.8 Discussion and conclusions

In this chapter, fundamentals for designing and constructing a multiband transmit-receiver for operating NMR probes were given. One benefit of a separate transmitter is that it ensures optimal flip angles for the maximum SNR, independent of applied pulse sequences. The implemented 5-W transmitter provided RF excitations in a cost-effective way for four to eight NMR probes. Moderate, $\sim$100-kHz excitation bandwidths for proton samples were ensured by generating short hard pulses with high-speed RF switches. For different NMR nuclei, the transmit chain was easily modified by changing the passband of a passive unblanking switch.

By utilizing a specialized feedback network for RF excitation pulses, one ensures that the RF pulses have high power levels but are also coherent with the spin ensemble. This novel technique ensures high signal levels with the coherent, short-interval excitations-based operating scheme, as well as with the standard, long-interval excitations-based operating scheme when having acquisitions with short repetition times (TR $<$ T1). This technique is seen as compulsory for making NMR-based magnetometers insensitive to MRI parameters such as resolution, repetition time, and strength of velocity-encoding lobes.

With a separate receiver, the utilization of the field monitoring system is not constrained to only multichannel MRI systems, nor is one forced to use relatively expensive, high-dynamic-range MRI receiver channels for magnetic field monitoring. In addition, the system enables the utilization of non-proton-based NMR probes. The developed receiver design requires only minor adjustments, i.e., switching of the antialias filters, when changing nuclei or background magnetic field strength.

A timing controller was constructed to adjust transmission pulse widths, to prevent RF excitations occurring during very high gradient pulses, e.g., crusher gradients, and to adjust the time window of data acquisitions. The developed microcontroller-based state machine was easily interfaced with a clinical MRI scanner for parallel operations based on readily available clock and trigger outputs from the scanner. Hence, no system hardware changes for this aspect were required.

The developed MR receiver was shown to also be applicable for MRI applications with a comparable performance to a standard clinical MRI scanner. To phase lock the software local oscillator of the homemade receiver, one of the

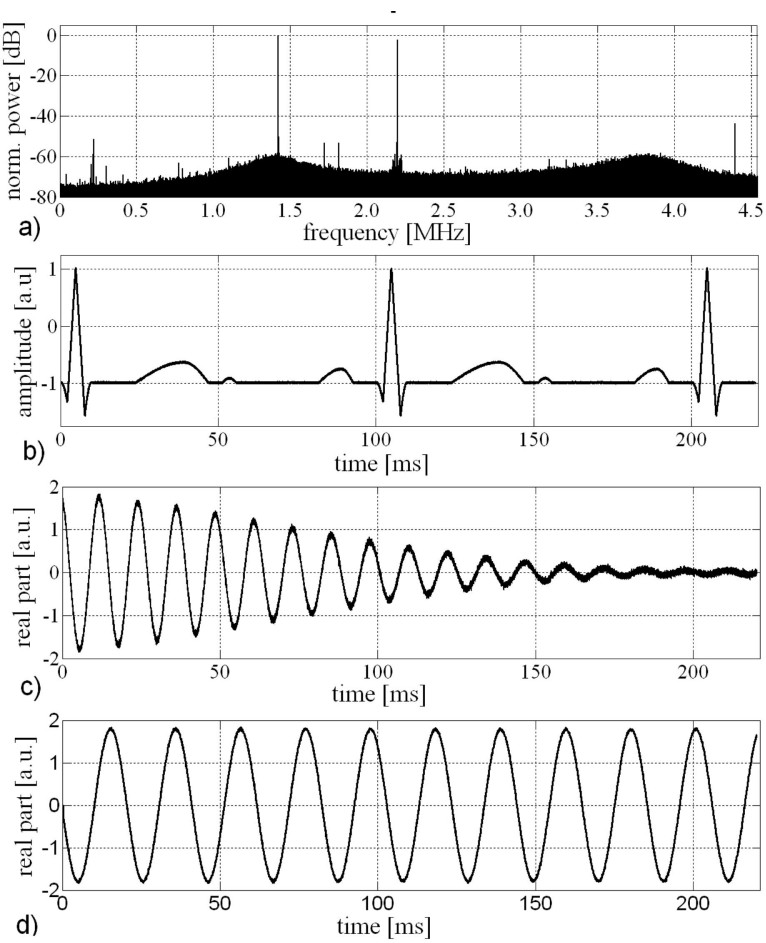

Fig. 7.8. *Illustration of data sets that were received during a single-channel multiband acquisition. The combined signals of the ECG, the ^2H FID, and the 1^1H RF local oscillator were separated during signal processing to individual signals by appropriate filtering. (a) With a 9.09-MHz sampling rate, the ^2H signal at 19.6 MHz was folded to 1.42 MHz and that at 129.5 MHz was folded to 2.20 MHz, respectively. Owing to the relatively wide band separation, the band-to-band interference was easily filtered below the noise level. With (b) the ECG signal, no division into the I and Q modes was done, as was the case with (c) the ^2H NMR and (d) the ^1H RF LO signals.*

receiver's RF channel was utilized to measure the output of the MRI system's local oscillator.

With the utilized direct-conversion receiver topology, an intriguing option becomes possible: utilizing a single receiver channel to measure multiple frequency bands simultaneously. This was proven in practice by measuring ^{1}H local oscillator, ^{2}H NMR probe, and simulated ECG signals without observable band-to-band cross-talk or loss in SNR. This technique allows, for example, cost savings in manufacturing MRI systems since the number of required RF channels can be reduced. To implement this option, frequency-domain multiplexing of multiple MRI signals is required to spread the signals to different frequency bands [143].

8

Susceptibility-Matched NMR Probes for High Intrinsic Magnetic Field Homogeneity

The strict requirement for field homogeneity over an NMR sample has been briefly discussed in Chapter 6 in the context of the standard, long-interval excitations-based monitoring scheme. In this chapter, the relevant relations between field inhomogeneity and material susceptibility differences in NMR probe constructs are introduced. For designing standard, long-interval excitations-based NMR probes, different techniques to improve field homogeneity across the NMR sample are also presented. Many of these methods require an accurate control of material susceptibility; it will be shown that a clinical MRI scanner can also be utilized for accurate susceptometric measurements.

8.1 Susceptibility mismatch and magnetic field inhomogeneity

Static magnetic field patterns across NMR samples in the presence of susceptibility mismatches is studied with the help of magnetic scalar potential $\phi_m(\mathbf{r})$. Because no magnetic charges exist, the scalar potential obeys the Laplace equation

$$\nabla^2 \phi_m(\mathbf{r}) = 0. \tag{8.1}$$

If a long cylinder is placed inside a homogeneous magnetic field, the flux density inside the cylinder can be shown to be constant [53], and

$$\mathbf{B} = \frac{1+\chi_0}{1+\chi/2+\chi_0/2} B_0 \hat{z}, \tag{8.2}$$

where χ_0 is the susceptibility of the ambient medium and χ is the homogeneous susceptibility of the cylinder. Similar outcomes of a homogeneous field can also

be concluded to occur inside an ellipsoid and inside the innermost cylinder of a coaxial geometry of materials with different susceptibility values [53, 144]. This property can be effectively utilized in probe constructs, whereby choosing the right probe geometry field inhomogeneities across the NMR sample volume can be reduced.

The definition of a long cylinder is dependent on the cylinder diameter, the difference in susceptibility from that of ambient medium, and how tolerable significant inhomogeneities are. Numerical analysis has been conducted to model the level of field perturbations caused by the ends of the cylinder. The scattering fields inside and outside of a 30-mm-long cylinder with a 10-mm diameter are shown in Fig. 8.1. Here, the susceptibility difference is set to $\Delta\chi = -10$ ppm, thus approximately matching the air-water difference. Simulations were performed with "Maxwell 3D" software (Ansys, Canonsburg, PA). Figure 8.1a shows that the magnetic flux density outside the cylinder forms a dipole-shaped pattern as predicted by the analytical solution of Eq. 8.1 [53] given as

$$\Delta B_z(z,x) = \frac{\Delta\chi B_0 a^2}{2} \frac{z^2 - x^2}{(x^2+z^2)^2}. \tag{8.3}$$

Here, B_0 is assumed to point toward the z direction.

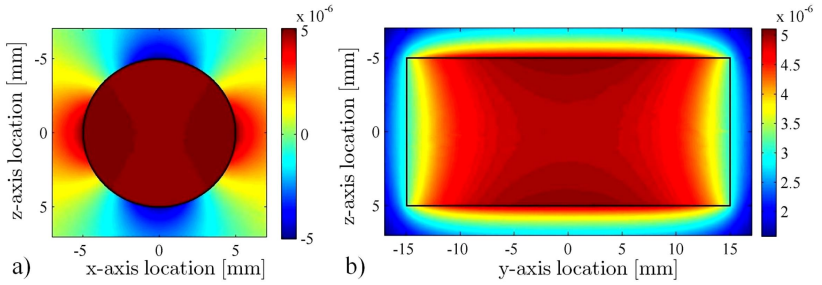

Fig. 8.1. *Relative magnetic field patterns inside and outside of a nonconductive cylinder with a −10 ppm susceptibility difference from that of the ambient medium. Here, the background field is pointing toward the z axis, and the cylinder boundaries are highlighted with black lines. (a) In an axial slice taken at the center of the cylinder, one sees the dipole-shaped pattern outside of the cylinder and a constant field inside. (b) Along the symmetry axis of the cylinder, i.e., the y axis, the level of field homogeneity increases toward the center of the cylinder.*

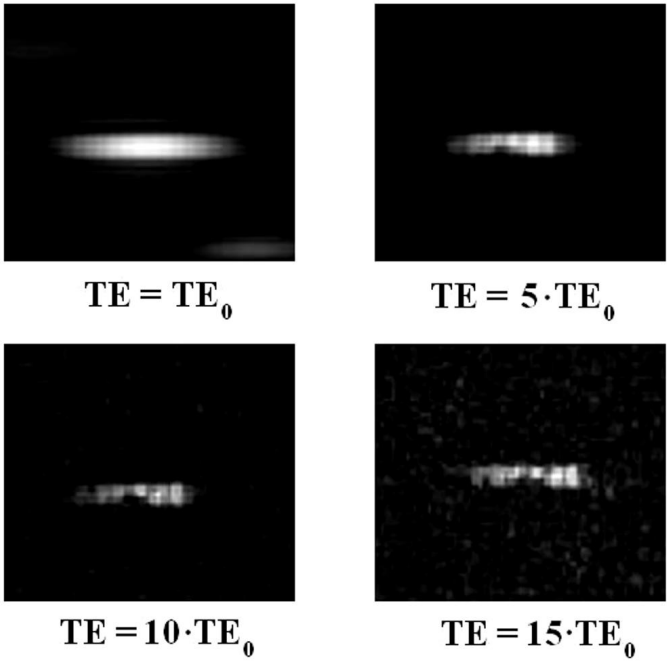

Fig. 8.2. *Gradient-echo-based MR images of a water-filled capillary with an inner diameter of 1.5 mm and a copper coil wound around it. (The image resolution is set to 0.16 × 0.32 mm with a slice thickness of 1.3 mm.) Stripe-shaped inhomogeneities arise at longer echo times, indicating a susceptibility mismatch between the copper solenoid and the ambient medium. In the middle of the sample, one can also see an impurity-related artifact. In all the figures, the contrast is adjusted to match the average SNR.*

A solenoid coil wound around an NMR sample can potentially distort the magnetic field homogeneity over the sample. For example, this can be seen as darker stripes in the high-resolution MRI images in Fig. 8.2.

The relation between the coil susceptibility mismatches (and hence the consequent field perturbations) and the level of signal dephasing was further studied in the case of ^{1}H probes. The outcome of such simulations is shown in Fig. 8.3. Here, a cross-sectional cut of a solenoid coil, which was made out of 300-μm copper wire, was taken along the direction of the background field. At ppm-range susceptibility differences, second-order field perturbations can be omitted, and thus the total effect of the coil susceptibility mismatch was estimated by sum-

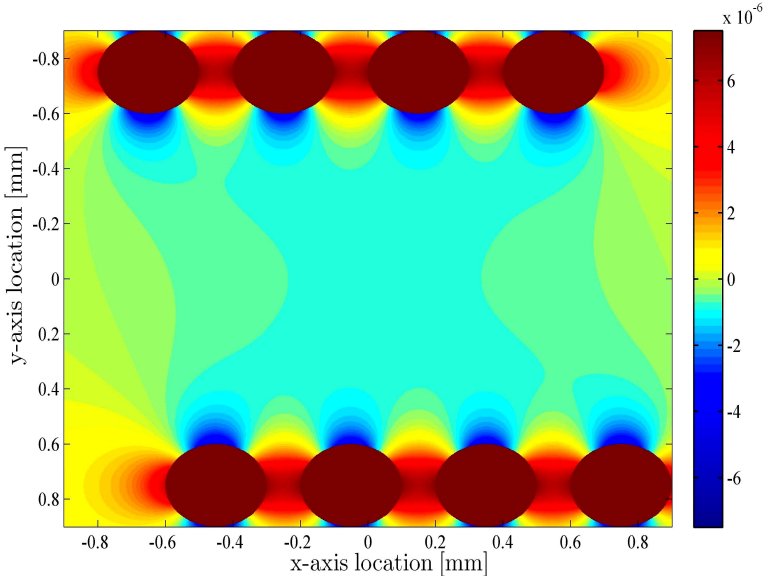

Fig. 8.3. *Simulations of magnetic field inhomogeneities emerging as a result of a susceptibility mismatch between a copper coil and air. Here, a relative scale is used with respect to the background field, which is pointing in the z direction.*

ming the effects of the differential cross sections of the wire (cf. Eq. 8.3), and the signal dephasing was calculated based on Eq. 6.14. The corresponding signal dephasing is presented with four different susceptibility difference values in Fig. 8.4. Although the analysis is approximate in nature, the results suggested that the susceptibility difference between the copper and the ambient medium should be reduced below 1 ppm to ensure sufficiently high signal levels even throughout the longest MRI trajectories (between 100 and 150 ms).

It should be noted here that, for nonproton samples, the requirement for susceptibility matching is relaxed by the ratio γ_X/γ_{1_H}. The level of field inhomogeneities can be suppressed also by reducing the wire diameter or by winding the coil further away from the sample. However, both of these methods have negative effects on SNR, and therefore these techniques are not desired.

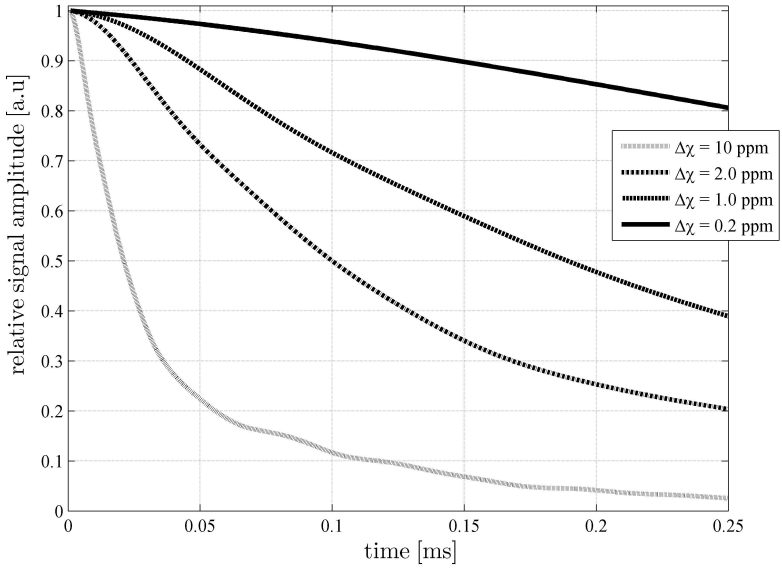

Fig. 8.4. *If an NMR sample is placed inside the coil shown in Fig. 8.3, the signal dephases prematurely as a result of the susceptibility-mismatch-related field inhomogeneities. A two-dimensional case was considered, with a 1 × 1 mm sample that was placed in the middle of the coil, and four different susceptibility-mismatch values between the coil and the ambient medium were studied. The effect of the susceptibility difference between the sample and the ambient medium was omitted from the simulations since this was not considered to be relevant based on Eq. 8.2.*

8.2 Susceptibility matching: probe casing

To ensure long read-out times with NMR probes operated with the standard, long-interval excitation-based scheme, different susceptibility-matching techniques for NMR microprobes have been developed [55, 56, 118, 145]. Ideally, all the materials utilized in the probe constructs would have their susceptibility values close enough to the value of the ambient medium. In reality, such a requirement is difficult to fulfill, and, for example, no substitute for a copper wire can be found, apart from specially made metal alloys, which would inherently have high conductivity and a susceptibility difference smaller than 1 ppm from that of air. An alternative method to reduce the RF-coil-induced field inhomogeneities is to utilize a cast surrounding the solenoid coil that can be manufactured with a matching susceptibility value to that of copper. If such a casing has

a geometry of a cylinder, or an ellipsoid, the susceptibility difference from that of air is of no concern, as was explained in the previous section (cf. Eq. 8.2).

A challenge with such a susceptibility-matching technique is to find casing materials of the right properties. Along with the matching susceptibility, the material should be formed seamlessly over the coil and the sample to ensure that there were no (air) voids to deteriorate the field homogeneity. To prevent noise and undesired signal coupling, the material should be nonconductive and free of the nuclei upon which MRI acquisitions and NMR probes are based. In solids, nuclei are strongly coupled to the surrounding lattice structure, which consequently leads to very short T2* values [43]. Therefore, certain solids can be utilized for susceptibility matching despite the possibility of their containing the same nuclei as NMR probes or imaging objects, e.g., plastics.

One potential ^{1}H-free material that is suitable for susceptibility matching is perfluorinated hydrocarbon FC-43, also known as Fluorinert (M3, St. Paul, MN) [56]. The susceptibility of FC-43 is still relatively far from the value of copper (i.e., 1.4 ppm [56]), which leads only to a moderate level of susceptibility matching. Furthermore, the use of fluids such as FC-43 requires a liquid-proof casing around the probe, which complicates the probe manufacturing processes and makes the probe construction more fragile. For improved robustness, solid enclosures, for example, out of epoxy, are proposed. Epoxy is a diamagnetic material with a susceptibility between -9 and -12 ppm [34, 55] and, therefore, its susceptibility can be increased to match the value of a less diamagnetic material (hence water or copper) by introducing small amounts of a paramagnetic dopant.

Doping two-component epoxy with a third compound requires a careful assessment of the materials that are used. The challenge is to have a highly paramagnetic material that is soluble in either epoxy resin (i.e., in epoxide molecules) or hardener (i.e., in amine molecules), yet not reacting with these components and hence interfering with the normal epoxy-forming reaction. High molar susceptibility is also required for the candidate dopant since the solubility to epoxy is estimated to be limited. In MRI, paramagnetic ions are typically utilized for adjusting the T1, T2, and susceptiblity values of water-based samples. Amines are especially chemically strongly reactive and introducing (highly paramagnetic) salts into a curing process of epoxy would lead to unwanted reactions between the salt ions and the amines.

The challenge of doping epoxy can be tackled by utilizing certain hydrocarbon molecules, e.g., monomers, into which highly paramagnetic ions are firmly bonded. The paramagnetic ions could, for example, be dysprosium, erbium, gadolinium, iron, manganese, or nickel-based ions [53, 54]. Such monomer-based molecules are chemically nonreactive with the epoxy components, are soluble at the desired quantities, and have a molar susceptibility on the or-

der of 0.1-1 cm^3/mol. For example, erbium(III) tris(2,2,6,6-tetramethyl-3,5-heptanedionate) is one such molecule and is readily available from commercial vendors.

8.3 Susceptibility matching: sample plugs

Gradient-related dephasing restricts the sizes of NMR probe samples, especially with the standard, long-interval excitations-based operating scheme. Reduced sample sizes, however, increase the sensitivity of the susceptibility matching. Several ways exist to constrain the sample dimensions in the direction of the coil longitudinal axis, while not compromising the high field homogeneity. Three such plausible designs are illustrated in Fig. 8.5.

One possibility is to utilize non-^{1}H-based liquid plugs to restrict the sample size inside a glass capillary (cf. Fig. 8.5a). By using cyclohexane as a sample, and paramagnetically doped heavy water droplets as liquid plugs, one also ensures a preferred convex-shaped sample volume owing to the higher surface tension of heavy water [118]. If water-based samples are desired, for example, for the ease of adjusting sample T1 and T2 values, solid plugs can be utilized instead. These plugs can be made out of susceptibility-matched epoxy for example.

It is possible to omit the sample capillary and to manufacture the sample holder completely out of susceptibility-matched epoxy [145] (cf. Fig. 8.5b). Here, a water droplet is sealed inside the holder by dedicated epoxy plugs that have their susceptibility value matched to that of water. The RF coil and the sample void are cast directly into the sample holder during the manufacturing process. Because no capillaries are required with this design, the coil can be placed closer to the sample for higher sensitivity. The drawback of this technique is that the susceptibility matching becomes more demanding. This is further illustrated in Fig. 8.6.

A solenoid coil has a relatively sharp sensitivity drop-off along the coil's symmetry axis, as was shown in Fig. 6.6. This nonhomogeneous sensitivity profile can be utilized to eliminate the need physical plugs (cf. Fig. 8.5c). The feasibility of this probe design was further studied with simulations, where the spatial sensitivity profile of a solenoid (Eq. 6.18) and the gradient envelopes for imaging (Eq. 2.13) were introduced to the NMR signal equation (Eq. 6.14). The sample diameter was chosen to be 0.9 mm. Figure 8.7 illustrates the achievable signal levels after image encoding for various coil geometries. Although ^{1}H NMR probes were studied here, the analysis can be projected to NMR probes that are based on other nuclei by changing the value for the gyromagnetic ratio

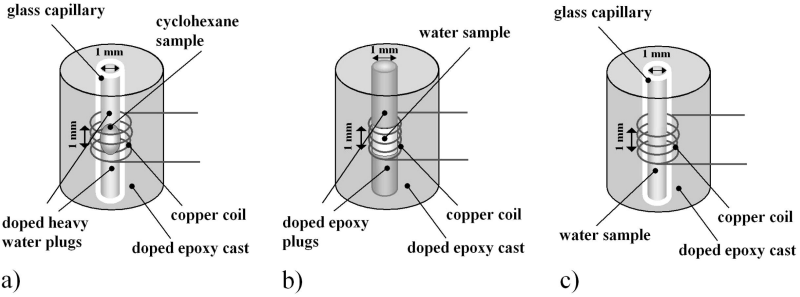

Fig. 8.5. *Illustrations of three susceptibility-matched NMR probe designs where in all cases a copper coil is cast inside an epoxy cylinder with matched susceptibility to copper. The dimensions are given based on the assumption that* ^{1}*H nuclei are chosen for the NMR signal source. In case (a), a cyclohexane droplet instead of a water sample is restricted by two heavy water droplets to ensure a convex NMR sample shape [118]. In case (b), the capillary is omitted, which increases the coil sensitivity. Here, the space for a water droplet is created during the curing phase of the epoxy with a dedicated mold. After the insertion of the NMR sample, the sample space is sealed by two epoxy plugs matched to the susceptibility of the sample. In case (c), the spatially selective sensitivity of a solenoid coil is utilized, and the use of physical plugs becomes obsolete.*

accordingly. It should also be noted here that the proposed design is only applicable for the standard, long-interval excitations-based operation scheme with the assumption that TR $>$ T1. Otherwise, an emerging steady-state transverse magnetization can lead to a different signal profile, as would be expected from Fig. 6.6.

The conducted simulations showed that the sensitivity drop-off of the receive-only probe's coil did not match that of the physical plugs with respect to spatial selectivity. Consequently, such probes would be applicable to MRI acquisitions with approximately double the resolution that would be achievable with probes based on physically constrained sample spaces. An interesting observation can be made from Fig. 8.7a, however: Although the number of turns, i.e., the coil length, was increased, the applicable imaging resolutions did not suffer dramatically. This was estimated to be because the coils with higher number of turns have a steeper drop-off in the sensitivity profile.

If NMR probes are operated in a transmit-receive configuration, the sensitivity drop-off is expected to become steeper in comparison to the receive-only case. This is because the spins that are at the locations of lower sensitivity also experience flip angles smaller than the desired 90° (cf. Eq. 7.3). Simula-

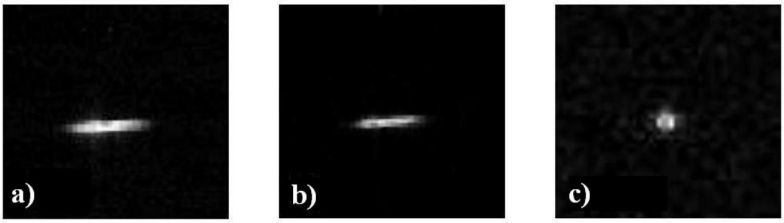

Fig. 8.6. *High-resolution gradient echo MR images of three water-filled NMR probes in a sample volume with an inhomogeneous magnetic field. (a) The presence of a local impurity is observed as a faster signal decay in the center of the image. Here, the T2* value of the sample is measured to be 62 ms. Difficulties using MR images for determining the B_0 inhomogeneity in small sample volumes include relatively large pixel sizes and the spreading of the signal from a single pixel to neighboring ones. This is illustrated in image (b), where a T2* value of 122 ms is achieved despite the visually observable signal inhomogeneity. (c) After inserting epoxy plugs into the capillary to limit the sample length to 1 mm, the T2* value of the signal drops to 30 ms. In addition to possible impurities, the susceptibility matching of the epoxy plugs is estimated to be nonideal in this particular case.*

tion results for the relation between SNR and achievable image resolution in the context of transmit-receive probes are shown in Fig. 8.7b. In comparison to receive-only NMR probes, it was observed that noticeable signal dephasing starts to occur at smaller voxel dimensions. This indicates a steeper drop-off in the spatial sensitivity. However, it was also observed that the achievable baseline signal levels were reduced with transmit-receive probes. This was because fewer sample voxels experienced the desired field strength for the 90° flip angle in this case. Hence from the reduced baseline SNR, it was concluded that only a marginal improvement in applicable image resolutions could be achieved.

In Fig. 8.7b, the excitation pulses were chosen to ensure 90° excitations at the center of the coil. It was further studied whether 90° was the most optimal flip angle also with the probe design where the sample volume is constrained by the solenoid's nonhomogeneous sensitivity profile. Simulated signal levels with respect to different imaging resolutions and applied flip angles are shown in Fig. 8.8. In the simulations, a coil geometry was chosen with five closely wound turns, 1.6-mm coil diameter, and 0.3-mm wire diameter. The filling factor was 56%. These values matched a realistic ^{1}H NMR probe geometry for magnetic field monitoring.

From Fig. 8.8, it was seen that the maximum SNR was achieved by an RF pulse that corresponded to a flip angle of 100° in the center of the solenoid.

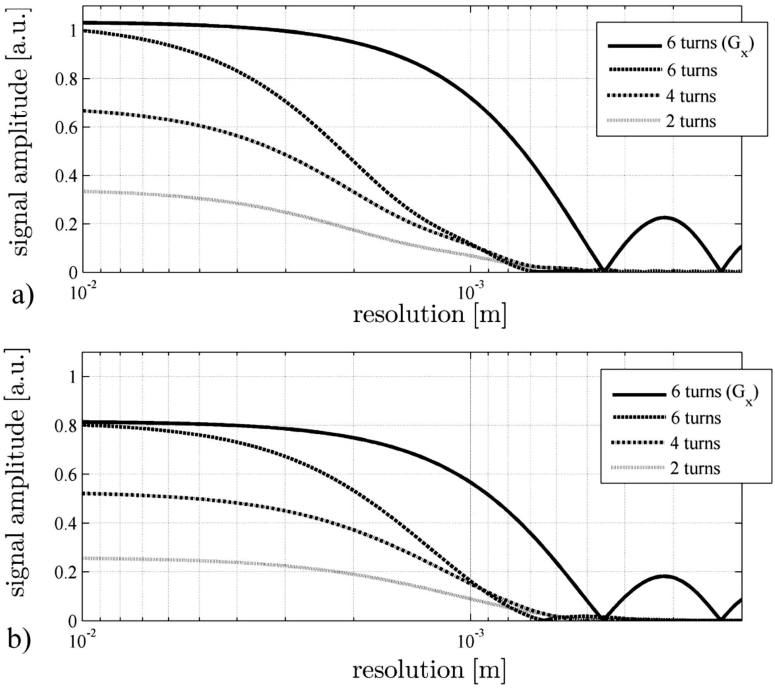

Fig. 8.7. *Signal levels after image encoding of* ^1H *NMR probes with an unsealed sample space along the capillary symmetry axis. The signal amplitudes are given as a function of the encoding gradient envelopes corresponding to the respective* ^1H *image resolutions. Two cases were separated: (a) the probes were relaying on the system excitations or (b) the probes were utilized in the transmit-receive configuration. The sample diameter was set to 0.9 mm, around which a 0.3-mm-thick copper wire was wound with a filling factor of 56%. For the different test configurations, different numbers of closely wound turns were utilized. The image-encoding gradient was applied along the cylinder symmetry axis (the y axis), if not otherwise mentioned.*

Intriguingly, a flip angle corresponding to 280° in the center of the solenoid provided the highest SNR at imaging resolutions between 0.6 and 1.8 mm. If imaging resolution was between 0.2 and 0.6 mm, a flip angle of 450° would become the most optimal one, and so forth. This phenomena is further clarified with Fig. 8.9, where the achieved transverse magnetization profiles are illustrated with respect to the nominal flip angles of 100°, 280°, and 450° at the center of the coil. It was seen that the contrast in achieved flip angles between adjacent voxels in-

creased with higher nominal flip angle values. This corresponded subsequently to a higher spatial selectivity, i.e., a smaller effective sample size, which would enable magnetic field monitoring assisted image acquisitions with higher resolutions.

From Fig. 8.8, it was also noticed that, if pulses providing the second signal maximum are pursued (i.e., the nominal flip angle was $\sim 280^\circ$), the maximum of the signal amplitude did not occur right after the RF pulse but rather when the spins from the first and the second local subvolumes constructively interfered with each other. By increasing the multiples of π to the nominal 90° flip angle, the number of temporal and spatial signal maxima increased correspondingly. Note that a perfectly homogeneous background field was assumed in these simulations for the sake of clarity.

8.4 MRI susceptometer

To determine accurately the correct dopant concentrations for susceptibility-matched epoxies, a method was needed to perform susceptometric measurements at sub-ppm precision. One plausible approach was to utilize an MRI scanner for this purpose. Although the susceptibilities of epoxy samples are not directly measurable with the MRI-based technique owing to the very short T2 time of proton spins in epoxy, one can determine the susceptibility value indirectly by placing an epoxy sample into a water bath and by studying the resulting B_0 perturbations in the water.

By applying two gradient echo sequences with two different echo times, the phase differences between the two images relate linearly to the relative local ΔB_0 value:

$$\Delta B_0 = \frac{\varphi(\mathrm{TE}_2) - \varphi(\mathrm{TE}_1)}{\gamma(\mathrm{TE}_2 - \mathrm{TE}_1)}, \tag{8.4}$$

where $\mathrm{TE}_2 > \mathrm{TE}_1$. If a cross-sectional image of an epoxy cylinder in a water bath is acquired, a dipole pattern emerges, as is predicted by Eq. 8.3. Measured field points in the vicinity of the epoxy samples can be inserted into Eq. 8.3 and averaged to give a better estimate for the relative susceptibility value of the epoxy, namely,

$$\Delta\chi = \frac{1}{A}\int_A \frac{2\Delta B_0(x,z)}{B_0 a^2}\,\frac{(x^2+z^2)^2}{z^2-x^2}\,dxdz. \tag{8.5}$$

The relative susceptibility value that is obtained by this method can be converted subsequently to an absolute value based on the known susceptibility of water.

When conducting such susceptibility measurements, care should be taken to ensure that the ends of an epoxy cylinder do not influence the measurements.

In addition, the echo time difference should be adjusted in a way such that no phase-wrapping artifacts occur. Otherwise a utilization of a more complex two-dimensional phase-unwrapping algorithm is required [146].

8.5 Susceptometric measurements

Cylindrical, 60-mm-long epoxy samples with different levels of a paramagnetic Er^{3+} dopant were manufactured to find the concentrations that would match the susceptibility of epoxy to the values of water and copper. The curing of the epoxy samples took place in a vacuum environment to ensure that no additional air molecules could erroneously contribute to the volume susceptibility. Consistently, the water bath for the susceptometric measurements was degassed in a vacuum environment. The susceptibility of each test sample was estimated with the method described in Section 8.4. The test cylinders were set far enough apart from each other as well as from the edges of the water bath. This ensured higher homogeneity in the background magnetic field that each sample was experiencing. Figure 8.10 shows a magnetic field map acquired during one of the MRI-based susceptometric measurements.

A linear dependency between Er^{3+} concentration and corresponding susceptibility could be estimated as

$$\chi(n_{Er^{3+}}) = \chi_0 + \alpha\, c_{Er^{3+}}, \tag{8.6}$$

where χ_0 is the intrinsic susceptibility of the epoxy, $c_{Er^{3+}}$ is the Er^{3+} ion concentration, and α is a constant dependent on the density and the volume susceptibility of the dopant. The outcome of the conducted susceptibility measurements is shown in Fig. 8.11. By interpolating the measurement data, dopant levels that corresponded to the susceptibilities of copper and water were found. Here, a measurement inaccuracy of approximately 0.15 ppm was estimated based on the repeatability of the measurements. This error was expected to be mostly due to the difficulties in producing accurately the desired Er^{3+} dopant concentrations, as well as due to errors in the numerical estimation of the two-dimensional magnetic momentum.

8.6 Discussion and conclusions

NMR probes that are based on the standard, long-interval excitations scheme require long sample T2* values to ensure up to 100-ms read-out times. Significant

signal dephasing is experienced already as a result of sub-ppm susceptibility differences in the materials that are utilized in the probe constructions. Therefore, the magnetic properties of the utilized materials should be carefully addressed, and, consequently, this makes the manufacturing process of such susceptibility-matched NMR probes delicate and sensitive to any magnetic impurities.

Different susceptibility-matching techniques with individual drawbacks and benefits exist for manufacturing NMR probes. For suppressing the coil-induced B_0 inhomogeneities, a solid susceptibility-matched enclosure, e.g., made out of epoxy, gives better mechanical robustness in comparison to techniques that rely on susceptibility-matching liquids. A higher filling factor, and thus an improved SNR, is achieved by omitting the glass capillary and by manufacturing the sample holder completely out of epoxy. Placing the coil right next to the sample is especially beneficial for high-resolution imaging ($\Delta x < 0.5$ mm), which requires smaller sample dimensions without a compromised filling factor. Such a probe design is, however, very sensitive to errors in the susceptibility matching and to any air bubbles or other impurities that are accidentally introduced into the sample space during the manufacturing process. With a careful manufacturing process the amount of impurities can be reduced to a level that ensures 100-ms or longer read-out times with the manufactured NMR probes. Although having a clean-room environment can be beneficial, it is not obligatory in manufacturing.

When using epoxy, its hygroscopic nature should be countered to preserve a good measurement repeatability and long-term stability. Addressing this matter is especially crucial if no capillaries are utilized to isolate the NMR samples from the epoxy enclosures. Saturating the epoxy with water in combination with an airtight coating is proposed to solve this problem. No errors are expected to be induced into NMR probe signals or MR images by these water molecules, since these are assumed to be bound to the epoxy lattice efficiently enough to keep the T2 value of the molecules very short.

By utilizing glass capillaries and liquid plugs (e.g., doped heavy water), the sample (e.g., cyclohexane) volume is less likely to be contaminated by impurities during manufacturing. The design however is still vulnerable to air bubbles that can find their way into the plug-sample interfaces. Vibrations in combination with introduced air bubbles can lead to a dislocation of the NMR sample from the coil center. For high-resolution imaging, achievable filling factors, i.e., relative SNRs, are also expected to get reduced since the capillary wall thickness cannot be scaled down by the same factor as the sample diameter.

Better robustness against impurities and air bubbles is obtained by exploiting the relatively steep drop-off in the sensitivity profile of a solenoid coil. No physical plugs in this design are required, and the capillary can be made long enough to ensure that small air bubbles at the ends of the sample space do not distort

the field homogeneity at the center of the sample. In the case of receive-only NMR probes, the drawback of the design is that the sensitivity drop-off is not as sharp as desired. Therefore, image resolutions as high as would be possible with probes based on a physically limited sample space cannot be applied with this design.

By utilizing NMR probes in the transmit-receive configuration and applying greater than 90° flip angles, the effective sample volume can be reduced for high-resolution imaging. If the excitation power is restricted, a drawback of using higher flip angles is a longer excitation pulse width and consequently a narrower excitation bandwidth. Furthermore, a loss in SNR is expected with this method since fewer spins are effectively tilted into the transverse plane. Despite its simplicity, the greatest drawback of this probe design is that it is applicable only if probes are operated with the standard, long-interval excitations scheme.

All the susceptibility-matching methods that were considered here required an accurate adjustment of the susceptibility values of the materials that are enclosing the NMR probe. In this work, two-component epoxy was utilized and the susceptibility tuning of the material was effectively done by mixing non-reactive, paramagnetic dopants to epoxy during the curing phase. The correct dopant concentration was verified with a good accuracy with an MRI-based susceptometer. In this method, material samples were submerged into a water bath, and the consequent field inhomogeneity patterns were studied with gradient-echo-based field maps. The sensitivity of such a susceptibility measurement was easily adjusted by changing the echo time difference of the two gradient echo acquisitions. An alternative method for increased sensitivity would be to manufacture test cylinders with larger diameter. For liquid samples, large-diameter test tubes with a thin wall thicknesses are proposed.

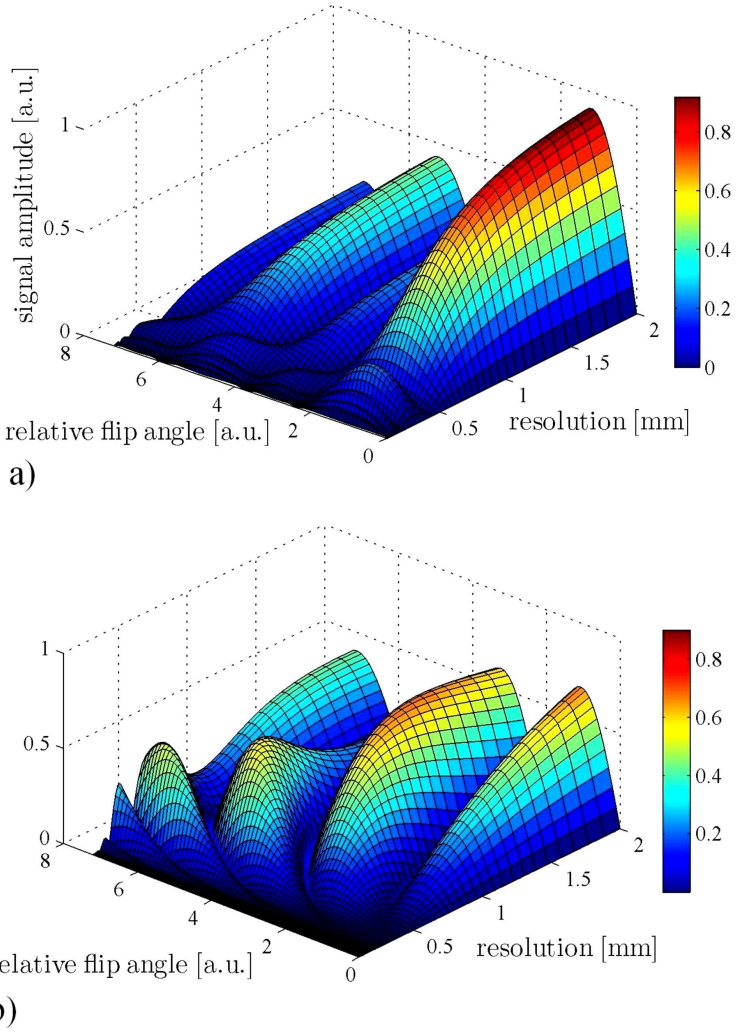

Fig. 8.8. *Signal levels of a Tx-Rx NMR probe after image-encoding gradients. Here, a probe design was studied that relied on the spatially constrained sensitivity profile of a solenoid coil to restrict the NMR sample volume. The signal amplitudes are given here as a function of an applied excitation field, i.e., as a function of the achievable flip angle, and as a function of a gradient envelope, i.e., as a function of the achievable imaging resolution. The flip angles were normalized to a value that corresponded a 90° excitation in the center of the solenoid. In (a), the imaging gradient was along the symmetry axis of a cylinder-shaped NMR sample, and in (b), it was perpendicular to this.*

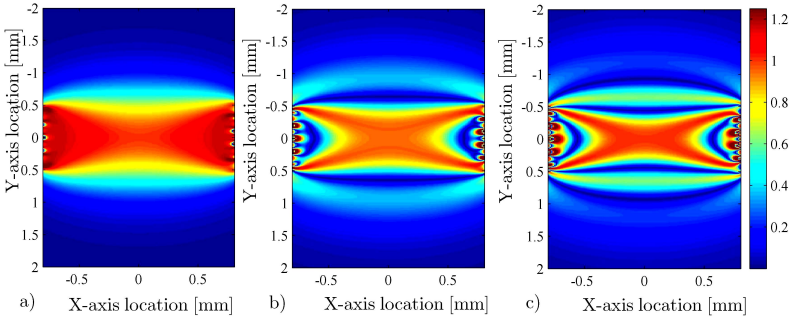

Fig. 8.9. *Spatial sensitivity profiles of a transmit-receive NMR probe (with 5 turns, a diameter of 1.7 mm, and a length of 1.0 mm) showed with three different nominal flip-angle values. Here, nominal pulses of (a) 90°, (b) 270°, and (c) 450° were provided to the coil. The sensitivity scale is normalized to the value at the center of the coil.*

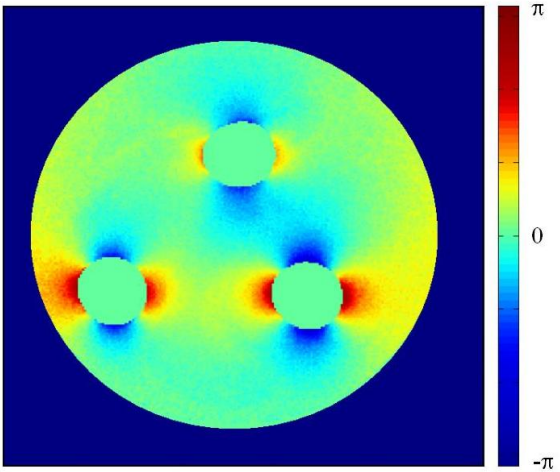

Fig. 8.10. *Three epoxy samples, with 20-mm diameters and varying susceptibility values, were submerged into a water bath and a static magnetic field map was acquired with the help of two gradient echo sequences with different echo times. The field perturbations were converted to the phase differences with respect to the background field. The dipole-shaped field perturbations resulting from the susceptibility mismatch between the epoxy samples and the water bath are noticeable. In this experiment, the topmost sample was observed to have the best susceptibility match to water.*

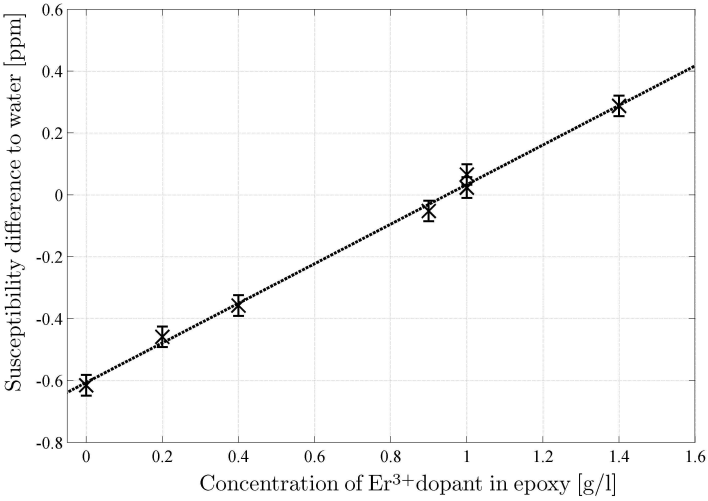

Fig. 8.11. *Measured volume susceptibilities of different epoxy samples with respect to different paramagnetic Er^{3+} concentrations. The susceptibilities are given referenced to the susceptibility of water, $\chi = -9.05$. The relation to the dopant concentration was observed to follow a linear curve within the limits of measurement uncertainty.*

9

Implementation of an NMR-Probe-based Magnetic Field Monitoring System for MRI

Utilizing NMR-based magnetometers for magnetic field monitoring assisted MRI is studied in this chapter. The work goes through the different probe designs and operating schemes that have been presented in Chapters 6 and 8. The chapter begins with theoretical considerations to understand the components that affect the measurement uncertainty in NMR-probe-based magnetic field monitoring. The outcomes of these considerations are then applied for the different NMR probe techniques that have been developed in this thesis and are compared. Simulation results and practical experiments for NMR-probe-based magnetic field monitoring are presented individually with respect to each probe technique. All the MRI-related practical experiments and probe characterizations are done with a clinical 3.0-T MRI scanner (GE Signa Excite, GE Healthcare, WI).

9.1 Uncertainty in magnetic field measurements

9.1.1 Noise-related errors

The relation between the average probe SNR and the achievable accuracy, repeatability, and precision in the magnetic field measurements are studied. Bandwidths of NMR signals at clinical field strengths lay roughly between 10 and 500 MHz, and equally distributed spectral noise can therefore be assumed. Only the out-of-phase noise, i.e., the component perpendicular to the signal vector, contributes to the uncertainty of the signal phase, $\Delta\varphi$. If a root-mean-square value for the phase noise is calculated, one gets

$$\Delta\varphi \approx \frac{\sqrt{\frac{1}{2\pi}\int_0^{2\pi}(U_{noise}\sin\theta)^2\,d\theta}}{U_{probe}}\,[\text{rad}] = \frac{1}{\sqrt{2}}\frac{1}{\text{SNR}}\,[\text{rad}]. \tag{9.1}$$

From the Larmor relation (cf. Eq. 2.4) and assuming that the uncertainty in the modulation frequency of the receiver and the monitoring time step, $\Delta t = 1/(f_m)$, are insignificant, one obtains an estimate for the field uncertainty [34]:

$$\Delta B = \frac{\sqrt{2}\Delta\varphi}{\gamma\Delta t} = \frac{f_m}{\gamma\text{SNR}}. \tag{9.2}$$

Here, the factor $\sqrt{2}$ arises from the fact that the phase value obtained is the differentiation of two successive, uncorrelated measurement points. If the precision requirement, i.e., Eq. 3.4, is combined with Eq. 9.2, and it is assumed that the probe separation $|\mathbf{r}|$ equals the FOV and that the monitoring rate for nuclei-X-based probes can be different from the imaging rate f_s, one gets for the minimum affordable probe SNR that

$$\text{SNR} \geq \frac{\gamma_{\text{H}}}{\gamma_{\text{X}}}\frac{f_m}{f_s}\frac{1}{2\pi|\Delta\mathbf{k}|}\,[\text{rad}]. \tag{9.3}$$

It should be noted that, for ^{1}H acquisitions with <50-kHz sampling bandwidth, an SNR increase can be obtained by lowering the monitoring bandwidth from the Nyquist limit to match the sampling rate of the imaging. For ^{1}H acquisitions above 50 kHz, the monitoring bandwidth should either match $\gamma_{\text{H}}/\gamma_{\text{X}} \cdot f_s$ or 50 kHz, whichever is higher. This maximizes SNR and avoids signal aliasing either in NMR signals or in processed field data. In Chapter 3, the requirement of $\sqrt{2}\pi|\Delta\mathbf{k}|/\gamma_{\text{H}} \leq 53$ pTs for the acceptable measurement uncertainty was derived. Hence, it is seen that the precision requirement for magnetic field monitoring is at the most demanding at the lowest imaging bandwidths, which are typically down to 10 kHz. If the worst case is assumed, then the precision requirement can be rewritten as 0.53 pT/Hz$^{3/2}$.

For measuring static B_0 values, linear regression can be applied for increased precision, and the measurement accuracy becomes [34]

$$\Delta B_0 \approx \frac{\sqrt{6}}{\gamma\,\text{SNR}_{avg}\,T_{obs}}. \tag{9.4}$$

Here, T_{obs} stands for the measurement time. Hence, lengthening the acquisition time increases the accuracy of the static field measurement.

9.1.2 Chemical shift and sample size

Systematic errors in static B_0 measurements arise if the intrinsic chemical shift of an NMR probe is not characterized. Such a calibration can be performed by first characterizing the value of the B_0 field in a chosen FOV location of an MRI scanner. This can be done with a phantom with a known susceptibility, e.g., water, which is placed in the same location at a controlled temperature. The precession frequency is measured, and the field value is calculated from the Larmor relation, i.e., Eq. 2.4, based on the known chemical shift and the gyromagnetic ratio of the phantom. It should be noted here that the geometry influences the chemical shift experienced in the object of interest and therefore it should also be taken into account [53]. After the value of the background magnetic field is calibrated, the chemical shift of the probe is determined by placing the probe into the magnetic field and reversing the procedure.

Ultimately, the accuracy of the calibration comes down to the accuracy at which the gyromagnetic ratio of the utilized nuclei has been determined. The National Institute of Standards and Technology gives an uncertainty of $<$30 ppb for ^1H_2O [147]. In addition, any drift in the ambient temperature reduces the validity of the NMR probes' chemical shift calibration. It has been estimated that a drift of $\pm$4 K in the temperature value leads to an uncertainty of 1 to 15 ppb, depending on the materials that are utilized to manufacture the NMR probes [34, 148].

An additional measurement error arises from the fact that an NMR sample is not a point source but the detected signal is an averaged value of the total field over the spin ensemble. If an average measurement error is considered, then

$$\Delta B = \frac{1}{\Delta V} \int_{\Delta V} \mathbf{G}(\mathbf{r}) \cdot (\mathbf{r} - \mathbf{r}_0)\, dV, \tag{9.5}$$

where ΔV is the sample volume and $\mathbf{r}_0$ is the location of the probe's center point. Here, it is seen that the sample size does not influence the measurement error of linear field gradients. For static measurements, the significance of an error depends on the inhomogeneity of the field that is being measured. For standard clinical MRI scanners, the intrinsic field homogeneity is typically specified to be below $\sim$2.5 ppm/m throughout the whole field of view. Hence, it is obtained from Eq. 9.5 that the spreading of the signal linewidth across a 1.0-mm-sized sample would equal a B_0 measurement error of $\leq$5 ppb.

9.1.3 Intrinsic field inhomogeneity of an NMR sample

Owing to mismatches in the susceptibility values of the different materials that are utilized in probe constructions, a magnetic field across an NMR sample can

vary. This causes a line broadening in the measured Larmor frequency and consecutive measurement errors, especially during long monitoring windows. With susceptibility-matching techniques, a field homogeneity close to 10 nT can be achieved. This value is larger than the estimated value of 710 pT in Chapter 3 that was considered to be still acceptable for a signal drift during a 100-ms-long monitoring period. The error related to the intrinsic field homogeneity can be compensated by calibrating the spectral response of the NMR sample and by convolving its Fourier transform with monitoring data.

With NMR probes based on coherent, short-interval excitations, the T1 and T2 values of an NMR sample are adjusted to values of two to three orders of magnitude lower than those with probes based on the standard, long-interval excitations. The field homogeneity requirement is consequently relaxed by the same factor for the benefit of the coherent, short-interval excitations-based probes.

9.1.4 Dispersion

Any delays in an MR receiver chain, and hence in cables, tuned RF coils, preamplifier inputs, or RF filters, can introduce dispersion-related phase shifts in the signals that are being measured. Simulations based on the model shown in Fig. 6.4 were performed with parameter values that match a typical ^{1}H coil design. In combination with appropriate S-parameter measurements of the utilized receiver chain, it was simulated that the dispersion could be estimated to be linear over the relatively narrow bandwidths of NMR signals and that the dispersion constants corresponded to values of $2\pi\tau = 1\text{-}2\ \mu$rad/Hz (cf. Fig. 9.1). The influence of the signal dispersion could therefore be estimated as a delay in the measured signal with values of 0.2-0.4 μs.

In Chapter 3, the maximum acceptable timing error of 40 ns was derived, which is, hence, smaller than is expected to be introduced by the dispersion in the receiver electronics. By calibrating the responses of the magnetometers, and applying the individual delay values in postprocessing, errors from the dispersion can be suppressed below a level that causes reconstruction artifacts.

9.2 Receive-only ^{1}H NMR probes

Based on Eq. 6.15, simulations to find theoptimal RF coil geometry were conducted for receive-only ^{1}H NMR probes with a given sample size. A cylindrical sample volume with a 1 mm length and a 1 mm diameter was chosen here;

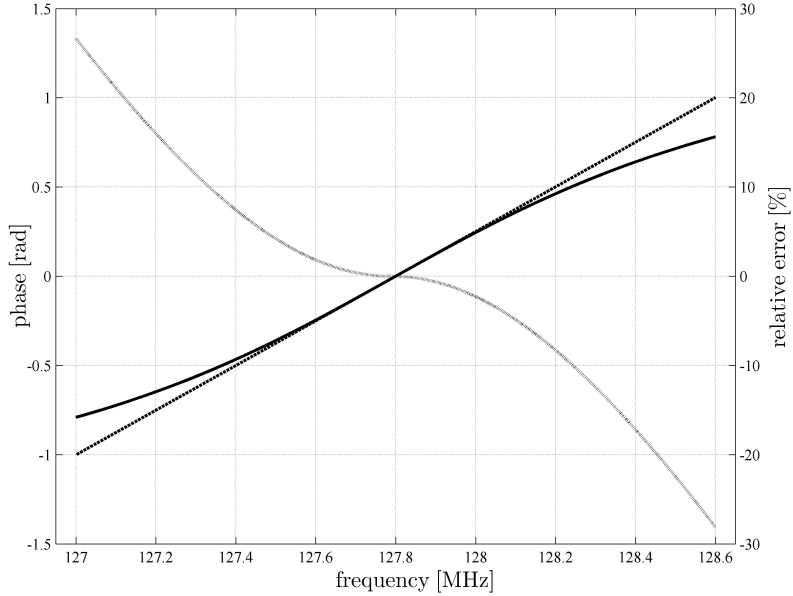

Fig. 9.1. *Dispersion of a ^{1}H signal from a tuned solenoid coil , plotted with a solid line and with respect to a measurement frequency. At narrow bandwidths, the dispersion can be approximated to be linear, as is illustrated with a dashed line. The error of this linear approximation is shown with a dotted line. The coil geometry that was applied for the simulations corresponded to a typical ^{1}H geometry with a quality factor of 80.*

hence with these dimensions, magnetic field monitoring assisted MRI is applicable down to image resolutions of 0.5 mm. A realistic 55% filling factor was used in the simulations, and the effects of the receiver electronics to the total noise level were omitted apart from the matching and tuning capacitors. From Eqs. 6.25, 6.30, and 6.34, it was noticed that the sample losses were three orders of magnitude smaller than the resistive coil losses even if the NMR sample was doped with $CuS0_4$ for a reduced T1 of 100 ms.

To avoid self-resonance and standing-wave effects in the coil, and to ensure that the applied quasistatic analysis based on the Biot-Savart law was applicable, the coil dimensions were limited to values clearly smaller than the signal wavelength. The Larmor frequency of ^{1}H spins at a 3.0-T background flux density corresponds to a free-space wavelength of 2.3 m. The wavelength is reduced to $\sim$1.0 m in Pyrex glass, and it becomes $\sim$25 cm in distilled water [54]. Based on

these values, conservative limits of 10 cm for the total coil wire length and 10 mm for the coil length were determined.

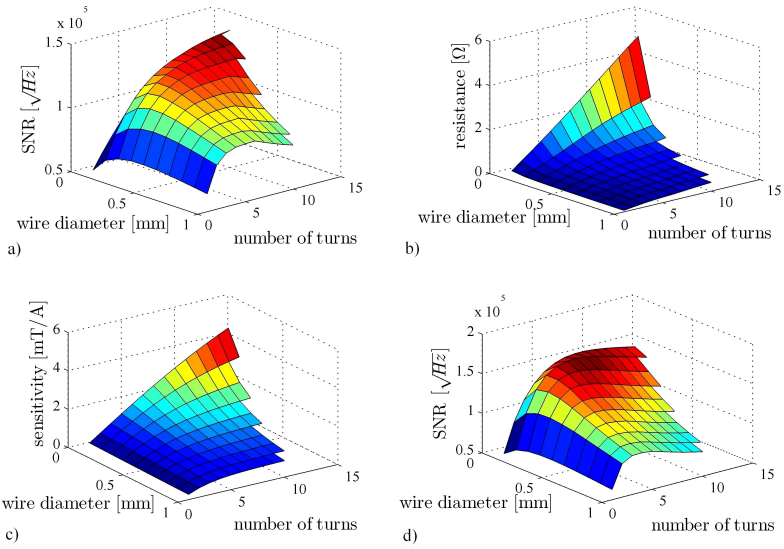

Fig. 9.2. *(a) Simulated SNR values of various solenoid coils with various wire diameters and numbers of turns. In the simulations, the coil turns were assumed to be wound closely together, and the maximum number of turns was set to be limited either by the maximum coil length (10 mm) or by keeping the total wire length clearly smaller than the free-space wavelength (100 mm). The SNR was divided into (b) resistance and (c) sensitivity plots. To minimize the proximity effect, thus reducing the coil resistance, (d) the simulation results with 200-µm spacing between turns are also shown.*

The results of the conducted simulations are illustrated in Fig. 9.2. With the optimal coil geometry, an SNR of $\sim 1.6 \times 10^5 \sqrt{\text{Hz}}$ was estimated to be achievable. The proximity effect was reduced by introducing space between adjacent turns, which led to a slight increase in SNR. Coil configurations with a larger number of turns were observed to became less ideal owing to the reduced sample length versus coil length ratio; hence, the sensitivity increase of a coil did not compensate for the resistance increase.

Receive-only ^{1}H NMR probes were manufactured for the proof-of-concept experiments based on a capillary-less probe design with solid epoxy plugs to

constrain the sample volume (cf. Figs. 8.5b and 9.3). The chosen design was estimated to offer a higher achievable SNR and better down-sizing for high-resolution imaging than designs based on sample capillaries. The NMR sample diameter was set to 1 mm, and the sample length to 2 mm. No paramagnetic dopant was added into the distilled water sample for adjusting T1 and T2 times. The chosen solenoid coil geometry was based on the simulations for optimal SNR (cf. Fig. 9.2). A compromise was made for a slightly larger wire diameter that was preferred over the maximum achievable SNR. This decision was made since a certain level of robustness was required for the coil construct during the epoxy molding phase, which was making geometries based on small wire diameters less attractive. The chosen geometry had 6 turns, with 0.5-mm copper wire thickness and 0.2-mm wire spacing. A spacing of 250 μm between the coil and the sample was set to relax the susceptibility-matching requirements between the copper and the epoxy as well as to make the construction less sensitive to possible impurities at the surface of the solenoid coil. This probe design gave a filling factor of 57%.

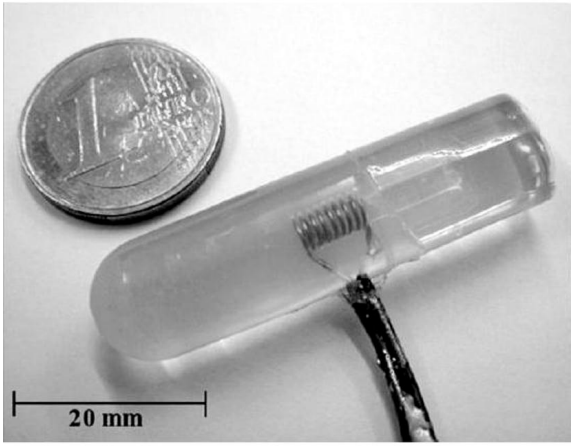

Fig. 9.3. *Photograph of an NMR probe with an epoxy casing for susceptibility matching and increased mechanical robustness. In this design, no capillaries were utilized, but the sample space was molded directly into the epoxy. Semirigid coaxial cables were utilized to keep the matching and tuning electronics far enough from the probe.*

Manufactured ^{1}H NMR probes were tuned to 127.8 MHz, matched to 50 Ω, and connected to a preamplifier, as was illustrated in Fig. 6.4. The utilized

MRI compatible preamplifiers (GE Healthcare, Milwaukee, WI) offered a gain of 27 dB with a noise figure of 0.7 dB. All the electrical components in the probe constructions were ensured to be MRI compatible of the second kind to avoid any image artifacts and T2*-related signal decays in the NMR probes.

In S-parameter measurements, the NMR probes showed quality factors (cf. Eq. 6.35) of 71 ± 3 with no noticeable differences for whether or not probes were loaded with a water sample. Good consistency with the simulated value ($Q_{simulated} = 73.4$) indicated the correctness of the theoretical considerations and verified the assumption that the sample losses were insignificant in comparison to the coil losses. The small reduction in the measured quality factor to the simulated one is assumed to come from the losses in the capacitor that is utilized to tune the resonant circuit.

The preamplifier outputs of the NMR probes were interfaced to a standard ^{1}H multireceiver system of a 3.0-T MRI scanner (3T Signa Excite, GE Healthcare, Milwaukee, WI) via a commercial eight-channel 3.0-T MRI connector (Hypertronics, London, UK). In addition to the RF signal paths for the reception, the connector provided supply voltages for the preamplifiers and a biasing for the PIN-diode-based active detuning. The probe electronics were designed in a way such that the supply voltage and the biasing signals, which are typically intended for phased-array MRI coils, could be utilized for the NMR probes without any configuration changes in the MRI system itself.

In MRI-based tests to characterize the manufactured NMR probes, the excitation pulses were matched by adjusting the RF transmitter gain to provide the 90° flip angles. Free-induction decay curves were studied to find the SNR and T2* values of the NMR probes. The manufactured probes showed an SNR performance of $1.6 \times 10^5 \sqrt{\text{Hz}}$ and a maximum T2* value of 150 ms. The theoretical SNR was calculated as $2.0 \times 10^5 \sqrt{\text{Hz}}$ with the utilized probe design, indicating a good agreement between the simulations and practice.

The achieved spectral SNR of $1.6 \times 10^5 \sqrt{\text{Hz}}$ corresponded to an uncertainty of 23 fT/Hz$^{3/2}$ (cf. Eq. 9.2). Hence, the the precision requirement of 0.53 pT/Hz$^{3/2}$ that was derived in Chapter 3 was clearly fulfilled. During 100-ms-long acquisitions, the measurement uncertainty was expected to get doubled based on the probes' 150-ms-long T2* time. For static field measurements, a precision of 2.3 pT could be achieved when the monitoring signal was averaged over a 100-ms-long time period (cf. Eq. 9.4).

9.3 Counterwound transmit-receive ^{1}H NMR probes

The suitability of the developed transmitter hardware for independent NMR probe excitations was studied. In comparison to receive-only probes, higher signal levels were expected with transmit-receive probes owing to the ensured 90° flip angles. Therefore, further improvements in decoupling techniques were necessary. For these experiments, the counterwinding decoupling strategy was chosen for the probe design instead of RF shields. The decision was made on the basis of simulation results showing that RF shields can distort high frequency components of the magnetic fields being measured. In addition, RF shields can cause potential SNR losses in standard imaging, and they can compromise patient safety if the probes are placed near an imaging coil or a patient, respectively .

A probe design was chosen in which an NMR sample was sealed into a glass capillary and the sample volume was constrained by susceptibility-matched epoxy plugs. In comparison to the capillary-less probe design, a higher filling factor (and hence SNR) was traded for more robust functionality. Because of the utilized glass capillary, the change was notably reduced that the T2* performance would be deteriorated by any impurities in the sample volume or by the sample diffusion owing to the hygroscopic nature of epoxy. The probe sample diameter and the length were both set to 0.9 mm; thus, MRI acquisitions with resolutions down to 0.45 mm could be accomplished with this design (cf. Eq. 6.7). The solenoid coil was wound around the NMR sample with a filling factor of 55%. The number of closely wound turns was set to four. Two 2-turn counterwindings were placed symmetrically on both sides of the 4-turn solenoid coil for signal detection. The wire diameter of the coil construct was chosen to be 0.3 mm.

The utilized transmit-receive duplexer was based on the passive design that was shown in Fig. 6.5b. For exciting the NMR probes, a separate RF transmitter was utilized, as was explained in Chapter 7. The “start sequence” trigger signal from an MRI scanner (3T Signa Excite, GE Healthcare, Milwaukee, WI) was routed to a timing and the pulse width controller. For signal reception, the probes were interfaced with a multichannel receiver of the MRI scanner in a similar fashion to the receive-only ^{1}H NMR probes.

The probe performances were characterized based on FID measurements with the 3.0-T MRI scanner. Approximately 4.7-μs-long pulses delivered the nominal flip angle of 90°. The applied RF pulse width was somewhat higher than the calculated 2.5-μs value (cf Eq. 7.2). The difference was expected to be due to additional losses and reflections in the transmit chain. The obtained spectral SNR of $5.5 \times 10^4 \sqrt{\text{Hz}}$ with the NMR probes corresponded to an uncertainty

of 68 fT/Hz$^{3/2}$. The achieved SNR value was above the estimated minimum limit for effective magnetic field monitoring assisted MRI of 0.53 pT/Hz$^{3/2}$. Acceptable probe T2* values of up to 150 ms were typically achieved, and averaging over 100-ms-long acquisition periods was calculated to result in a precision of 6.9 pT in static field measurements (cf. Eq. 9.4).

The signal coupling between counterwound NMR probes and a eight-channel imaging coil was studied with an MRI-based measurement (cf. Fig. 9.4). The NMR probes were placed around the imaging coil with a proximity of 4 to 5 cm, and a spherical water phantom, with an 18-cm diameter, was placed inside the imaging coil. After the NMR probes and the phantom were excited, FID signals were monitored. The spectral response showed a coupling of -40 to -50 dB. The experiment verified that, in comparison to standard solenoid coils, the counterwindings could be utilized for improved signal decoupling by 10 to 15 dB.

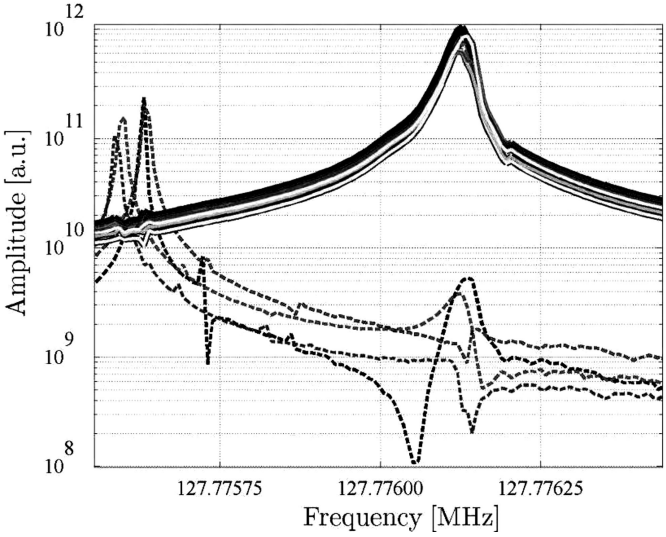

Fig. 9.4. *Signal spectra of four NMR probes (illustrated with dashed lines) and an eight-channel head receiver array (the signals of each element being illustrated with a solid line). The coupling between the NMR probes and the head array is observable. Furthermore, the experiment showed a susceptibility difference of 1.7 ppm, and hence a chemical shift of 450 Hz, between the phantom and the NMR probes.*

9.4 Transmit-receive ^{2}H NMR probes

For the non-proton-based NMR probes, deuterium nuclei, ^{2}H, were utilized. The relatively low gyromagnetic ratio of ^{2}H was not considered to be problematic since, as was shown by Eq. 6.40, the consecutive loss in the relative SNR could be compensated for by having larger sample sizes. The use of ^{2}H nuclei, and especially the heavy water molecule, ^2H_2O, was favored for several reasons. ^2H_2O has a spin density that is equivalent to ^1H_2O. Because ^{2}H is a spin 1 system, a relative signal increase is expected in comparison to the 1/2 spin system of ^{1}H nuclei (cf. Eq. 6.15). The liquid form of ^2H_2O gives a high intrinsic T2 relaxation time (770 ms [149]), which is required for long read-out times. The chemical and magnetic properties of ^2H_2O are close to ^1H_2O; thus, susceptibility matching as well as adjusting the T1 and T2 relaxation times can be performed with methods similar to those used earlier for ^{1}H-based probe designs. Coupling and cross-talk distortions with MRI coils and imaging objects are practically eliminated as a result of the clearly different gyromagnetic ratio of ^{2}H ($\gamma_{^2H}$ = 6.54 MHz/T versus $\gamma_{^1H}$ = 42.6 MHz/T). This holds true not only for proton-based imaging but also for other nuclei used for functional and metabolic MRI studies: for instance, ^{3}He ($\gamma_{^3He}$ = 32.43 MHz/T), ^{13}C ($\gamma_{^{13}C}$ = 10.71 MHz/T), ^{19}F ($\gamma_{^{19}F}$ = 40.08 MHz/T), or ^{23}Na ($\gamma_{^{23}Na}$ = 11.27 MHz/T) [43]. With ^{2}H-based NMR samples, the phase-unwrapping algorithm has a smaller chance of failure during any high-gradient performance because of the lowered signal bandwidth (cf. Eq. 6.6). Failure in the phase unwrapping is in practice the determining factor for how long the magnetic field profiles can be reliably tracked.

Of the available probe designs for ^{2}H NMR probes, the one chosen was that in which the NMR sample was injected into a glass capillary and the effective sample space was restricted along the capillary symmetry axis by the inhomogeneous sensitivity profile of the utilized solenoid coil. This probe design gave higher robustness against potential impurities in the sample volume than the capillary-less probe design and the design in which the sample volume inside the capillary is constrained by physical plugs. Furthermore, the utilized capillary reduces any sample diffusion through the epoxy, thus improving long-term stability.

The simulation results for the optimal coil geometry with respect to sample size and applicable imaging resolution are illustrated in Figs. 9.5 and 9.6. Based on these simulations, ^{2}H-NMR-probe prototypes with 1.7-mm sample diameter and with a filling factor of 76% were manufactured. Such a probe design offered magnetic field monitoring assisted MRI for imaging resolutions down to $\sim$0.15 mm. The RF coils in this design had five closely wound turns that were made out of 0.5-mm copper wire. The counterwindings-based probe-to-probe decou-

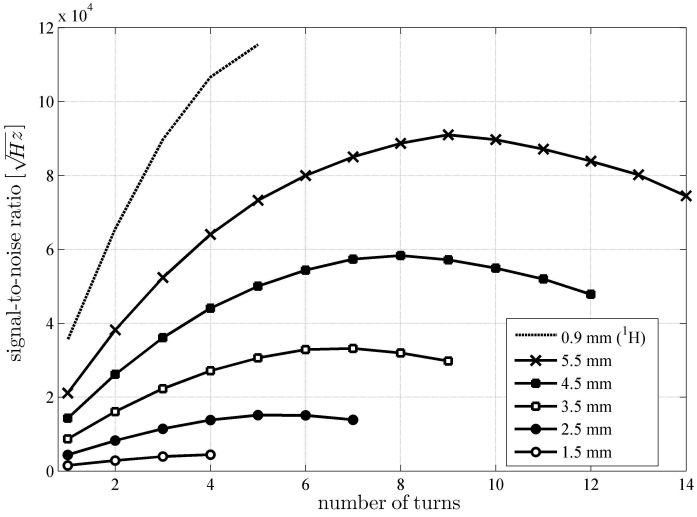

Fig. 9.5. *Simulated SNR values obtained with different ^2H NMR probe coil geometries. The number of turns was limited by the coil length, which was set to be 1.25 times the sample diameter. The notch in the SNR curves is due to the proximity effect, which increases when the increasing number of turns are packed more closely to each other. For a comparison, an analysis for an ^1H NMR probe is plotted with a typical sample size of 0.9 mm and a filling factor of 55%.*

pling strategy was omitted since the low-input-impedance preamplifier decoupling strategy was considered to be sufficient with the lower Larmor frequency of ^{2}H nuclei. This assumption was verified with S-parameter measurements that showed that, when probes were placed 40 mm or more away from each other, the coupling was <-50 dB and hence less than the expected SNR.

A passive transmit-receive duplexer design, as was shown in Fig. 6.5b, was utilized for operating the probes. The matching and tuning network and the quarter-wavelength cables were modified to match the Larmor frequency of ^{2}H at 3.0-T background flux density. Commercial 3.0-T ^{2}H low-noise preamplifiers (Microwave Technology, Fremont, CA) were utilized for both the first- and the second-stage amplifications. Band-pass filters (SBP-21.4, Mini-Circuits, Brooklyn, NY) provided antialiasing filtering before the homemade multichannel receiver. The manufactured microcontroller-based timing circuitry handled the timing and synchronization of transmit pulses and the starting points of data acquisitions.

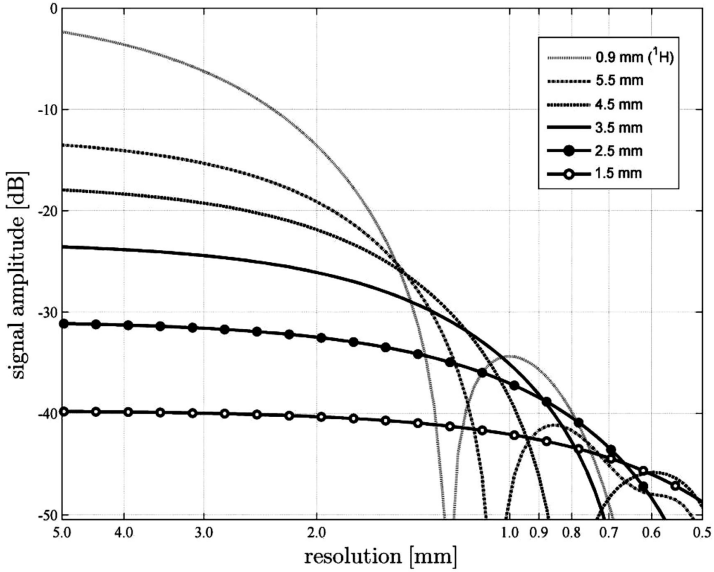

Fig. 9.6. *Signal loss as a result of gradient-induced signal dephasing was studied with various sample sizes. Although providing a higher SNR, large sample sizes suffered from a severer signal loss if high-k-space values were applied, e.g., in high-resolution imaging. The coil geometries equaled the optimal SNR configurations for each sample diameter, as was introduced in Fig. 9.5. For comparison, performance of an ^{1}H NMR probe with a typical sample size and the related optimal coil geometry is plotted as well. In SNR calculations, the γ_H/γ_H reduction in the measurement bandwidth was taken into consideration.*

With a nominal 31-dBm excitation power in a four-probe configuration, pulse widths of approximately 25 μs provided excitations for 90° flip angles. After an RF excitation, a succeeding FID curve was studied, and the SNR was observed to be approximately $1.7 \times 10^4\sqrt{\text{Hz}}$. From the same experiment, an estimate of 200-250 ms for a T2* value was obtained.

With a modern ^{1}H MRI scanner, the imaging bandwidth can be up to 1 MHz. This transfers to a maximum sampling rate of 154 kHz for ^{2}H probes. Hence, the achieved spectral SNR of $1.7 \times 10^4\sqrt{\text{Hz}}$ with the 1.7-mm-diameter sample probes yields from Eq. 9.2 a precision of 1.4 pT/Hz$^{3/2}$. For static field measurements with this NMR probe design, averaging over a 100-ms-long acquisition period was calculated to result in a precision of 50 pT (cf. Eq. 9.4).

In Chapter 3, a monitoring precision of 0.53 pT/Hz$^{3/2}$ was estimated to deliver the desired 40-dB signal-to-artifact ratio for magnetic field monitoring assisted MRI. These simulations to determine monitoring precision also showed a roughly linear relation between measurement errors and the level of image artifacts on a double logarithmic scale. Hence, the precision of 1.4 pT/Hz$^{3/2}$ achieved with ^{2}H NMR probes is estimated to be sufficient for efficient magnetic field monitoring assisted MRI with a theoretically calculated signal-to-artifact ratio of $40 - 8.4$ dB = 31.6 dB. Since the requirement for monitoring precision is reduced with an increased imaging bandwidth, it is estimated that the manufactured ^{2}H NMR probes would deliver the desired 40-dB signal-to-artifact ratio as long as ^{1}H imaging bandwidths were set higher than 96 kHz.

9.5 Coherent, short-interval excitations-scheme-based NMR probes

The concept of coherent, short-interval excitations-based monitoring was further studied. The NMR samples in this operation scheme needed to be highly doped to achieve the required short T1 and T2 values. With such NMR samples, the influence of sample losses can no longer be neglected in SNR calculations. By utilizing larger sample dimensions, Δr, the otherwise expected reduction in SNR can be offset to a certain extent. Since greater magnetic losses owing to a larger sample volume reduce the SNR with a factor proportional to Δr^{-2} (cf. Eqs. 6.15 and 6.34), and since a larger diameter reduces the coil sensitivity by Δr^{-1} (cf. Eq. 6.19), the increase in signal amplitude, which is proportional to Δr^3 (cf. Eq. 6.15), becomes negligible in cases where sample losses dominate. Furthermore, larger sample sizes require shorter T1 relaxation times to fulfill the criterion of Eq. 6.13; this leads to a higher conductivity of the NMR samples. Therefore, a theoretical maximum exists for the achievable SNR with NMR probes that are based on coherent, short-interval excitations. This phenomena was simulated, and it was found that a sample dimension of $\sim$5 mm would deliver the maximum SNR (cf. Fig. 9.7). In these simulations, the optimal coil geometry was always resolved accordingly for each sample size. To simplify the simulations, the wire diameter and the filling factor were kept at constant values of 0.4 mm and 75%, respectively.

The optimal repetition rate and flip-angle combination was studied based on the T1 relaxation time of an NMR sample. Figure 9.8a shows the achievable transverse magnetization right before the next phase-coherent excitation pulse. Here, the values of T1 = 200 μs and T2* = 180 μs were applied. For a comparison, the level of achievable transverse magnetization based on the steady-state

free precession sequence with a perfect spoiling is shown in Fig. 9.8b. It was concluded from these simulations that an improvement of approximately 60% in SNR could be achieved with short-interval phase-coherent excitations. It is also important to note here that, in practice, perfect RF phase spoiling cannot be expected, and cases of destructive interference of the transverse magnetization may occur. The significance of the phase-coherent excitations is therefore further emphasized since it ensures the high SNR, which is required for robust field monitoring.

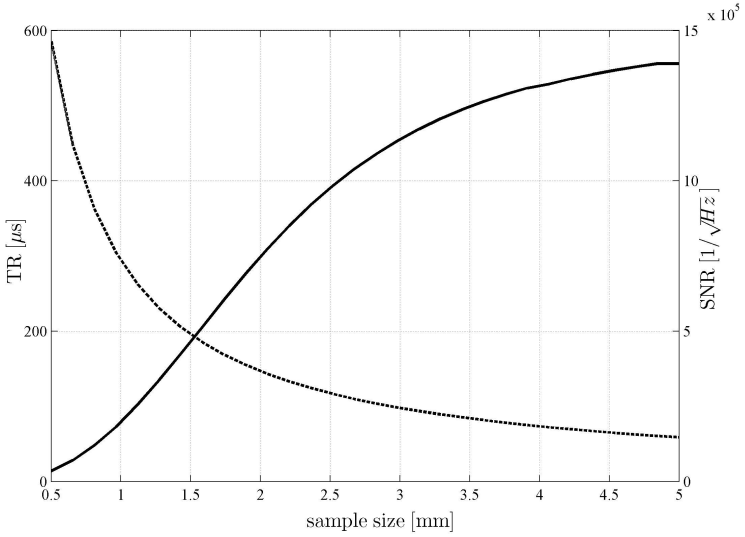

Fig. 9.7. *SNR plots of coherent, short-interval excitations-operated NMR probes with different sample sizes (solid line). The required TR ∼ T1 to fulfill the criterion based on Eq. 6.13 is also shown (dashed line). For each sample size, the optimal coil geometry was solved based on the preset properties of a 0.4-mm-diameter wire and a 75% filling factor.*

A single ^{1}H probe was manufactured to test the concept of coherent, short-interval excitations-based magnetic field monitoring. The transmit-receive electronics were based on the passive duplexer design, and the probe was operated with the feedback network described in Chapter 7. The 2.1-mm-long and 1.4-mm-diameter NMR sample was doped with $GdCl_3$ to adjust the T1 time to 280 μs. Based on the field-inhomogeneity simulations of Fig. 8.4, the T2* value of the sample was expected to be dominated by the intrinsic T2 of the doped sam-

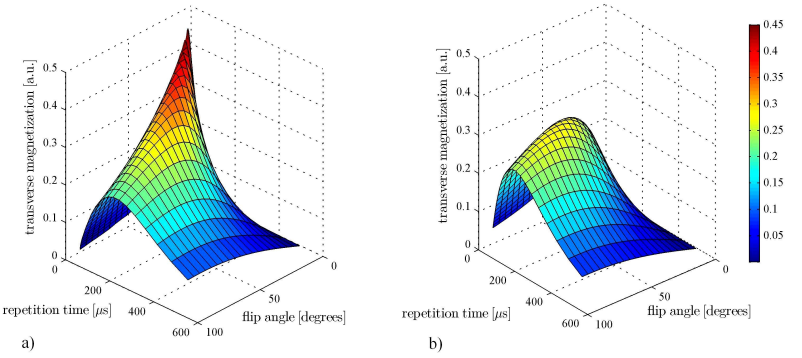

Fig. 9.8. *Steady-state transverse magnetization that is achievable right before a consecutive RF pulse, plotted as a function of applied repetition time and flip angle. Two cases are illustrated here: (a) NMR probes experiencing phase-coherent RF pulses and (b) a perfect spoiling of transverse magnetization before each consecutive pulse was expected.*

ple, i.e., 260 μs. The volume susceptibility of the doped sample was estimated to be +15 ppm with the $GdCl_3$ concentration corresponding to the given T1 time [54]. It was therefore estimated that such NMR probes would not introduce susceptibility artifacts to imaging as long as the probes were not placed directly in contact with the region of interest.

The monitored signal phase of a coherent, short-interval excitations-based NMR probe during a spiral sequence is illustrated in Fig. 9.9. The spiral sequence had the following parameters: 256-kHz bandwidth, 4 096 points, and 1.2-mm resolution. The NMR probe was placed in this experiment 20 cm away from the isocenter. As is seen from Fig. 9.9, steady-state transverse magnetization was achieved, and apart from the short 15-μs-long excitation periods occurring every 250 μs, continuous monitoring of the applied magnetic field was achieved. Based on the average SNR of 5.4×10^4 $\sqrt{\text{Hz}}$, a monitoring accuracy of 69 $\text{fT/Hz}^{3/2}$ was expected. This value fulfilled the precision requirement of 0.53 $\text{pT/Hz}^{3/2}$ that was derived in Chapter 3. In comparison to other NMR-based magnetometers that have been developed in this work, the acquisition lengths for static field measurements are no longer restricted by the signal T2* decay, and higher precisions in such measurements can therefore be achieved.

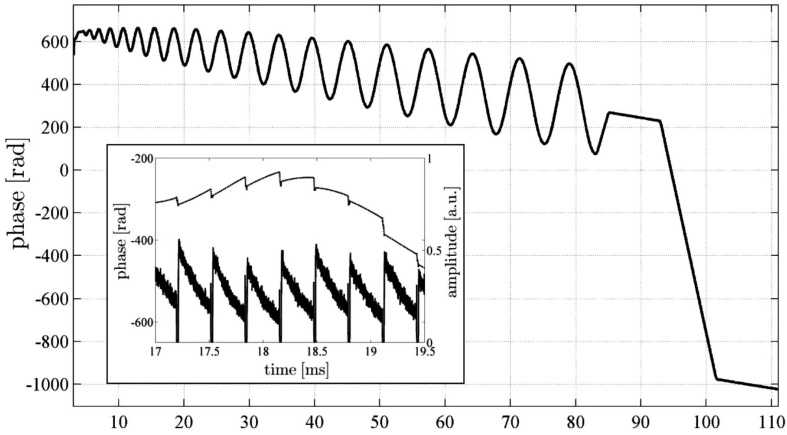

Fig. 9.9. *Signal amplitude and phase of a coherent, short-interval excitations-based NMR probe monitored during a single-shot spiral MRI acquisition. In the box, the unprocessed amplitude and phase signals are highlighted. The fact that it was possible to capture the crusher gradient applied at the end of the sequence indicates the advantage of this operation scheme.*

9.6 Application of NMR-probe-based magnetometers to magnetic field monitoring assisted MRI

9.6.1 Fast imaging acquisitions

For magnetic field monitoring assisted MRI experiments, a clinical MRI scanner (GE Signa 3.0 T, GE Healthcare, Milwaukee, WI, USA) was equipped with the developed receive-only ^{1}H NMR probes. Figure 9.10 illustrates a typical configuration of the magnetic field monitoring probes with a clinical eight-channel receiver array coil. Since, in this operation scheme, the system body coil was also utilized to excite the NMR probes, careful placement of the probes inside the excitation plane was required.

Images of a resolution phantom were acquired based on the spiral k-space trajectories. The monitored k-space locations were introduced into the gridding algorithm for improved image quality, as was explained in Chapter 1. The reconstructed images are shown in Fig. 9.11. In comparison to a standard two-dimensional Fourier-transform-based reconstruction, an improved image quality was observed. Hence, the application of NMR-based magnetometers for magnetic field monitoring assisted MRI was successfully verified.

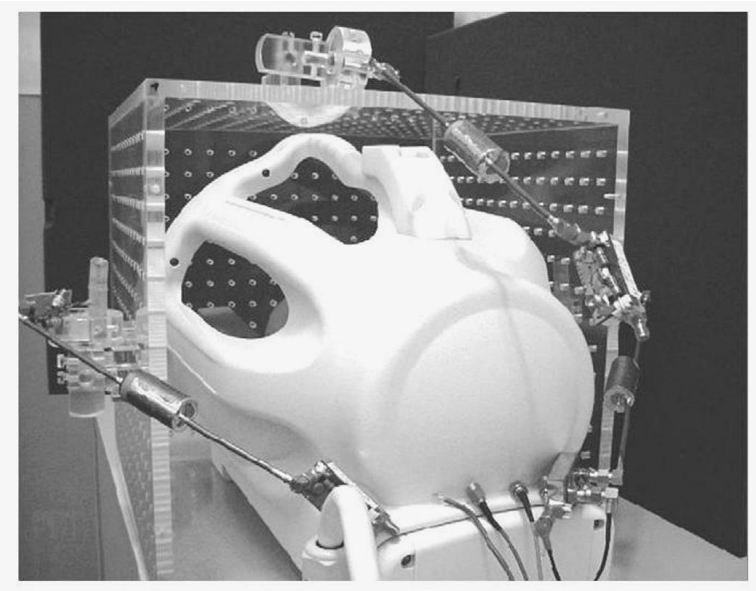

Fig. 9.10. *Magnetic field monitoring assisted MRI setup where four NMR probes are placed around an eight-element receive coil, and where a resolution phantom is placed inside the coil for imaging. In this particular setup with receive-only probes, one has to ensure the proper placement of the probes within the excitation plane.*

The high intrinsic SNR of the NMR probes ensured that the measurement precision was good enough despite the fact that the flip angles were optimized for imaging and not for achieving the 90° flip angles for the NMR probes. Since the imaging and the NMR probes were both based on ^{1}H nuclei, signal coupling could not completely be avoided. This was observed as an artifact in the bottom of Figs. 9.11c and 9.11d.

Similar to experiments with the receive-only ^{1}H NMR probes, transmit-receive ^{1}H NMR-probe-based magnetic field monitoring assisted MRI acquisitions were conducted. The monitored k-space trajectories of a spiral acquisition are plotted in Fig. 9.12. Here, the same imaging parameters were applied as were applied with the receive-only ^{1}H NMR probes. An improved image quality was achieved also in this case by introducing the field monitoring data into the gridding-based reconstruction (cf. Fig. 9.13). As was the case with the receive-only probes, coupling-based image artifacts were observable. The coupling artifacts were, however, not observed to be stronger with the transmit-receive probes than with the receive-only ones despite the fact that the transmit-receive probes

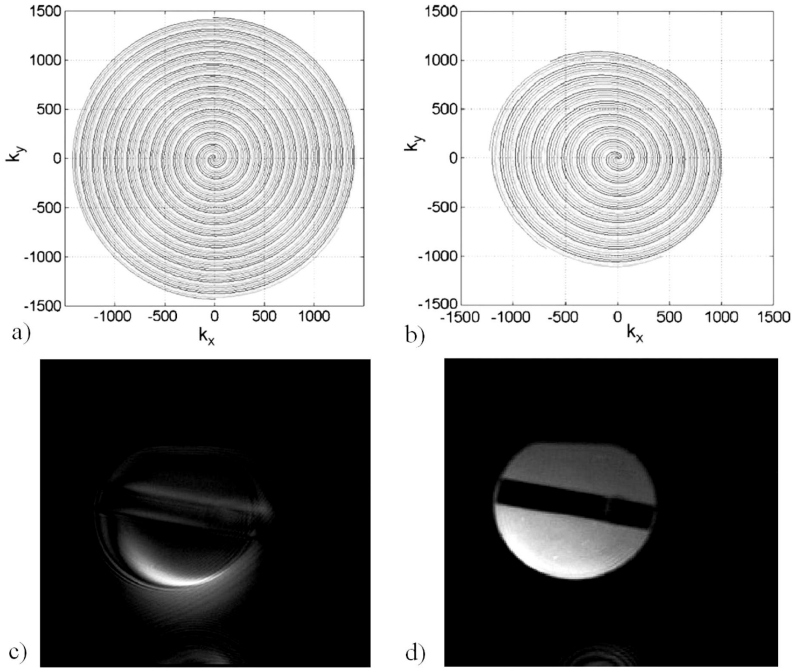

Fig. 9.11. *(a) Assumed and (b) measured multishot spiral k-space trajectories applied for reconstructing an image taken from a resolution phantom. Here, a spiral acquisition was applied with the following parameters: four arms, 8 192 points, and a bandwidth of 125 kHz. Noticeable skewing and amplitude compression were observed in the monitored k-space trajectories. These resulted in (c) a distorted MR image if ideal trajectories were assumed in the image reconstruction. It was possible to (d) restore the image quality if knowledge of actual gradient waveforms were implemented in the reconstruction.*

had higher signal levels owing to the optimal 90° flip angles. This observation was estimated to be an indication of the effectiveness of the counterwinding-based decoupling strategy that was utilized in the transmit-receive probes.

The type of image artifacts that are based on the probe-to-imaging coupling depends on the applied *k*-space trajectory. Figure 9.14 shows results of a circular echo planar imaging of a resolution phantom, where the acquisition is accompanied with the transmit-receive ^{1}H NMR probes for improved image quality. The corresponding *k*-space trajectory of the circular echo planar imaging is plotted in Fig. 9.15. From Fig. 9.14, one sees that the image artifacts from the ^{1}H probes

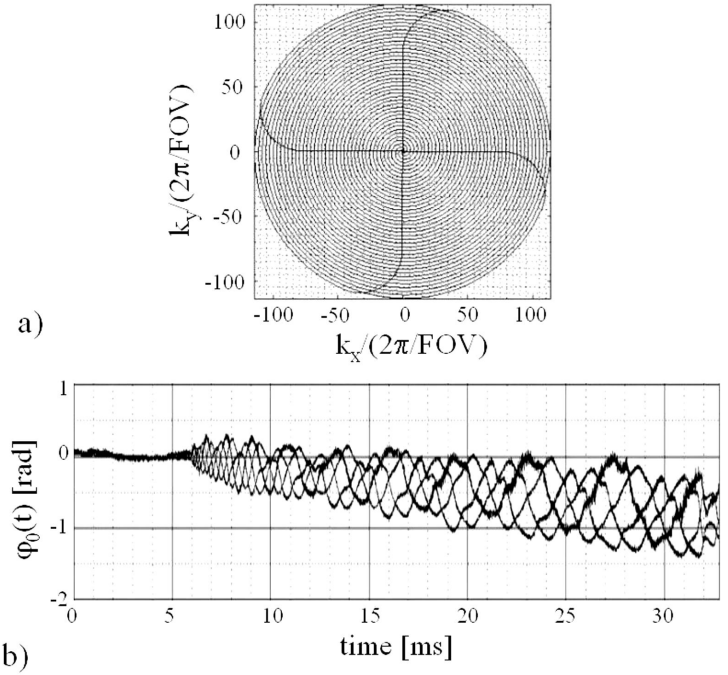

Fig. 9.12. *Acquired k-space trajectories for a four-arm spiral imaging presented with respect to (a) location in k space and (b) time. Here, the imaging parameters were the following: 16 arms, 8 192 points, and a bandwidth of 250 kHz.*

were spread along the phase-encoding axis owing to the incoherent excitations of the ^{1}H NMR probes.

Clearly, if such artifacts as shown in Fig. 9.14 overlap the region of interest in a clinical application, a reliable diagnosis would become either difficult or impossible to conduct. Figure 9.16 illustrates the significance of using non-proton-based NMR probes for preventing probe-based image artifacts. In these experiments, the trajectories of circular echo planar imaging were monitored precisely for improved image quality and without any interfering image artifacts.

9.6.2 Phase-contrast imaging

Phase-contrast imaging relies on high-amplitude bipolar gradient pulses to generate motion-related contrast between spins. The gradient pulses that are utilized

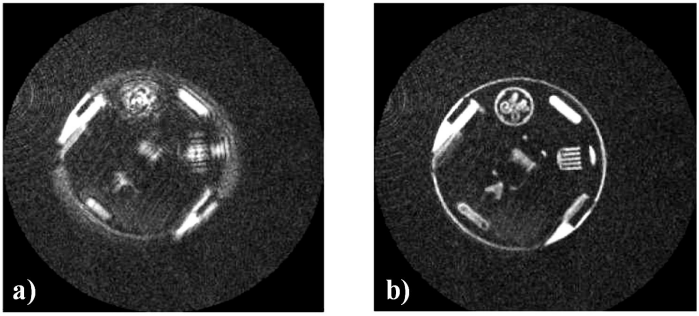

Fig. 9.13. *(a) MR image of a resolution phantom taken with a spiral sequence (bandwidth of 250 kHz, 8 192 points, and 16 arms) suffering from blurring and skewing artifacts resulting from nonideal gradient profiles. (b) The two-dimensional imaging assisted by four* ^1H *transmit-receive NMR probes to map the* k*-space trajectories for improved image quality. Here, an autofocus deblurring technique was also utilized for the reconstruction to correct the* B_0*-imperfection-related artifacts [150]. The coupling artifacts caused by the NMR probes should also be noticed here.*

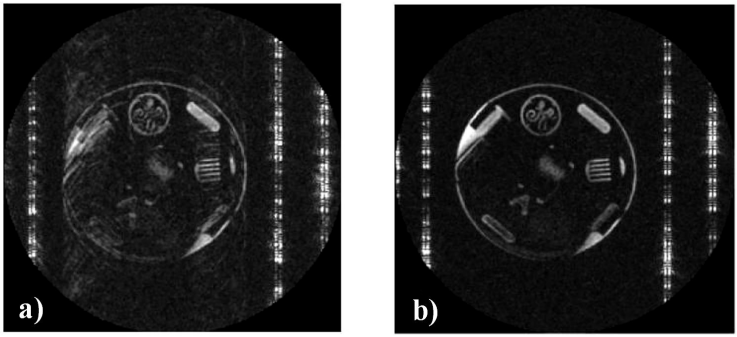

Fig. 9.14. *(a) MR image of a resolution phantom taken with a circular echo planar imaging sequence (bandwidth of 250 kHz, resolution of* 256×256*, and echo train length of 16) suffering from blurring and ghosting artifacts resulting from a nonideal gradient profile. (b) The two-dimensional imaging assisted by four* ^1H *transmit-receive NMR probes to map the* k*-space trajectories for improved image quality. The artifacts outside of the resolution phantom caused by the coupling of the NMR probes to the eight-channel receiver coil should be noted.*

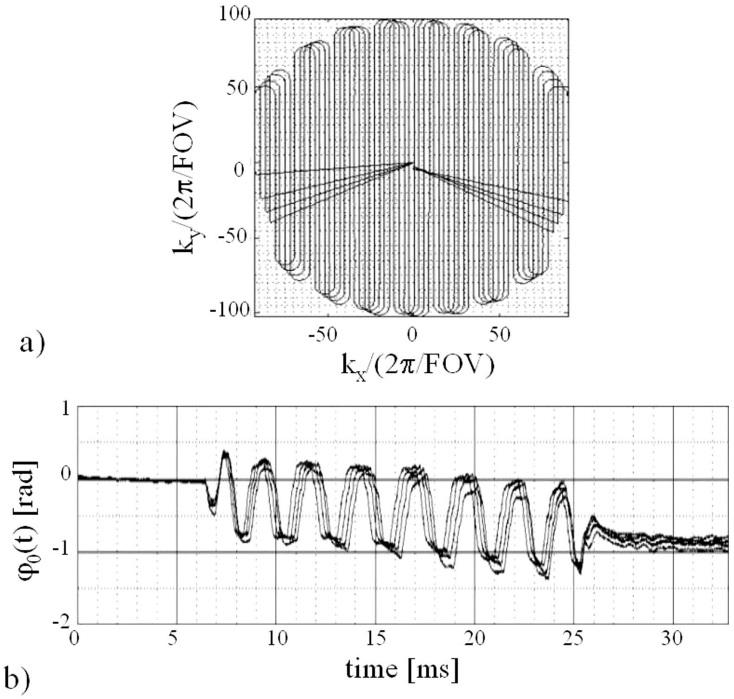

Fig. 9.15. *k-space trajectories acquired during a circular echo planar imaging acquisition presented with respect to (a) the location in k space and (b) time. The imaging parameters were the following: bandwidth of 250 kHz, resolution of* 256×256*, and echo train length of 16.*

for this purpose invoke strong eddy current responses, and velocity-encoding errors arise if the gradient envelopes of the bipolar pulses are not identical. Figure 9.17 shows results of an experiment in which a severe incoherency between the ideal and the actual field profiles existed. The actual fields were monitored with the transmit-receive ^{1}H NMR probes. It was observed that, especially at high ± 20 mT/m gradient amplitudes, the residual phase did not converge to zero as it was supposed to do. In addition, it was observed that the velocity encodings could not be reproduced accurately. Information on the actual magnetic field profiles was utilized for correcting the residual phase error, as shown in Fig. 9.18. It was diagnosed afterward that the nonideal gradient behavior was due to a damaged gradient amplifier. The experiments were repeated with the ^{2}H NMR

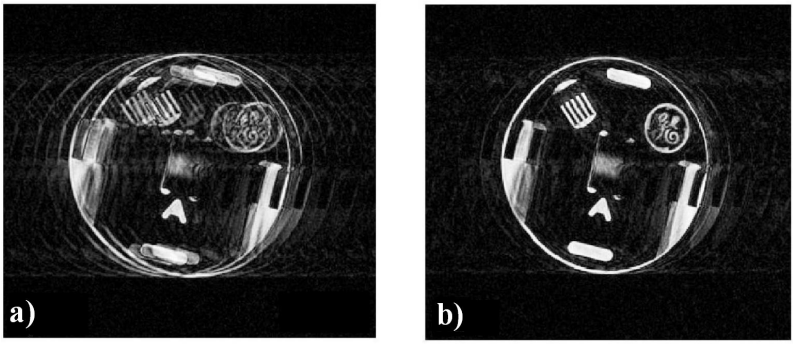

Fig. 9.16. *(a) MR image of a resolution phantom taken with a circular EPI sequence (bandwidth of 250 kHz, 8 192 points, and 16 arms) showing severe blurring and ghosting artifacts resulting from nonideal gradient profiles. (b) The two-dimensional imaging assisted by four ^2H transmit-receive NMR probes to map the k-space trajectories for improved image quality. As can be seen, no coupling between the NMR probes and the imaging coil was experienced.*

probes and in-specifications gradient hardware. It was found that improvements of an order of magnitude in the homogeneity of the phase encoding were still achievable with the help of magnetic field monitoring (cf. Fig. 9.19).

9.7 Discussion and conclusions

In this chapter, different techniques to utilize NMR probes for magnetic field monitoring assisted MRI have been studied. If an MRI scanner is equipped with a multichannel receiver, implementing a magnetic field monitoring system based on receive-only ^{1}H NMR probes becomes a straightforward procedure. The manufactured receive-only ^{1}H NMR probes showed a good SNR performance with a 80% match to the simulated values; this result indicates good applicability of the theoretical considerations that were applied in the design of the NMR probes. The difference in the SNR values were estimated to arise from the losses in the receiver chain that were not included in the simulations.

These NMR-probe-based magnetometer techniques were further developed to manufacture transmit-receive and ^{2}H-based non-proton-based NMR probes. The developed homemade transmit-receiver (cf. Chapter 7) was proven to be a suitable platform for operating NMR probes with high precision. It was shown that improved image quality in fast-acquisition and phase-contrast imaging experiments could be achieved with the help of magnetic field monitoring.

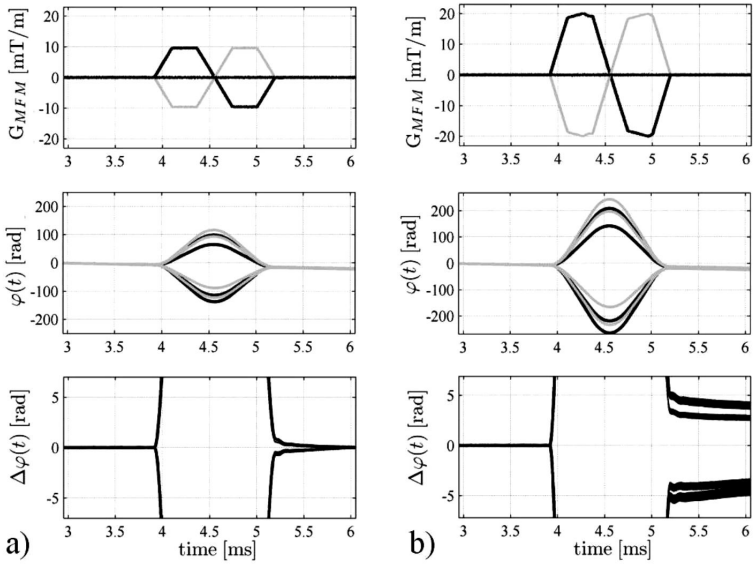

Fig. 9.17. *Velocity-encoding bipolar gradients with (a) ±10 mT/m and (b) ±20 mT/m amplitudes. Here, (top) gradient waveforms, (middle) absolute phase evolutions, and (bottom) relative phase evolutions with respect to a static field evolution are plotted. In both cases, eddy-current-related "tailing" was observable. In the experiments with the ±20 mT/m maximum gradient amplitude, it was also noticed that the waveforms could not be reproduced accurately.*

In all the MRI-related experiments, the manufactured receive-only ^{1}H probes, as well as the transmit-receive ^{1}H and ^{2}H probes, were operated based on the standard, long-interval excitations-based operation scheme. It was observed that the ^{1}H probes met the estimated precision requirement by more than an order of magnitude, and ^{2}H probes could fulfill this precision requirement as long as the applied ^{1}H-based MRI acquisitions have a bandwidth of 90 kHz or higher. At lower bandwidths, a maximum reduction of 8 dB with respect to the desired image-to-artifact ratio could be expected. In this context, it should be noted that lower imaging bandwidths also reflect linearly to lower gradient strengths and therefore to a more modest eddy current response. Thus, the fact that the SNR achieved with the manufactured ^{2}H NMR probes value is slightly below the desired value is deemed not to be critical.

All the manufactured NMR probes showed only a weak T2*-related signal decay with T2* values ranging from 100 to 200 ms. These results indicated a

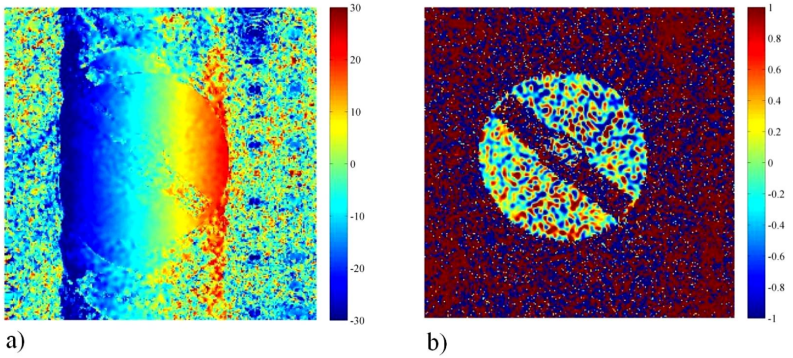

Fig. 9.18. *Phase maps of a static phantom after velocity encoding for phase-contrast imaging (VENC = 100 cm/s, G_{max} = 20 mT/m). (a) Owing to nonideal gradient waveforms, the phase distribution was corrupted. (b) With ^{1}H NMR-probe-based magnetic field monitoring, the phase distribution over the image was restored toward the desired value of zero.*

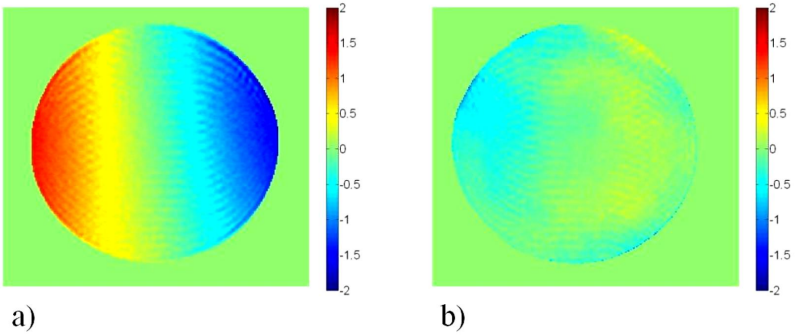

Fig. 9.19. *Phase maps over a static phantom after velocity encoding in phase-contrast imaging (VENC = 20 cm/s, G_{max} = 20 mT/m). (a) Owing to nonideal gradient waveforms, the phase distribution was corrupted. (b) With ^{2}H NMR-probe-based magnetic field monitoring, the phase distribution over the image was restored toward the desired value of zero.*

good functionality of the susceptibility-matching techniques that were applied, and they verified that the developed NMR probes could be utilized to monitor any existing MRI acquisition, regardless to the length of their acquisition windows.

The lower resolution limit for an MRI acquisition that can be accompanied with magnetic field monitoring depends on the sample size and the gyromagnetic ratio of the utilized NMR probes. With the manufactured transmit-receive ^{1}H and ^{2}H NMR probes, these resolution limits were 0.45 and 0.15 mm, respectively. The high SNR of ^{1}H NMR probes could be traded for lower applicable imaging resolutions to some extent. However, high filling factors are in practice difficult to achieve with ^{1}H probes with small sample diameters, and therefore it is more favored to utilize ^{2}H probes for high-resolution imaging owing to the lower gyromagnetic ratio of these.

The concept of a novel operation scheme based on coherent, short-interval excitations was proven with a single ^{1}H NMR probe. In the experiment, the magnetic field profile of an applied spiral fast-acquisition sequence was monitored with good precision. The fact that it was possible to capture the crusher gradients applied at the end of the spiral sequence indicated especially the significance of this operation scheme. The limited number of advanced feedback-based RF channels that were available, as well as the high coupling between the utilized ^{1}H probes and the imaging coil, prevented the performance of simultaneous ^{1}H image acquisitions. For future work, more NMR probes based on coherent, short-interval excitations should be manufactured and the feedback scheme should be modified for operating non-proton-based NMR probes. The latter can be easily achieved by changing the amplifiers and the bandpass filters in the feedback network.

The suitability of the different NMR-based techniques for clinical applications is further discussed here. A magnetic field monitoring system based on receive-only ^{1}H NMR probes is estimated to be feasible only for MRI acquisitions with volume excitations since placing NMR probes within an excitation plane of an imaging object can be a very delicate process. Three-dimensional imaging and separate calibration scans are application examples in which receive-only probes could still be feasible. Despite the counterwindings-based decoupling technique, the manufactured transmit-receive ^{1}H probes showed noticeable coupling artifacts to ^{1}H imaging. Therefore, this design is also considered to be less attractive for clinical applications.

With ^{2}H probes, the coupling to imaging can be completely eliminated. Further benefits of ^{2}H probes over ^{1}H probes are their reduced sensitivity to susceptibility mismatches and the ease at which they can be miniaturized for high-resolution imaging. A drawback of this scheme is a slightly lower baseline SNR than is achieved with ^{1}H NMR probes.

The operation scheme based on the standard, long-interval excitations is not deemed to be suitable for clinical applications since NMR probes based on this scheme cannot be optimized simultaneously for both short- and for long-

acquisition windows. However, significantly higher robustness against imaging parameters, such as resolution and repetition time, is achieved with the novel operation scheme based on coherent, short-interval excitations. With this scheme, NMR sample sizes can be increased for a higher SNR, and susceptibility-matching techniques can be omitted for simpler probe manufacturing. Since RF excitation pulses with this operation scheme are applied also during the MRI signal reception, efficient decoupling with imaging coils is compulsory. It is proposed here that sufficient coupling can be achieved with non-proton-based probes and narrow band-pass filtering of the transmission pulses.

10

Conclusions and Future Perspectives

Spatial, flow, and diffusion encodings in MRI are based on precisely applied magnetic field gradients. Imperfections in these magnetic field profiles can severely degrade image quality in MRI. This is especially the case with various novel MRI applications such as fast-acquisition, phase-contrast, and diffusion-tensor imaging. Artifacts in images arise as a result of eddy currents, imprecise gradient waveforms, asymmetric timing delays in applying waveforms, and drifts in environmental constants such as temperature. Improving gradient fidelity in these novel MRI applications could have a significant impact on patient throughput and quality of diagnosis in everyday clinical use.

Utilizing a dedicated magnetometer system to monitor real-time MR image-encoding gradients, and applying the information for specialized image reconstruction is proposed to tackle the described shortcomings of the present-day gradient hardware. Unlike gradient calibration methods, field monitoring does not lengthen image acquisitions, nor is it vulnerable to parameter drifts between calibration scans. Unlike gradient current monitoring and feedback-based active compensation techniques, which are used in present-day MRI scanners, magnetic field monitoring offers higher precision and better spatial selectivity and does not rely on potentially incomplete models for the response function of the gradient system.

Estimates for performance requirements for such a field monitoring system have been formulated in this work. A general derivation for the monitoring precision is difficult to make because the image sensitivity to gradient errors varies from MR application to application. In this work, typical signal-to-noise ratio levels experienced in MRI are reflected to determine the minimum ratio between the signal and the induced errors by gradient imperfections. For simulating the level of image artifacts, the echo planar imaging trajectory has been chosen in

this work owing to its popularity as a fast acquisition scheme, as well as its high sensitivity to gradient imperfections.

The high sensitivity of the MRI acquisition relates directly to strict performance requirements for magnetometers suitable for magnetic field monitoring assisted MRI. It is estimated that spatiotemporal magnetic flux densities are to be measured with <3 nT/$\sqrt{\text{Hz}}$ noise density at a maximum gradient swing of ± 50 mT at a background flux density of ≥ 1 T. As MR image encoding is based on the time integral of an applied gradient field, MRI is particularly sensitive to errors related to magnetic field drifts. Thus, in the context of magnetic field monitoring, potential noise in measured signals gets further amplifier; a highly undesired characteristic for candidate magnetometers.

Additional design considerations should also be included when choosing appropriate magnetometer techniques for the described application. The utilized magnetic field monitoring system should not deteriorate or in any other way interfere with standard imaging. Hence, the level of electromagnetic interference at the applied imaging band(s) should be restricted below the noise level of MRI acquisition. To avoid susceptibility-related artifacts in images, the materials utilized in the sensors are must be susceptibility matched relative to biological tissue to within 10-25 ppm, depending on the sensor size. Furthermore, features such as low cost and straightforward parallel operation with existing clinical MRI scanners are desired. These two latter criteria bias the research toward well-established magnetometer technologies.

The majority of existing magnetometer technologies can be eliminated as candidates because they are not sensitive enough (e.g., Hall-effect-based, MEMS, and optical sensors), are ferromagnetic (e.g., flux-gate and magnetoresistive sensors), or are too complex as well as too expensive to be feasibly implemented for the application (e.g., optically pumped sensors and SQUIDs). Pick-up coils do not have these drawbacks in principle, however, theoretical calculations made in this work show that the intrinsic $1/f$ noise of the pick-up coil-based magnetometers makes these sensors also less suitable for magnetic field monitoring assisted MRI. The experimental results obtained in this work further support this prediction. However, the conducted experiments also show that beyond the $1/f$ noise regime, the spectral SNR is close to fulfilling the derived precision requirement for accurate field monitoring.

Electron paramagnetic resonance sensor technology is based on nonmagnetic materials, is estimated to have the desired precision, and does not suffer from $1/f$ noise. The technology would therefore be well suited for magnetic field monitoring assisted MRI. However, it is estimated that the high operational frequencies of EPR sensors at strong background field strengths experienced in present-day clinical MRI scanners (up to 100 GHz) would make the technology

difficult to implement and economically unfeasible. In contrast, NMR probes, whose nuclei have gyromagnetic ratios several orders of magnitude lower, are operated at RF frequencies for which cost-effective electronic components are available. As NMR probes are also reported to offer a precision that fulfills the derived requirements and no $1/f$ noise, the technique is identified to be the most suitable solution for magnetic field monitoring in MRI.

The free-induction decay signal of an excited spin ensemble is monitored after an initiating RF pulse in a typical magnetic field monitoring scheme using miniaturized NMR probes. Here, the phase evolution of the signal relates to the time envelope of the monitored magnetic field at the location of the NMR probe. A configuration of at least four distributed NMR probes can be used to map the time-dependent, spatially constant, and three-dimensional linear terms of a temporal magnetic field. This first-order approximation is considered to be sufficient to capture the dominant image-encoding artifacts. However, further improvements are achieved by measuring higher spatial orders with higher sensor counts [36].

NMR probes also offer highly accurate static magnetic field mapping as long as the intrinsic chemical shifts of the spin ensembles are first calibrated. The reliability of such measurements from the perspective of clinical, real-time magnetic field monitoring can be questioned however, as the patients themselves induce B_0 disturbances at a level of magnitude relevant for MRI. Accurate mapping of intrabody B_0 inhomogeneities experienced close to large air cavities, such as lungs, ears, nose, and mouth, are also beyond the capabilities of magnetic field monitoring techniques. Diamagnetic patches, as proposed in [17], can be utilized to resolve these issues of static B_0 inhomogeneity to some extent. However, this method has its drawbacks with respect to patient comfort and countering B_0 inhomogeneities owing to unaccessible air cavities such as lungs or the inner ear. It should be noted, however, that the magnetic field monitoring hardware in the absence of a patient can be utilized for static B_0 mapping without the aforementioned drawbacks. Performing a calibration measurement is one such application.

The NMR probe construct chosen for this work consists of an NMR sample, e.g., a water droplet, around which a solenoidal RF coil is wound for signal detection. Two physical factors affect the speed at which the signal dephases, and this necessitates a careful choice of NMR probe geometry and design. First, a background field inhomogeneity over the sample can lead to unacceptably low signal levels within one encoding instance. The longest read-out windows of MRI acquisitions are roughly 100 ms long, and corresponding T2* values or longer windows for NMR probes can be achieved with delicate susceptibility-matching techniques. Second, magnetic-field-gradient-induced dephasing can be

limited by restricting the sample size to be no larger than half the applied imaging resolution if NMR probes and image acquisition are based on the same nuclei. In the case of NMR nuclei with lower gyromagnetic ratio, this criterion becomes relaxed.

Different susceptibility-matching techniques have been studied in this work for NMR probes based on the described standard, long-interval excitations scheme. By omitting the sample capillaries, thus casting the coil and the sample space directly into the susceptibility-matched epoxy casing, increased filling factors are achievable for higher SNR. The technique, however, is sensitive to any impurities introduced close to or within the NMR sample. In addition, measures to deal with the hygroscopic nature of epoxy must be countered to preserve long operating times. Higher robustness against impurities and better manufacturing yield are achieved if physical plugs in the direction of the cylinder symmetry axis are omitted and the sharp drop-off in the sensitivity of a solenoid coil is exploited to constrain the effective sample size. The sensitivity-profile-based spatial selectivity does not match physical plugs, and typically applicable imaging resolutions are lower with this NMR probe design. For high-resolution imaging, the steepness of the sensitivity drop-off can be further enhanced by applying excitation pulses with larger than (nominal) 90° angles.

As an alternative to the described susceptibility matching methods, (indefinitely) long read-out times and strong robustness to a variety of applied field gradients can be achieved if probes are operated based on coherent, short-interval excitations. The approach ensures high SNR if the repetition time applied in MRI acquisitions becomes significantly shorter than the T2* value of the probes [6]. To avoid destructive interference of residual and newly excited magnetization, this approach requires a sophisticated feedback mechanism to align the phase of the RF excitation pulses with the phase of the residual magnetization. Hence, it is not necessary to adopt gradient spoiling at the end of every applied repetition to suppress any residual spin magnetization. With this novel scheme, increased robustness to susceptibility-related dephasing is also obtained, and the susceptibility-matching techniques can be omitted in practice.

The decoupling requirement of NMR probes to a standard MRI acquisition can be tackled by utilizing probes that are based on a nucleus different from for imaging itself (typically ^{1}H). This technique is shown with ^{2}H probes to be superior in comparison to counterwound coils, providing only moderate decoupling, and to RF shields, which distort the measured fields and potentially jeopardize imaging quality and patient safety. An additional advantage of non-proton-based probes with their lower gyromagnetic ratio is that larger applicable sample sizes simplify probe manufacturing, reducing sensitivity to sample impurities (e.g., air bubbles) and enabling higher filling factors for higher effective

SNR. These properties become especially beneficial if the probes are applied for high-resolution and nonproton imaging, and if the probes are placed in areas with poorer background field inhomogeneity (e.g., if the probes are integrated into imaging coils or patient tables). In this work, theoretical considerations are also derived to show that, with the right probe design, the SNR is only slightly impacted by the lower gyromagnetic ratio. The advantages of nuclei with lower gyromagnetic ratio, apart from reduced signal coupling, become less significant if the coherent, short-interval excitations-based operating scheme is utilized.

NMR magnetometers based on ^{1}H and ^{2}H nuclei have been further studied in practical experiments. The benefit of ^{1}H nuclei is that very good SNR values are achieved because of the high gyromagnetic ratio. The advantage of ^{2}H nuclei is that they practically eliminate coupling to MRI acquisitions. Despite the lower SNR achieved with ^{2}H probes, sensors can provide accurate field monitoring down to ^{1}H imaging resolutions of 0.15 mm. The performance characteristics of the magnetometers constructed in this thesis, including the pick-up coils, are summarized in Tab. 10.1.

The concept of improving MR image quality with real-time magnetic field monitoring is proved by fast-acquisition schemes such as spiral and (circular) echo planar imaging. These experiments show that gradient-error-related artifacts in MR images can be significantly reduced with magnetic field monitoring. It is also shown that the gradient imperfection induced errors in the velocity encoding of phase-contrast imaging experiments can be suppressed by approximately one order of magnitude. The novel excitation scheme based on coherent RF pulses to generate continuous monitoring data, regardless of applied imaging parameters, is proven successfully by accurately monitoring a single-shot spiral sequence with an ^{1}H NMR probe. The fact that strong crusher gradients at the end of the acquisition were also mapped highlights the significance of this technique.

Several possibilities exists for the placement of NMR probes inside the magnet bore of a MRI scanner. Placing NMR probes on the patient would potentially introduce undesired complexity into standard clinical workflow, although this offers the additional opportunity of motion correction [37]. Having probes integrated into a patient table and a magnet bore is seen challenging, since the level of spatial nonlinearities in the image-encoding fields and the accompanying eddy current fields increase drastically outside the maximum field of view. Extrapolating the monitoring data from sensors placed far away from the isocenter could lead to systematic errors in correcting gradient waveforms.

NMR probes can be integrated into imaging coils. However, if flexible coils, e.g., torso arrays, are utilized, but one needs to ensure that the probe locations do not shift during imaging, as a result of patient movement. On the other hand,

Sensor type	Principle of operation	Precision	^{1}H imaging resolution	Further notes
pick-up coils	analog integration	6.3 nT/$\sqrt{\text{Hz}}$	no limit	high $1/f$ noise, unlimited TR range
^{1}H probes	receive-only, standard long-interval excitations	23 fT/Hz$^{3/2}$	>0.5 mm	restricted placement, moderate coupling, limited TR range
	transmit-receive, standard long-interval excitations, counterwindings	68 fT/Hz$^{3/2}$	>0.45 mm	low coupling, limited TR range
	transmit-receive, coherent short-interval excitations	69 fT/Hz$^{3/2}$	no limit	high coupling, unlimited TR range
^{2}H probes	transmit-receive, standard long-interval excitations	1.4 pT/Hz$^{3/2}$	>0.15 mm	no coupling, limited TR range

Table 10.1. *Summary of the different magnetometer techniques that have been developed in this work including the relevant characteristics for magnetic field monitoring assisted MRI. For pick-up coils, the precision is given with units of T/$\sqrt{Hz}$. With NMR-based techniques, it is more appropriate to discuss with T/Hz$^{3/2}$. For pick-up coils, the sensing bandwidth should match or exceed the Nyquist limit of the gradient activity (i.e., 50 kHz). With NMR probes lower bandwidths can be chosen for higher SNR as long as the monitoring rate matches the imaging sampling rate.*

it is possible to distinguish motion artifacts from eddy-current-related effects by having redundancy in the number of probes and by placing one subset of the probes in fixed locations.

Having a separate multinuclear NMR transmit-receiver, instead of utilizing the capabilities offered by a clinical MRI scanner, brings certain advantages. With such hardware, none of the expensive RF channels of an MRI system are consumed but the data acquisition hardware can be more cost-effectively tailored for NMR probes alone. With a separate transmitter, excitation pulses providing optimal flip angles for NMR probes are delivered regardless of imaging parameters. Non-proton-based probes as well as the coherent, short-interval excitations-

based operation scheme become also straightforward to implement with such a system design.

The developed transmitter, utilizing hard pulses with short durations, offers wideband excitations adequate for operating NMR probes at clinical background magnetic flux densities of up to 4.7 T, regardless of the relevant NMR nuclei chosen. Operations at higher field strengths are easily enabled by either frequency multipliers or frequency mixers. Alternatively, the hard-pulse transmitter can be omitted and a positive-feedback loop can be introduced individually to each receiver channel. With this excitation scheme, one ensures phase coherency between the spin ensemble and the RF excitation pulses as long as the RF-pulse width is kept short. The most significant advantage of this developed excitation scheme is that functionality of NMR-probes is not anymore hindered by applied MRI acquisition parameters such as resolution or repetition rate. High power levels are required with this excitation scheme to flip the spins in a very short time period ($1-10\ \mu s$). This is achieved with the positive-feedback loop, which gives to the RF-signal for spin excitation an exponential growth. As an intriguing feature of this method, no additional signal sources, e.g. local oscillators and RF amplifiers, are requirede but the design relies alone on the signal from the NMR ensemble. Therefore, the feedback circuitry can be miniaturized to an extent where it takes place at the probe itself or in the intermediate vicinity (i.e., inside the magnet room).

Federal limits for SAR constrain the applied RF power levels for any MR excitation pulses, and therefore these limits should also be considered when designing NMR-based field monitoring system. The most stringent SAR limit for tissue heating is for the head area and is set to 3.2 W/kg. This value is orders of magnitude larger than can be expected to be induced to a patient by an NMR-probe-based magnetic field monitoring system, regardless of the chosen RF excitation scheme. Therefore, it is concluded that an active SAR monitoring, which is typical for volume coils, does not have to extend to the magnetic field monitoring system.

The novel multinuclei NMR receiver developed in this work is based on the direct-conversion topology, as opposed to typical, heterodyne topology-based, MRI receiver designs. The direct-conversion-based receivers offer certain benefits such as a simpler hardware implementation and the option of having multiple signal bands on a single physical channel. The latter feature has been exploited in this work to show that a single channel of the developed receiver can be utilized for simultaneous multiband acquisitions, and with comparable SNR performance to a clinical MRI scanner. The increased costs associated with higher sampling rate analog-to-digital converters as well as the more intense digital signal processing required are seen as the only drawbacks of the direct-conversion

receiver topology. However, because no expensive local oscillators for NMR probes are required, the total costs are partly compensated. Furthermore, it is predicted that the cost of high-speed analog-to-digital converters will be reduced in the future as the technology to manufacture semiconductor devices continues to progress. Implementing time-efficient digital signal processing algorithms and utilizing high-speed signal processors are proposed for handling the larger data sets experienced with this receiver technique.

Based on the promising results shown in this work, it is expected that real-time magnetic field monitoring in MRI can greatly increase interest in using fast-acquisition techniques for clinical purposes and improve the accuracy of diagnosis in flow and diffusion-tensor imaging. Fast acquisitions are especially foreseen to reduce the high cost of MRI per scanned patient, an issue that afflicts MRI technology in comparison to many other imaging modalities. A drawback of real-time magnetic field monitoring, in comparison to gradient calibration methods for example, is that the total MRI system complexity and manufacturing costs are increased. The increased number of RF receiver channels required for the system can be limited by applying a direct-conversion-based receiver topology for simultaneous acquisition of multiple frequency bands [143, 119]. For example, signals from a single ^{1}H MRI-coil element and a single non-proton NMR-probe could share the same physical channel in this implementation.

It is expected that NMR-based magnetic field monitoring cannot penetrate everyday clinical use without utilization of the developed novel phase-coherent excitation scheme. This is because otherwise the performance of NMR-based field monitoring system could be significantly degraded by the applied gradient profiles and imaging repetition rates. Future work should therefore focus on manufacturing more such probes for (*in vivo*) experiments. Tackling the issues with RF-signal coupling is another important aspect and potentially suitable non-proton nuclei should be studied to ensure sufficient level of signal decoupling. Compared to the standard, long-interval excitations scheme, nuclei with a relatively low gyromagnetic ratio, e.g. ^{2}H, may no longer be as advantageous. The challenge of nuclei with low gyromagnetic ratio is that the excitation pulses become inefficient, and higher power levels are required to achieve large flip angles within the required short time intervals. A more economically feasible solution is expected to be achieved with ^{19}F nuclei having a gyromagnetic ratio of 40.06 MHz/T. Such an approach would require further research to find a molecule or chemical solution with high ^{19}F spin density, a T1 value below 1 ms, and a T2 value as close to T1 as possible. Also, because of the proximity of the signal bandwidths of ^{19}F and ^{1}H nuclei, negligible coupling to imaging coils should be verified in practice. On the other hand, the demanding challenges of probe miniaturization and susceptibility matching, which are faced with NMR-probes

based on the standard, long-interval excitation scheme, are not considered to be relevant with the coherent, short-interval excitation scheme. This conclusion has already been verified to a large degree by the conducted experiments with ^{1}H nuclei.

Magnetic-field-monitoring is expected to enable more accurate feedback for the gradient drivers, a technique that is now implemented indirectly by measuring the currents fed to the gradient coils and relying on system response models. The introduction of field monitoring could potentially reduce the high-fidelity requirements of the gradient systems and therefore lead to cost savings, especially in gradient drivers. Similar feedback techniques can be applied for automatic control of the active B_0 and gradient shim coils as well, a novelty that would benefit not just imaging experiments but also installation and maintenance operations. It is clear that these are promising research fields and should be further explored in the future.

EMR-based sensors are reported to have a precision close to what is desired for accurate magnetic field monitoring in MRI. EMR-elements and Wheatstone-bridge-based read-out electronics can be manufactured very inexpensively and the technique therefore offers a sound alternative to NMR probes. At the moment the technology is in a young stage and some time is needed before the technology matures and sensors become commercially available. The biggest challenge for the technology is the noise level at lower frequencies (i.e., random walk), and this topic would need to be carefully studied.

Clinical *in vivo* studies should be one important aim of further work. An approval from federal authorities is required first before such studies can be conducted. Studies of applying magnetic field monitoring can be expanded from standard and phase-contrast imaging, which have already been shown feasible in this work, to enable NMR-probe-based motion correction and controlling accuracy of parallel excitation pulses [151]. Integrating magnetic field monitoring hardware in a clinical MRI coil is a technological novelty that should be shown *in vivo* also. Furthermore, the potential of coherent RF excitations should be studied also for MRI applications since this can offer increased SNR and an additional contrast parameter, and can make the utilization of spoiler gradients obsolete.

Introduction of an integrated magnetic field monitoring system to a clinical MRI scanner would be more straightforward if existing MRI receivers are upgraded to utilize multiband receiver techniques based on digital direct sampling and multiband RF front-ends. Adaptation of the technology would eliminate the need for separate RF channels for the magnetic field monitoring system. A further, more significant benefit of this receiver technique is that one could utilize frequency-domain multiplexing to reduce the number of physical ^{1}H receiver

paths. Work is still, however, needed to optimize the digital signal processing in a way that compromises neither MRI acquisition lengths nor SNRs.

This concludes the work on studying the capabilities of magnetic field sensing to improve image quality in MRI.

References

1. I. I. Rabi, J. R. Zacharias, S. Millman, and P. Kusch, "A new method of measuring nuclear magnetic moment," *Physical Review*, vol. 53, p. 318, 1938.
2. E. L. Hahn, "NMR and MRI in retrospect :discussion," *Philosophical Transactions: Physical Sciences and Engineering*, vol. 333(1632), pp. 403–411, 1990.
3. D. W. McRobbie, E. A. Moore, M. J. Graves, and M. R. Prince, *MRI from picture to proton*. Cambridge University Press, 2003.
4. R. H. Hashemi, W. G. Bradley, and C. J. Lisanti, *MRI: The Basics*. Lippincott Williams & Wilkins, Philadelphia, 2004.
5. M. O'Donnell and W. A. Edelstein, "NMR imaging in the presence of magnetic field inhomogeneities and gradient field nonlinearities," *Medical Physics*, vol. 12, pp. 20–26, 1985.
6. M. A. Bernstein, K. F. King, and X. J. Zhou, *Handbook of MRI Pulse Sequences*. Elsevier Academic Press, Burlington, MA, 2004.
7. C. B. Ahn, J. H. Kim, and Z. H. Cho, "High-speed spiral scan echo planar NMR imaging," *IEEE Transactions on Medical Imaging*, vol. 5, pp. 2–7, 1986.
8. E. L. Hahn, "Spin echoes," *Physical Review*, vol. 80, pp. 580–594, 1950.
9. G. Wider, V. Dotsch, and K. Wuthrich, "Self-compensating pulsed magnetic-field gradients for short recovery times," *Journal of Magnetic Resonance A*, vol. 108(2), pp. 255–258, 1994.
10. A. L. Alexander, J. S. Tsuruda, and D. L. Parker, "Elimination of eddy current artifacts in diffusion-weighted echo-planar images: The use of bipolar gradients," *Magnetic Resonance in Medicine*, vol. 38(6), pp. 1016–1021, 1997.
11. X. J. Zhou, S. G. Tan, and M. A. Bernstein, "Artifacts induced by concomitant magnetic field in fast spin-echo imaging," *Magnetic Resonance in Medicine*, vol. 40(4), pp. 582–591, 1998.
12. T. G. Reese, O. Heid, R. M. Weisskoff, and V. J. Wedeen, "Reduction of eddy-current-induced distortion in diffusion MRI using a twice refocused spin echo." *Magnetic Resonance in Medicine*, vol. 49(1), pp. 177–182, 2003.

13. A. J. Powell and T. Geva, "Blood flow measurement by magnetic resonance imaging in congenital heart disease," *Pediatric Cardiology*, vol. 21, pp. 47–58, 2000.
14. A. Chernobelsky, O. Shubayev, C. R. Comeau, and S. D. Wolff, "Baseline correction of phase contrast images improves quantification of blood flow in the great vessels," *Journal of Cardiovascular Magnetic Resonance*, vol. 9, pp. 681–685, 2007.
15. P. Mansfield, "Multi-planar image formation using NMR spin echoes," *Journal of Physics C: Solid State Physics*, vol. 10, pp. 55–58, 1977.
16. F. Romeo and D. I. Hoult, "Magnet field profiling: analysis and correcting coil design," *Magnetic Resonance in Medicine*, vol. 1(1), pp. 44–65, 1984.
17. J. L. Wilson, M. Jenkinson, and P. Jezzard, "Optimisation of static field homogeneity in human brain using diamagnetic passive shims," *Magnetic Resonance in Medicine*, vol. 48(5), pp. 906–914, 2002.
18. P. Mansfield and B. Chapman, "Active magnetic screening of coils for static and time-dependent magnetic field generation in NMR imaging," *Journal of Physics E: Scientific Instruments*, vol. 19(7), pp. 540–545, 1986.
19. D. J. Jensen, W. W. Brey, J. L. Delayre, and P. A. Narayana, "Reduction of pulsed gradient settling time in the superconducting magnet of a magnetic resonance instrument," *Medical Physics*, vol. 14(5), pp. 859–862, 1987.
20. R. J. Ordidge and I. D. Cresshull, "The correction of transient B0 field shifts following the application of pulsed gradients by phase correction in the time domain," *Journal of Magnetic Resonance*, vol. 69(1), pp. 151–155, 1986.
21. G. H. Glover and E. Schneider, "Three-point dixon technique for true water/fat decomposition with B0 inhomogeneity correction," *Magnetic Resonance in Medicine*, vol. 18(2), pp. 371–383, 1991.
22. P. Gurney, J. M. Pauly, and D. G. Nishimura, "A simple method for measuring B0 eddy currents," *Proceedings of International Society for Magnetic Resonance in Medicine*, vol. 13, p. 866, 2005.
23. A. Takahashi and T. Peters, "Compensation of multi-dimensional selective excitation pulses using measured k-space trajectories," *Magnetic Resonance in Medicine*, vol. 34(3), pp. 446–456, 1995.
24. G. F. Mason, T. Harshbarger, H. P. Hetherington, Y. Zhang, G. M. Pohost, and D. B. Twieg, "A method to measure arbitrary k-space trajectories for rapid MR imaging," *Magnetic Resonance in Medicine*, vol. 38(3), pp. 492–496, 1997.
25. J. H. Duyn, Y. Yang, J. A. Frank, and J. W. van der Veen, "Simple correction method fork-space trajectory deviations in MRI," *Journal of Magnetic Resonance*, vol. 132, pp. 150–153, 1998.
26. P. Jezzard, A. S. Barnett, and C. Pierpaoli, "Characterization of and correction for eddy current artifacts in echo planar diffusion imaging," *Magnetic Resonance in Medicine*, vol. 39, pp. 801–812, 1998.
27. M. Beaumont, L. Lamalle, C. Segebarth, and E. L. Barbier, "Improved k-space trajectory measurement with signal shifting," *Magnetic Resonance in Medicine*, vol. 58(1), pp. 200–205, 2007.
28. S. M. Lechner, P. Sipilae, F. Wiesinger, A. B. Kerr, and M. W. Vogel, "Spiral imaging artifact reduction: A comparison of two k-trajectory measurement methods," *Journal of Magnetic Resonance Imaging*, vol. 29, pp. 1485–1492, 2009.

29. G. H. Glover and N. J. Pele, "Method for magnetic field gradient eddy current compensation," U.S. Patent 4,698,591, Oct. 1987.
30. R. Prigl, U. Haeberlen, K. Jungmann, G. zu Putlitz, and P. von Walter, "A high precision magnetomer based on pulsed NMR," *Nuclear Instruments Methods A*, vol. 374, pp. 118–126, 1996.
31. V. Senaj, G. Guillot, and L. Darrasse, "Inductive measurement of magnetic field gradients for magnetic resonance imaging," *Review of Scientific Instruments*, vol. 69, pp. 2400–2405, 1998.
32. C. Barmet, N. De Zanche, and K. P. Pruessmann, "Spatiotemporal magnetic field monitoring for MR," *Magnetic Resonance in Medicine*, vol. 60, pp. 187–197, 2008.
33. K. P. Pruessmann, C. Barmet, and N. De Zanche, "Magnetic field monitoring during MRI acquisition improves image reconstruction," *Proceedings of International Society for Magnetic Resonance in Medicine*, vol. 13, p. 681, 2005.
34. N. De Zanche, C. B. C, J. A. Nordmeyer-Massner, and K. P. Pruessmann, "NMR probes for measuring magnetic fields and field dynamics in MR systems," *Magnetic Resonance in Medicine*, vol. 60(1), pp. 176–186, 2008.
35. P. Sipilä, D. Lange, S. Lechner, W. Löw, P. Gross, M. Baller, G. Wachutka, and F. Wiesinger, "Robust, susceptibility-matched NMR probes for compensation of magnetic field imperfections in magnetic resonance imaging (MRI)," *Sensors and Actuators A: Physical*, vol. 145-146, pp. 139–146, 2008.
36. C. Barmet, B. J. Wilm, M. Pavan, and K. P. Pruessmann, "A third-order field camera with microsecond resolution for MR system diagnostics," *Proceedings of International Society for Magnetic Resonance in Medicine*, vol. 17, p. 780, 2009.
37. M. B. Ooi, S. Krueger, W. J. Thomas, S. V. Swaminathan, and T. R. Brown, "Prospective real-time correction for arbitrary head motion using active markers," *Magnetic Resonance in Medicine*, vol. 62(4), pp. 943–954, 2009.
38. J. I. Jackson, C. H. Meyer, D. G. Nishimura, and A. Macovski, "Selection of a convolution function for fourier inversion using gridding [computerised tomography application]," *IEEE Transactions on Medical Imaging*, vol. 10(3), pp. 473–478, 1991.
39. P. J. Beatty, D. G. Nishimura, and J. M. Pauly, "Rapid gridding reconstruction with a minimal oversampling ratio," *IEEE Transactions on Medical Imaging*, vol. 24(6), pp. 799 – 808, 2005.
40. J. C. Hoch and A. S. Stern, *NMR Data Processing*. John Wiley & Sons, Inc., Hoboken, NJ, 1996.
41. J. Jin, *Electromagnetic Analysis and Design*. CRC Press, Boca Raton, 1999.
42. Z.-P. Liang and P. C. Lauterbur, *Principles of Magnetic Resonance Imaging: A signal Processing perspective*. IEEE Press Series in Biomedical Engineering, Piscataway, NJ, 2000.
43. R. A. de Graaf, *In Vivo NMR Spectroscopy- Principles and Techniques*. John Wiley & Sons, Ltd., 2007.
44. E. Hayes, W. A. Edelstein, J. F. Schenck, O. M. Mueller, and M. Eash, "An efficient, highly homogenous radiofrequency coil for whole-body NMR imaging at 1.5 T," *Journal of Magnetic Resonance*, vol. 63, pp. 622–628, 1985.

45. J. Tropp, "The theory of the birdcage resonator," *Journal of Magnetic Resonance*, vol. 82, pp. 51–62, 1989.
46. A. Haase, F. Odo, M. von Kienlin, J. Warnking, F. Fidler, A. Weisser, M. Nittka, E. Rommel, T. Lanz, B. Kalusche, and M. Griswold, "NMR probeheads for in-vivo applications," *Concepts in Magnetic Resonance*, vol. 12, pp. 361–388, 2000.
47. A. Abragram, *The Principles of Nuclear Magnetism*. Oxford University Press, 1978.
48. P. B. Roemer, W. A. Edelstein, C. E. Hayes, S. P. Souza, and O. M. Mueller, "The NMR phased array," *Magnetic Resonance in Medicine*, vol. 16(2), pp. 192–225, 1990.
49. T. Vaughan, L. DelaBarre, C. Snyder, J. Tian, C. Akgun, D. Shrivastava, W. Liu, C. Olson, G. Adriany, J. Strupp, P. Andersen, A. Gopinath, P.-F. van de Moortele, M. Garwood, and K. Ugurbil, "9.4T human MRI: Preliminary results," *Magnetic Resonance in Medicine*, vol. 56(6), pp. 1274–1282, 2006.
50. International Commission on Non-Ionizing Radiation Protection ICNIRP, "Guidelines for limiting exposure to time-varying electric, magnetic, and electromagnetic fields," *Health Physics*, vol. 74(4), pp. 494–522, 1998.
51. U.S. Department Of Health and Human Services, Food and Drug Administration , "Criteria for significant risk investigations of magnetic resonance diagnostic devices," 2003.
52. L. A. Shepp and B. F. Logan, "Reconstructing interior head tissue from X-ray transmissions," *IEEE Transactions on Nuclear Science*, vol. NS-21, pp. 228–236, 1974.
53. J. F. Schenck, "The role of magnetic susceptibility in magnetic resonance imaging: MRI magnetic compatibility of the first and second kinds," *Medical Physics*, vol. 23(6), pp. 815–850, 1996.
54. D. R. Lide, Ed., *Handbook of Chemistry and Physics*, 87th ed. CRC Press, Boca Raton, 2006.
55. F. D. Doty, G. Entzminger, and Y. A. Yang, "Magnetism in high-resolution NMR probe design. i: General methods," *Concepts in Magnetic Resonance*, vol. 10(3), pp. 133–156, 1998.
56. D. L. Olson, M. E. Lacey, and J. V. Sweedler, "High-resolution microcoil ^{1}H-NMR for analysis of mass-limited, nanoliter-volume samples," *Science*, vol. 270(5244), pp. 1967–1970, 1995.
57. F. Pobell, *Matter and methods at low temperatures*. Springer, New York, 2007.
58. F. G. Shellock, "Magnetic resonance safety update 2002: Implants and devices," *Journal of Magnetic Resonance Imaging*, vol. 16, pp. 485–496, 2002.
59. J. Lenz and A. S. Edelstein, "Magnetic sensors and their applications," *IEEE Sensors Journal*, vol. 6(3), pp. 631–649, 2006.
60. W. Göbel, J. Hesse, and J. N. Zemel, *Sensors: A comprehensive Survey*. VCH Verlagsgesellschaft mbH, Weinheim, 1989.
61. R. S. Popovic, *Hall Effect Devices*. Adam Hilger, Bristol, 1991.
62. P. Ripka, *Magnetic Sensors and Magnetometers*. Artech House, Norwood, 2001.
63. H. H. Sample and L. G. Rubin, "Characterization of three commercially available hall effect sensors for low temperatures and magnetic fields to 23 T," *IEEE Transactions on Magnetics*, vol. 12(6), pp. 810–812, 1976.

64. J. Heremans, "Solid state magnetic field sensors and applications," *Journal of Physics D: Applied Physics*, vol. 26, pp. 1149–1168, 1993.
65. A. S. Sedra and K. C. Smith, *Microelectronic Circuits*. Oxford University Press, New York, 1998.
66. C. Panait and G. Caruntu, "The noise of MOS magnetic microsensors structures," *International Semiconductor Conference, CAS*, vol. 1, pp. 209–212, 2008.
67. R. S. Popovic, Z. Randjelovic, and D. Manic, "Integrated hall-effect magnetic sensors," *Sensors and Actuators A*, vol. 91(1-2), pp. 46–50, 2001.
68. S. M. Sze, *Semiconductor Sensors*. John Wiley & Sons, New York, 1994.
69. J. Lenz, "A review of magnetic sensors," *Proceedings of the IEEE*, vol. 78(6), pp. 973–989, 1990.
70. R. S. Popovic, P. M. Drljaca, and C. Schott, "Bridging the gap between AMR, GMR, and hall magnetic sensors," *International Conference on Microelectronics*, vol. 23(1), pp. 55–58, 2002.
71. R. Pallas-Areny and J. G. Webster, *Sensors and Signal Conditioning*. John Wiley, New York, 1991.
72. E. Sifuentes, O. Casas, and R. Pallas-Areny, "Direct interface for magnetoresistive sensors," *IEEE Instrumentation and Measurement Technology Conference Proceedings*, pp. 1–6, 2007.
73. C. M. Wolfe and G. E. Stillman, "Anomalously high mobility in semiconductors," *Applied Physics Letter*, vol. 18(5), pp. 205–208, 1971.
74. S. A. Solin, T. Thio, D. R. Hines, and J. J. Heremans, "Enhanced room-temperature geometric magnetoresistance in inhomogeneous narrow-gap semiconductors," *Science*, vol. 289, pp. 1530–1532, 2000.
75. S. A. Solin, "Magnetic field nanosensors," *Scientific American*, vol. 291, pp. 70–77, 2004.
76. M. J. Caruso, T. Bratland, C. H. Smith, and R. Schneider, "A new perspective on magnetic field sensing," *Sensors -Peterborough-*, vol. 15(12), pp. 34–47, 1998.
77. N. A. Stutzke, S. E. Russek, and D. P. Pappas, "Low-frequency noise measurements on commercial magnetoresistive magnetic field sensors," *Journal of Applied Physics*, vol. 97, p. 10Q107, 2005.
78. C. Dolabdjian, A. Qasimi, and C. Cordier, "Applied magnetic sensing: a long way," *Proceedings of IEEE, Sensors*, vol. 1, pp. 477–482, 2003.
79. M. N. Baibich, J. M. Broto, A. Fert, F. Nguyen Van Dau, F. Petroff, P. Etienne, G. Creuzet, A. Friederich, and J. Chazelas, "Giant magnetoresistance of (001)Fe/(001)Cr magnetic superlattices," *Physical Review Letters*, vol. 61(21), pp. 2472–2475, 1988.
80. M. Pannetier-Lecoeur, C. Fermon, N. Biziere, J. Scola, and A. L. Walliang, "RF response of superconducting- GMR mixed sensors, application to NQR," *IEEE Transcions on Applied Superconductivity*, vol. 17(2), pp. 598–601, 2007.
81. J. S. Modeera, L. R. Kinder, T. M. Wong, and R. Meservey, "Large magnetoresistance at room temperature in ferromagnetic thin film tunnel junctions," *Physical Review Letters*, vol. 74(16), pp. 3273–3276, 1995.
82. K. B. Klaassen, J. C. L. von Peppen, and X. Xing, "Noise in magnetic tunnel junction devices," *Journal of Applied Physics*, vol. 93, pp. 8573–8575, 2003.

83. A. P. Ramirez, "Colossal magnetoresistance," *Journal of Physics: Condensed Matter*, vol. 9, pp. 8171–8199, 1997.
84. G. Tatara, Y. W. Zhao, M. Munoz, and N. Garcia, "Domain wall scattering explains 300 % ballistic magnetoconductance of nanocontacts," *Physical Review Letters*, vol. 83, pp. 2030–2033, 1999.
85. H. D. Chopra and S. Z. Hua, "Ballistic magnetoresistance over 3000% in Ni nanocontacts at room temperature," *Physical Review B: Condensed Matter*, vol. 66, pp. 020 403/1–020 403/3, 2002.
86. M. Hauser, L. Kraus, and PRipka, "Giant magnetoimpedance sensors," *IEEE Instrumentation & Measurement Magazine*, vol. 4(2), pp. 28–32, 2001.
87. M. R. Britel, D. Ménard, L. G. Melo, P. Ciureanu, A. Yelon, R. W. Cochrane, M. Rouabhi, and B. Cornut, "Magnetoimpedance measurements of ferromagnetic resonance and antiresonance," *Applied Physics Letters*, vol. 77, pp. 2737–2739, 2000.
88. R. Valenzuela and I. Betancourt, "Giant magnetoimpedance, skin depth, and domain wall dynamics," *IEEE Transactions on Magnetics*, vol. 38(5), pp. 3081–3083, 2002.
89. B. Culshaw, "Fiber optics in sensing and measurement," *IEEE Journal of Selected Topics in Quantum Electronics*, vol. 6(6), pp. 1014–1020, 2000.
90. M. Freiser, "A survey of magnetooptic effects," *IEEE Transactions on Magnetics*, vol. 4(2), pp. 152– 161, 1968.
91. S. Donati, V. Annovazzi-Lodi, and T. Tambosso, "Magneto-optical fibre sensors for electrical industry: analysis ofperformances," *IEE Proceedings Journal of Optoelectronics*, vol. 135(5), pp. 372–382, 1988.
92. B. Lee, "Review of the present status of optical fiber sensors," *Optical Fiber Technology*, vol. 9, pp. 57–79, 2003.
93. B. Eyre and K. S. J. Pister, "Micromechanical resonant magnetic sensor in standard CMOS," *International Conference on Solid State Sensors and Actuators. TRANSDUCERS '97 Chicago.*, vol. 1, pp. 405–408, 1997.
94. D. DiLella, L. J. Whitman, R. J. Colton, T. W. Kenny, W. J. Kaiser, E. C. Vote, J. A. Podosek, and L. M. Miller, "A micromachined magnetic-field sensor based on an electron tunneling displacement transducer," *Sensors and Actuators A*, vol. 86, pp. 8–20, 2000.
95. H. Emmerich and M. Schofthaler, "Magnetic field measurements with a novel surface micromachined magnetic field sensor," *IEEE Transactions on Electron Devices*, vol. 47(5), pp. 972–977, 2000.
96. A. S. Edelstein and G. A. Fischer, "Minimizing 1/f noise in magnetic sensors using a microelectromechanical system flux concentrator," *Journal of Applied Physics*, vol. 91, pp. 7795–7797, 2002.
97. E. W. Lee, "The approach to saturation magnetostriction of nickel," *Proceedings of the Physical Society*, vol. 65, pp. 162–163, 1952.
98. R. Osiander, S. A. Ecelberger, R. B. Givens, and D. K. Wickenden, "A microelectromechanical-based magnetostrictive magnetometer," *Applied Physics Letters*, vol. 69, pp. 2930–2931, 1996.

99. S. Dong, J. Cheng, J. F. Li, and D. Viehland, "Enhanced magnetoelectric effects in laminate composites of Terfenol-D/Pb(Zr,Ti)O_3 under resonant drive," *Applied Physics Letters*, vol. 83(23), pp. 2265–2267, 2003.
100. A. Dandridge, A. B. Tveten, G. H. Sigel, E. J. West, and T. G. Giallorenzi, "Optical fibre magnetic field sensors," *Electronics Letters*, vol. 16(11), pp. 408–409, 1980.
101. T. Giallorenzi, A. Bucaro, A. Dandridge, G. H. Siegl, J. Cole, S. Rashleigh, and R. Priest, "Optical fiber sensor technology," *IEEE Transactions on Microwave Theory and Techniques*, vol. 30(4), pp. 472–510, 1982.
102. C. M. Davis, C. J. Zarobila, and J. D. Rand, "Interferometric fiber-optic magnetometers," *Proceedings of the Annual International Conference of the IEEE Engineering in Medicine and Biology Society*, vol. 2, pp. 916–917, 1988.
103. P. Müller and A. V. Ustinov, *The Physics of Superconduction*. Springer, Berlin, 1997.
104. M. Pannetier, C. Fermon, G. Le Goff, J. Simola, and E. Kerr, "Femtotesla magnetic field measurement with magnetoresistive sensors," *Science*, vol. 304(5677), pp. 1648 – 1650, 2004.
105. M. Pannetier, C. Fermon, G. Legoff, J. Simola, E. Kerr, M. Welling, and R. J. Wijngaarden, "Ultra-sensitive field sensors - an alternative to SQUIDs," *IEEE Transactions on Applied Superconductivity*, vol. 15(2), pp. 892– 895, 2005.
106. T. Ryhänen, H. Seppä, R. Ilmoniemi, and J. Knuutila, "SQUID magnetometers for low-frequency applications," *Journal of Low Temperature Physics*, vol. 76(5-6), pp. 287–386, 1989.
107. R. Kleiner, D. Koelle, F. Ludwig, and J. Clarke, "Superconducting quantum interference devices: State of the art and applications," *Proceedings of the IEEE*, vol. 92(10), pp. 1534–1548, 2004.
108. F. Hartmann, "Resonance magnetometers," *IEEE Transactions on Magnetics*, vol. 8(1), pp. 66–75, 1972.
109. D. Duret, M. Beranger, and M. Moussavi, "An absolute earth field ESR vectorial magnetometer," *IEEE Transactions on Magnetics*, vol. 28(5), pp. 2187–2189, 1992.
110. N. Kernevez, D. Duret, M. Moussavi, and J.-M. Leger, "Weak field NMR and ESR spectrometers and magnetometers," *IEEE Transactions on Magnetics*, vol. 28(5), pp. 3054 – 3059, 1992.
111. H. R. Gray, R. M. Whitley, and C. R. Stroud, "Coherent trapping of atomic populations," *Optics Letters*, vol. 3(6), pp. 218–220, 1978.
112. P. D. Schwindt, S. Knappe, V. Shah, L. Hollberg, and J. Kitching, "Chip-scale atomic magnetometer," *Applied Physics Letters*, vol. 85(26), pp. 6409–6411, 2004.
113. P. D. Schwindt, B. Lindseth, S. Knappe, and V. Shah, "Chip-scale atomic magnetometer with improved sensitivity by use of the mx technique," *Applied Physics Letters*, vol. 90, pp. 081 102–1–3, 2007.
114. J. Kitching, S. Knappe, V. Shah, P. Schwindt, C. Griffith, R. Jimenez, J. Preusser, L.-A. Liew, and J. Moreland, "Microfabricated atomic magnetometers and applications," *IEEE International Frequency Control Symposium*, pp. 789–794, 2008.
115. I. K. Kominis, T. W. Kornack, J. C. Allred, and M. V. Romalis, "A subfemtotesla multichannel atomic magnetometer," *Nature*, vol. 422, pp. 596 – 599, 2003.

116. C. L. Dumoulin, S. P. Souza, and R. D. Darrow, "Real-time position monitoring of invasive devices using magnetic resonance," *Magnetic Resonance in Medicine*, vol. 29(3), pp. 411–415, 1993.
117. C. J. Hardy, R. O. Giaquinto, J. E. Piel, K. W. Rohling, L. Marinelli, D. J. Blezek, E. W. Fiveland, R. D. Darrow, and T. K. F. Foo, "128-channel body MRI with a flexible high-density receiver-coil array," *Journal of Magnetic Resonance*, vol. 28(5), pp. 1219–1225, 2008.
118. N. De Zanche, C. Barmet, J. A. Massner, and K. P. Pruessmann, "Advances in NMR probe technology for magnetic field monitoring," *Proceedings of International Society for Magnetic Resonance in Medicine*, vol. 14, p. 781, 2006.
119. P. Sipilä, R. F. Schulte, G. Wachutka, and F. Wiesinger, "Digital multi-band receiver for magnetic resonance," *Concepts in Magnetic Resonance Part B: Magnetic Resonance Engineering*, vol. 35B(4), pp. 210–220, 2009.
120. K. R. Minard and R. A. Wind, "Solenoidal microcoil design - part i: Optimizing rf homogeneity and coil dimensions," *Concepts in Magnetic Resonance*, vol. 13, pp. 128–142, 2001.
121. T. L. Peck, R. L. Magin, and P. C. Lauterbur, "Design and analysis of microcoils for NMR microscopy," *Journal of Magnetic Resonance, Series B*, vol. 108, pp. 114–124, 1995.
122. T. K. Ishii, *Handbook of Microwave Technology: Components and devices*. Elsevier Academic Press, Burlington, MA, 1995.
123. D. M. Pozar, *Microwave Engineering*. John Wiley & Sons, Inc., 2005.
124. *The PIN Diode Circuit Designer's Handbook*. Microsemi Corp., Watertown, Massachusetts, 1998.
125. K. Iniewski, Ed., *Medical Imaging: Principles, Detectors, and Electronics*. John Wiley & Sons, Inc., Hoboken, New Jersey, 2009.
126. D. I. Hoult and R. E. Richards, "The signal-to-noise ratio of the nuclear magnetic resonance experiment," *Journal of Magnetic Resonance*, vol. 24, pp. 71–85, 1976.
127. A. G. Webb and S. C. Grant, "Signal-to-noise and magnetic susceptibility tradeoffs in solenoidal microcoils for NMR," *Journal of Magnetic Resonance B*, vol. 113, pp. 83–87, 1996.
128. K. R. Minard and R. A. Wind, "Solenoidal microcoil design - part II: Optimizing winding parameters form maximum signal-to-noise performance," *Concepts in Magnetic Resonance*, vol. Vol. 13(3), pp. 190–210, 2001.
129. A. Kameari, "Transient eddy current analysis on thin conductors with arbitrary connections and shapes," *Journal of Computational Physics*, vol. 42, pp. 124–140, 1981.
130. I. Lindell and A. Sihvola, *Sähkömagneettinen Kenttäteoria: 2. Dynaamiset Kentät*. Otatieto, Helsinki, 2001.
131. C. Barmet, N. De Zanche, B. Wilm, and K. P. Pruessmann, "Towards routine field monitoring for MRI: a transmit/receive system based on shielded NMR probes," *Proceedings of Internatinal Society for Magnetic Resonance in Medicine*, vol. 16, p. 1152, 2008.

132. J. Bodurka, P. J. Ledden, P. van Gelderen, R. Chu, J. A. de Zwart, D. Morris, and J. H. Duyn, "Scalable multichannel MRI data acquisition system," *Magnetic Resonance in Medicine*, vol. 51, pp. 165–171, 2004.
133. M. Schmitt, A. Potthast, D. E. Sosnovik, J. R. Polimeni, G. C. Wiggins, C. Triantafyllou, and L. L. Wald, "A 128-channel receive-only cardiac coil for highly accelerated cardiac MRI at 3 tesla," *Magnetic Resonance in Medicine*, vol. 59(6), pp. 1431–1439, 2008.
134. B. Razavi, "Design considerations for direct-conversion receivers," *IEEE Transactions on Circuits and Systems II: Analog and Digital Signal Processing*, vol. 44(6), pp. 428–435, 1997.
135. ——, "Architectures and circuits for RF CMOS receivers," *Proceedings of the IEEE Custom Integrated Circuits Conference*, vol. 1998, pp. 393–400, 1998.
136. A. W. Crooke and J. W. Craig, "Digitial filters for sample rate reduction," *IEEE Transactions on Acoustics, Speech, and signal processing*, vol. 20, pp. 308–315, 1972.
137. J. H. McClellan, T. Parks, and L. Rabiner, "A computer program for designing optimum FIR linear phase digital filters," *IEEE Transactions on Audio and Electroacoustics*, vol. 21(6), pp. 506– 526, 1973.
138. L. Thede, *Practical Analog and Digital Filter Design*. Artech House, Inc., Norwood, MA, 2005.
139. R. E. Crochiere and L. R. Rabiner, "Optimum FIR digital filter implementation for decimation, interpolation, and and narrow-band filtering," *IEEE Transactions on Acoustics, Speech, and signal processing*, vol. 23, pp. 444–456, 1975.
140. T. Saramäki, "A class of linear-phase FIR filters for decimation, interpolation, and narrow-band filtering," *IEEE Transactions on Acoustics, Speech, and signal processing*, vol. 32(5), pp. 1023–1036, 1984.
141. P. E. Allen and D. R. Holberg, *CMOS Analog Circuit Design*. Oxford University Press, 2002.
142. A. Demir, A. Mehrotra, and J. Roychowdhury, "Phase noise in oscillators: A unifying theory and numerical methods for characterization," *IEEE Transactions on Circuits and Systems I: Fundamental Theory and Applications*, vol. 47(5), pp. 655–674, 2000.
143. W. He, X. Qin, R. Jiejing, and L. Gengying, "Four-channel magnetic resonance imaging receiver using frequency domain multiplexing," *Review of Scientific Instruments*, vol. 78, p. 015102, 2007.
144. I. Lindell and A. Sihvola, *Sähkömagneettinen Kenttäteoria: 1. Staattiset Kentät*. Otatieto, Helsinki, 2001.
145. P. Sipilä, D. Lange, S. Lechner, W. Löw, P. Gross, M. Baller, G. Wachutka, and F. Wiesinger, "Simple and robust design for susceptibility-matched NMR magnetic field monitoring probes," *Proceedings of International Society for Magnetic Resonance in Medicine*, vol. 15, p. 629, 2007.
146. C. Windischberger, S. Robinson, A. Rauscher, M. Barth, and E. Moser, "Robust field map generation using a triple-echo acquisition," *Journal of Magnetic Resonance Imaging*, vol. 20, pp. 730–734, 2004.

147. National Institute of Standard and Technology, www.nist.gov.
148. P. Sipilä, S. Greding, G. Wachutka, and F. Wiesinger, "^{2}H transmit-receive nmr probes for magnetic field monitoring in MRI," *Magnetic Resonance in Medicine*, vol. (submitted), p. NA, 2009.
149. *Handbook of High Resolution Multinuclear NMR*. John Wiley & Sons, Inc., New York, NY, 1981.
150. F. Wiesinger, P. Sipilae, S. M. Lechner, and R. F. Schulte, "Magnetic field monitored autofocus deblurring for improved non-cartesian imaging," *Proceedings of International Society for Magnetic Resonance in Medicine*, vol. 16, p. 790, 2008.
151. J. T. Schneider, C. Barmet, W. Ruhm, K. P. Pruessmann, and P. Ullmann, "Using dedicated field probes for trajectory measurements in parallel excitation experiments," *Proceedings of International Society for Magnetic Resonance in Medicine*, vol. 18, p. 4926, 2010.

11

List of Symbols and Physical Constants

a	sphere diameter
A	area, gain
B	magnetic flux density
ΔB	uncertainty in magnetic flux density
χ	volumetric susceptibility
C	capacitance
δ_s	skin depth
σ	conductivity
d	diameter
ε	electrical permittivity
ΔE	energy difference between two spin states
$\mathbf{E}$	electric field strength
f	frequency
F	input signal
f_l	spatial basis function
γ	gyromagnetic ratio
$\mathbf{G}$	gradient of magnetic flux density
h	Planck's constant
I	electrical current
$\mathbf{j}$	current density
J	spin quantum number
J_s	solenoid coil geometry-dependent variable
$\mathbf{k}$	k-space location
$\Delta\mathbf{k}$	uncertainty in k-space location
k_B	Boltzmann's constant
K_s	solenoid coil geometry-dependent variable

λ	wavelength
l	length
L	inductance
m	magnetic quantum number
μ	magnetic moment
μ_0	volumetric permeability
M	number of FIR filter coefficients
$\mathbf{M}$	bulk magnetization
N	number of turns in solenoid coils, number of data points
N_α, N_β	spin state density
N_l	number of spatial basis functions
n	spin density per unit volume
ω	angular frequency
ϕ_m	magnetic potential
φ	phase
$\Delta\varphi$	uncertainty in phase
Ψ_-	coil receive sensitivity
p_m	relative magnetic dipole momentum
P	power
Q	quality factor
R	electrical resistance
$\mathbf{r}$	spatial location
Δr	NMR sample dimension
S	signal amplitude
τ_0	delay
θ	angle
t_h	thickness
t	time
Δt	uncertainty in time
T	temperature
T1	spin-lattice relaxation time constant
T2	spin-spin relaxation time constant
T2*	relaxation time constant for transverse magnetization

$T_{inhomog.}$	magnetic field inhomogeneity induced relaxation time constant for transverse magnetization
u, U	voltage, induced electromotive force
Δu	uncertainty in voltage
V	volume
Δx	image resolution
X	electrical reactance
Y	closed-loop gain
Y_{real}	electrical conductance
ζ	enhancement factor
Z	electrical impedance

12

List of Acronyms

ADC	analog-to-digital converter
AMR	anisotropic magnetoresistance
a.u.	arbitrary units
BMR	ballistic magnetoresistance
BPF	band-pass filter
BW	bandwidth
CMR	colossal magnetoresistance
DC	direct current
DSP	digital signal processing
EMR	extraordinary magnetoresistance
EPI	echo planar imaging
EPR	electron paramagnetic resonance
FFT	fast Fourier transform
FID	free induction decay
FIR	finite impulse response
FOV	field of view
GMI	giant magnetoimpedance
GMR	giant magnetoresistance
IQ	in-phase + quadrature
LNA	low noise amplifier
LPF	low-pass filter
LSB	least significant bit
MAGFET	metal-oxide-semiconductor field-effect magnetotransistor
MEMS	microelectromechanical system
MR	magnetic resonance
MRI	magnetic resonance imaging
MTJ	magnetic tunnel junction
NEX	number of excitations

NF	noise figure
NMR	nuclear magnetic resonance
PA	power amplifier
ppb	parts per billion
ppm	parts per million
RF	radio frequency
SAR	specific absorption rate
SNR	signal-to-noise ratio
SERF	spin-exchange relaxation free
SQUID	superconducting quantum interference device
TE	echo time
TR	repetition time

Acknowledgments

Alone, I would have never finished this thesis. The deepest and the most sincerest gratitude goes to my family and to my closest friends, whose help and support I value the most. You gave me the strength, and you have always been with me in my thoughts.

I want to thank Prof. Gerhard Wachutka for the supervision of my thesis and all his support during the past four years. I am deeply grateful to Dr. Florian Wiesinger for his tremendous help and guidance throughout this thesis. Credit should be given to him especially for his indispensable work on analyzing data, pulse programming, as well as on simulation- and reconstruction-related issues. Dr. Dirk Lange should be acknowledged for the implementation of the pick-up-coil-based gradiometers and performing the corresponding magnetic field monitoring experiments. The sincerest gratitude of mine, however, goes to him for his invaluable guidance as well for his precious help throughout my thesis. Dr. Silke Lechner has given her priceless efforts conducting magnetic field monitoring experiments, implementing MRI pulse sequences and reconstruction algorithms, and helping with magnetostatic simulations. I also want to thank Dr. Marko Baller for sharing his expertise in chemistry. In addition, Sebastian Greding should by all means get the credit for his efforts in manufacturing NMR probes.

I also want to thank Dr. Bill Antel, Dr. William Grissom, M.Sc. Guido Kudielka, Dr. Mark Lynass, Dr. Laura Sacolick, M.Sc. Sundeep Patil, Dr. Victor Samper, and M.A. Dorothea Teubner for helping to proofread my thesis. I want to express my sincerest gratitude to the mentioned individuals as well as to dear colleagues Dr. Dong Chen, Dr. Tom Foo, Dr. Patrick Gross, M.Sc. Wolfgang Löw, Dr. Rolf Schulte, M.Sc. Jonathan Sperl, and Dr. Jim Tropp for all the fruitful discussions and momentous input on various topics of my thesis. I also want to thank the Finnish Foundation for Economic and Technology Sciences, the International Society of Magnetic Resonance in Medicine, a Karl Max Von Bauernfeind Grant, and Technical University of Munich for financial support.

Thank you, Kiitoksia.